UNIVERSIDAD DE CHILE
FACULTAD DE CIENCIAS FÍSICAS Y MATEMÁTICAS
DEPARTAMENTO DE INGENIERÍA MECÁNICA

ANALYTIC AND PARAMETRIC STUDY OF HIGH-TEMPERATURE PACKED-BED TES SYSTEMS USING COPPER SLAGS AS FILLER MATERIAL

TESIS PARA OPTAR AL GRADO DE
MAGÍSTER EN CIENCIAS DE LA INGENIERÍA, MENCIÓN MECÁNICA

MEMORIA PARA OPTAR AL TÍTULO DE INGENIERO CIVIL MECÁNICO

IGNACIO ANDRÉS CALDERÓN VÁSQUEZ

PROFESOR GUÍA:
JOSÉ CARDEMIL IGLESIAS

MIEMBROS DE LA COMISIÓN:
RUBÉN FERNÁNDEZ URRUTIA
ALVARO VALENCIA MUSALEM
RODRIGO BARRAZA VICENCIO
RAFAEL GUÉDEZ MATA

Este trabajo ha sido parcialmente financiado por FONDECYT

SANTIAGO DE CHILE
2021

RESUMEN DE LA MEMORIA PARA OPTAR
AL TÍTULO DE INGENIERO CIVIL MECÁNICO
Y GRADO DE MAGÍSTER EN CIENCIAS DE LA
INGENIERÍA, MENCIÓN MECÁNICA
POR: IGNACIO ANDRÉS CALDERÓN VÁSQUEZ
FECHA: 2021
PROF. GUÍA: JOSÉ CARDEMIL IGLESIAS

ANALYTIC AND PARAMETRIC STUDY OF HIGH-TEMPERATURE PACKED-BED TES SYSTEMS USING COPPER SLAGS AS FILLER MATERIAL

Increasing the operating temperature is the challenge of the third generation of concentrating solar power (CSP) plants, leading to the exploration of new technological alternatives. In that context, packed-bed thermal energy storage (TES) systems have emerged as a promising proposal, since low-cost storage materials can be employed to exchange heat with a working fluid such as natural rocks or industrial byproducts. The use of a solid material as a storage medium allows operation at high temperatures and improves the efficiency of solar-to-electrical energy conversion.

The present thesis aims to assess the high-temperature performance of a packed-bed TES system using Chilean copper slags as a filler material. The modelling approaches and the key design variables of these systems are studied. Based on a previous characterization of the copper slag's thermophysical properties and the development of a heat transfer model, its behavior in a packed-bed TES is assessed and contrasted with other waste materials studied in the literature. Through a parametric analysis in terms of the geometric dimensions and tank shape of the TES, the variation of its performance indicators is studied. The latter allows the proposal of design strategies of these systems, and to extend their applicability in other renewable energy technologies, such as Carnot batteries and compressed air energy storage systems (CAES).

A first and second law analysis is conducted to study the evolution of the thermocline within the tank, the round-trip efficiency, the heat losses, the exergy efficiency, and the irreversibilities during the heat transfer between the phases. Additionally, the pressure drop is analyzed. The developed model is also generalized for different TES geometries, such as cylindrical tank with axial fluid flow, truncated cone shape with axial flow, and a novel proposal consisting in arrange the filler material between two concentric cylinders and performing the fluid injection in the radial direction.

Results show that the copper slags' high specific heat of 1.4 - 1.5 J/(g K) enables a lower thermal front velocity through the packed-bed, which allows the discharge of higher temperatures for longer periods than the other materials studied. In addition, TES systems with high energy density can be obtained for more compact geometric dimensions. On the other hand, by varying the TES shape, the radial-flow proposal decreases the thermal losses by 80 % compared to conventional topologies, and lower pressure drop requirements. Therefore, the use of copper slags in radial-flow packed-bed systems is a potential candidate to reduce the costs in high-temperature TES.

RESUMEN DE LA MEMORIA PARA OPTAR
AL TÍTULO DE INGENIERO CIVIL MECÁNICO
Y GRADO DE MAGÍSTER EN CIENCIAS DE LA
INGENIERÍA, MENCIÓN MECÁNICA
POR: IGNACIO ANDRÉS CALDERÓN VÁSQUEZ
FECHA: 2021
PROF. GUÍA: JOSÉ CARDEMIL IGLESIAS

ESTUDIO ANALÍTICO Y PARAMÉTRICO DE UN SISTEMA DE ALMACENAMIENTO TÉRMICO DE LECHO DE ROCAS A ALTAS TEMPERATURAS USANDO ESCORIA DE COBRE COMO MATERIAL DE RELLENO

El desafío de la tercera generación de plantas de concentración solar de potencia (CSP) es aumentar la temperatura de funcionamiento. En búsqueda de alternativas tecnológicas para lograrlo, los sistemas de almacenamiento térmico (TES) de lecho de rocas se han planteado como propuesta prometedora, pues emplean rocas naturales o subproductos industriales de bajo costo, para almacenar energía mediante el intercambio térmico con un fluido de trabajo. El uso de un material sólido como medio de almacenamiento admite la operación a altas temperaturas y mejorar la eficiencia de conversión de energía solar a eléctrica.

La presente tesis busca evaluar el desempeño a altas temperaturas de un sistema TES de lecho de rocas usando escoria de cobre chilena como material de relleno. Para ello, se estudian las estrategias de modelación de estos sistemas y sus variables clave de diseño. Con una previa caracterización de las propiedades termofísicas de la escoria de cobre y el desarrollo de un modelo de transferencia de calor, se evalúa su comportamiento en un TES de lecho de rocas y se contrasta con otros materiales de desecho estudiados en la literatura. A través de un análisis paramétrico de las dimensiones geométricas y la forma del estanque, se estudia cómo varía su desempeño, para proponer estrategias de diseño de estos sistemas y extender su aplicación en otras tecnologías de energías renovables, como baterías de Carnot o sistemas de almacenamiento de aire comprimido (CAES).

Con un análisis de primera y segunda ley de la termodinámica, se estudia la evolución de la termoclina del TES, eficiencia de round-trip, pérdidas de calor, eficiencia exergética, caída de presión e irreversibilidades durante el intercambio de calor entre las fases. El modelo desarrollado es generalizado para distintas geometrías de almacenamiento térmico, como estanques cilíndricos con flujo axial de fluido, estanques de cono truncado con flujo axial, y una nueva propuesta geométrica que consiste en disponer el material de relleno entre dos cilindros concéntricos y realizar inyección de fluido en la dirección radial.

Los resultados muestran que el alto calor específico de 1.4 - 1.5 J/(g K) de la escoria de cobre permite un avance más lento de la termoclina a través del lecho de rocas, descargando mayores temperaturas por períodos más prolongados que en otros materiales estudiados. Además, es posible obtener sistemas de almacenamiento con alta densidad energética para geometrías más compactas. Por otro lado, al variar la forma del almacenamiento, el nuevo sistema de flujo radial disminuye en un 80 % las pérdidas térmicas frente a topologías convencionales, y con bajos niveles de pérdida de carga. Por lo tanto, el uso de escoria de cobre en sistemas de lecho de rocas con flujo radial de fluido es un candidato potencial para reducir los costos en los sistemas TES para altas temperaturas.

Dije que me equivocaría
y como me equivoqué,
tuve razón.

Roberto Musso

Acknowledgments

Quisiera comenzar con unas disculpas públicas a mi tata y abuela, pues les prometí hace 9 años que estudiaría arquitectura y les diseñaría una casa... Y bueno, acá estamos. Aprovechar también de agradecerles por el inmenso cariño y apoyo que me han dado, esas idas a buscar al colegio y los innumerables gansitos que me dieron siempre que me subía al auto. Gracias madre por los abrazos, las palabras de ánimo y simplemente por escucharme cuando era necesario. A mi papá por enseñarme que nada es gratis en la vida y por apoyarme en mis decisiones. A ambos les agradezco el esfuerzo por darme la educación que hoy tengo y por criarme como soy ahora. Gracias a mis hermanas mayores que siempre me han cuidado y aconsejado, les agradezco desde las peleas hasta los buenos momentos.

Mencionar a esas amistades que hasta el día de hoy han estado ahí a pesar de la distancia: Pedro, Franco, Constanza, Alejandro, Pablo, Santiago y Paula, y al piño, obviamente: Alonso, Edgar, Víctor, Rodrigo, Diego, Pablo, José Manuel, Guillermo y Marcela. Gracias por los momentos, las canciones tocadas, las tocatas, los pedaleos, los asados, los viajes, las eternas conversaciones, los apañes a estudiar, las discusiones random, las monadas, y sobre todo, las cervezas compartidas. Quisiera dedicar también palabras especiales a las personas que conocí en el DIMEC que hicieron que el día a día fuera más agradable, gracias a ustedes por las conversaciones de pasillo, los almuerzos interminables, las idas al subway y los recuerdos que hasta hoy atesoro.

Agradezco también el apoyo y la formación que he tenido de los profesores con quienes he tenido clases y trabajado hasta el día de hoy. A los y las funcionarias del DIMEC con quienes siempre fue grato compartir y siempre se preocuparon de cómo estaba. Muchas gracias también al grupo de investigación que pertenezco actualmente y espero podamos seguir contribuyendo activamente al desarrollo científico del país. Gracias por el trabajo dedicado y poder lograr los objetivos a pesar de la carga emocional y académica.

Quiero dedicar unas palabras al Prof. José Miguel Cardemil, que hasta el día de hoy ha tenido siempre la disposición de ayudarme y de brindarme apoyo académico. Agradezco también las oportunidades que me ha dado para seguir desempeñando una carrera en la investigación y la formación profesional, ética y académica que constantemente me ha entregado.

Por último, una página no hace justicia para expresar la inmensa gratitud que siento hacia todas las personas que han pasado durante todos estos años de estudio. Pese a que muchas no estén mencionadas explícitamente, su presencia ha sido significativa en cada una de las palabras que he plasmado acá. Por todos los que estuvieron, los que están y los que estarán. Gracias... Totales!

Contents

List of Tables

List of Figures

Chapter 1

Introduction

Recent international agreements to address the environmental crisis aim to place renewable energies at the forefront of the energy matrix, projected to account for at least 60% of total energy consumption in many countries by 2050 [1]. Today, power generated by renewable sources has become highly competitive, so that by the end of 2018, photovoltaic (PV) and wind power plants have become more cost effective than fossil fuel-powered generators [2]. However, the great disadvantage of both wind and PV power is their intermittency in terms of generation, which is related to the variability of the resource from which they convert energy [3]. Thus, the use of Concentrating Solar Power (CSP) technologies turns competitive compared to other energy sources, since it can be coupled to a thermal storage system (TES) that extends the electricity generation capacity even at times when radiation is not available [3, 4].

Among the commercial technologies found in CSP plants, the tower with central receiver and heliostats is distinguished from the others by its high operating temperatures (around 570 °C). It consists of mirrors located on a horizontal plane, which track the sun and concentrate the direct normal irradiation (DNI) in a receiver placed at the top of a tower (see Figure 1.1). In the receiver, the conversion of the radiation into useful heat takes place through the temperature rise of a heat transfer fluid (HTF) circulating inside its geometry. The heat is delivered in a steam generator for a Rankine cycle, which is illustrated in Figure 1.1 with the process of power generation in a solar tower plant. Unlike PV technology, CSP plants have thermal inertia; hence, the hourly variability of the solar resource does not have immediate effects on electricity generation. In addition, thermal storage systems coupled to CSP allows to extend power generation during cloudy days or after daylight hours [5]. However, installed capacity of CSP is still less than 1 % of solar PV and wind power because of their high levelized costs of electricity (LCOE), which according to He et al. by 2018 had a superior nominal value of 10.3 ¢/kWh [6] compared to 8.5 and 5.6 ¢/kWh for the aforementioned technologies, respectively [3, 6].

Aiming to improve the anual performance on CSP plants and to reduce the LCOE, different alternatives have been proposed by the scientific community [7]. According to Kolb et al., one way to characterize the annual performance of a tower plant is through the solar-to-electric conversion efficiency. That parameter can be improved through the enhancement

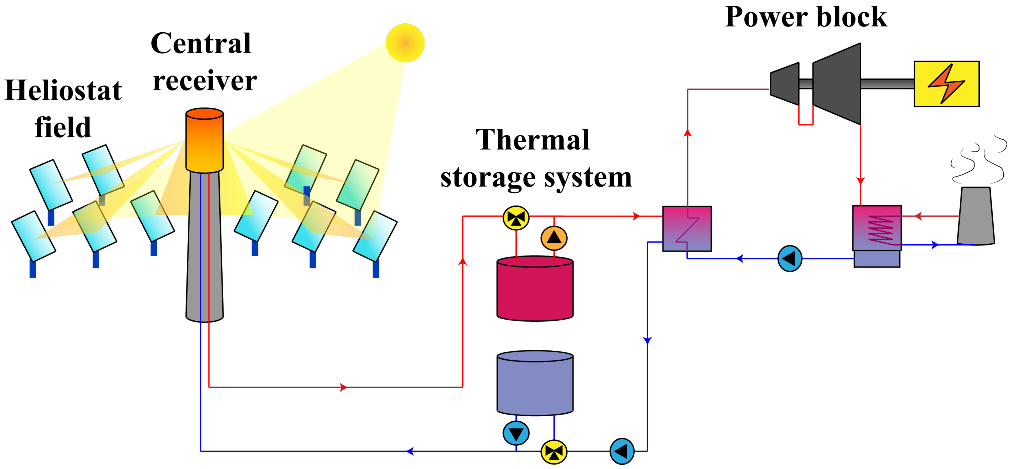

Figure 1.1: Diagram of central tower CSP plant with heliostat field

of the different subsystems which compose the CSP plant (see Figure 1.1): Heliostat field, central receiver, thermal storage system, and power block [7]. Thus, for the 3rd generation of CSP plants, the main objective is to improve the efficiency of the power cycle and, as a consequence, the conversion efficiency [3]. According to Carnot's principle, by increasing the current operating temperatures of commercial plants, that goal can be achieved, so in order to integrate new power cycles into the system, new technological alternatives are needed.

1.1 Thermal energy storage systems

Thermal storage technologies have become a promising alternative to address the mismatch between electricity demand and solar resource availability [8]. These systems are capable to store energy for a time period and then supply it to a thermal process [9]. Depending on the daily variations of supply/demand profiles, CSP plants with TES systems can have several operational strategies [8]. For instance, as shown in Figure 1.2 the energy produced during peak hours of the solar resource can be stored and delivered to the power block during peak hours of the demand, which are commonly during the hours where radiation is low.

TES systems are generally composed of three parts: the storage medium, the heat transfer mechanism, and the container system [11]. The thermal storage medium accumulate thermal energy in the form of sensible heat, latent heat or through chemical reactions. Through a heat transfer mechanism, the energy is supplied/extracted to/from the storage medium (commonly named charge/discharge process). Finally, the container system holds the storage medium and insulates the system from the environment allowing heat transfer processes to occur within it. Depending on the type of the storage medium and its interaction with the TES components, Herrmann et al. have identified several requirements that a TES system must fulfill to guarantee its proper operation [12].

1. High energy density in the storage medium.
2. Good heat transfer between the heat transfer fluid (HTF) and the storage medium.
3. Mechanical and chemical stability of the storage medium.
4. Chemical compatibility between HTF, container system and storage medium.

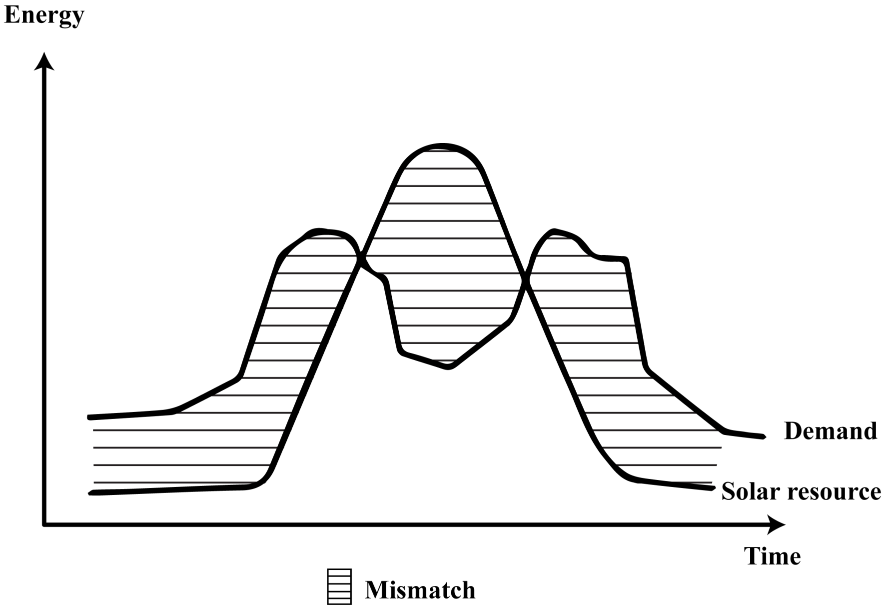

Figure 1.2: Scheme of the daily mismatch between solar resource and demand. Modified from [10]

5. Complete reversibility for a large number of charging/discharging cycles.
6. Low thermal losses.
7. Low costs.
8. Low environmental impact.

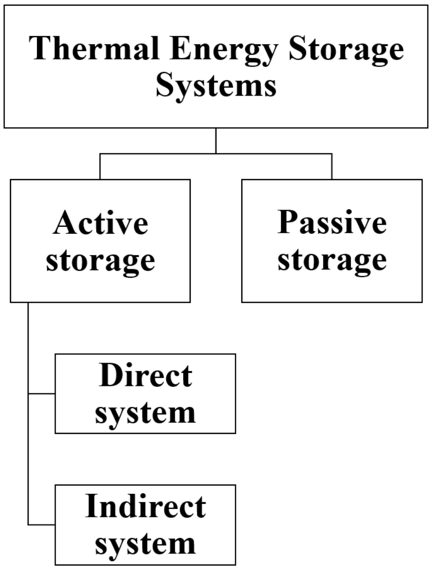

Figure 1.3: Classification of different storage concepts. Modified from [8]

Gil et al. established a general classification of the storage concept, which is illustrated in Figure 1.3. An active storage consists of using forced convection mechanisms in a fluid storage medium to extract energy through a heat exchanger or steam generator. Within this type, there are direct systems, where the storage medium is also the heat transfer fluid.

On the other hand, in the indirect systems the storage medium and the working fluid are different, so a heat exchanger is required to recover the stored energy [8, 13]. Passive storage systems are generally composed by a HTF that flows through the storage medium to store the energy transported during a charging process, and then recover it from the storage when discharging.

The current trends in thermal storage in commercial CSP plants are presented below, along with the new challenges to be solved for the 3$^{\text{rd}}$ generation.

1.1.1 Current trends in CSP plants

The following elements need to be considered on the design of TES systems for CSP plants[12]:

1. Nominal temperature and specific enthalpy delivered to the load.
2. Maximum load.
3. Operational strategy.
4. Integration into the plant.

The above enables the selection of the TES system and its design. In a commercial scale, two main technologies can be distinguished: molten salt storage and steam storage [11, 12].

Molten salt storage

Molten salts are widely used as a storage media in commercial CSP plants. Their configuration is based in a double tank system, where hot and cold salts are accumulated separately. Commercial salt known as “Solar Salt” is a mixture of 60% KNO_3 and 40% $NaNO_3$ (weight) [8], and it has a limited operating temperature: Under 290 °C the molten salt freezes and above 565 °C it loses its thermal properties and become highly corrosive; despite of the latter, its high energy density makes it a desirable medium for high-temperature applications through sensible heat energy storage.

Based on the classification proposed by [13], these are active storage systems where the HTF extract the energy from the storage medium through a heat exchanger as shown in Figure 1.1. The good thermal properties of the molten salts enable them to be used as a working fluid and storage media, which is an attractive alternative for central tower plants, as it can be heated directly in the central receiver and reach high operating temperatures.

In direct operation, once heated in the receiver, they flow through the piping loop of the plant and are either injected into the hot salt storage or sent through the steam generator to drive the power cycle. During times of low radiation, the stored hot salts are extracted and passed through the heat exchanger, allowing continuous operation of the power block. When leaving the steam generator, the salts are stored in the cold salt tank to be reintegrated into the receiver.

On the other hand, since parabolic through plants operates at temperatures around 350 °C [14], it is common for thermal oils to be used as HTF with a molten salt TES system integrated indirectly, where the thermal oil transfers heat to the molten salt tanks through a heat exchanger to deliver/recover the energy (see Figure 1.4).

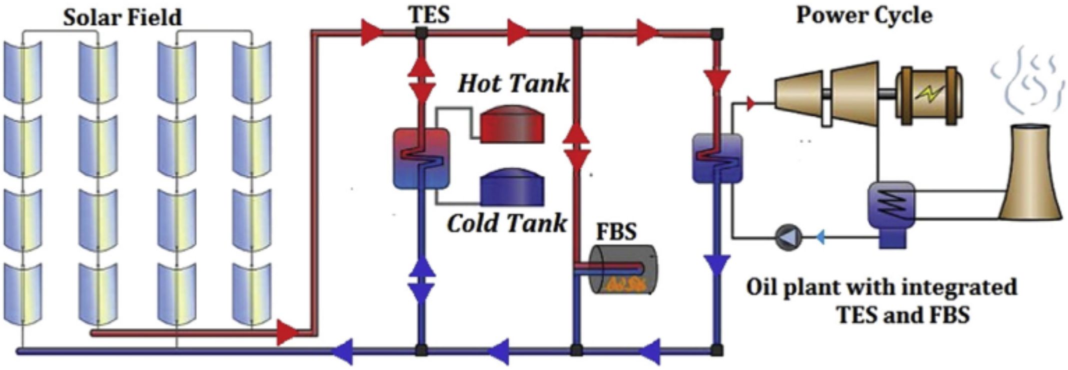

Figure 1.4: Diagram of parabolic through CSP plant with TES system [14]

Steam accumulator storage

The use of water as HTF is suitable for Direct Steam Generation plants (DSG), which is a commercial option in central tower plants since it does not require an intermediate steam generator. In DSG plants the superheated steam is generated in the central receiver; therefore, it can be injected directly into the high-pressure turbine of the cycle [8, 11]. The charging of storage takes place when the superheated steam or saturated water enters a pressurized tank. Depending on the quality of the inlet, the storage's behavior is going to be different [11]:

- If the system is charged with superheated steam, the initial saturated water and steam will increase their temperature and pressure, changing the saturation state.
- When saturated liquid is used to charge the system, pressure and temperature will remain constant, but increasing the mass in the volume.

The discharge process of the steam accumulator takes place when the pressure of the tank is reduced, and saturated steam is produced. If superheated steam is required, a secondary tank is employed to increase the temperature of the steam [8, 11].

1.1.2 New generation challenges

As mentioned above, increasing the operating temperature of the power cycle improves the conversion efficiency. However, current technology in central tower CSP plants has temperature limits which should not be exceeded to avoid global system failures [3]. In that context, interest has been placed on developing solutions to achieve the proposed operating conditions for the new CSP generation which He et al. have listed in its work [3] (Table 1.1).

In addition, targets have been set for thermal storage systems towards the year 2030 [6, 15]:

1. TES cost < 15 ¢/kWh_{th}.
2. Exergetic efficiency $> 95\,\%$.
3. Material degradation due to corrosion $< 15\,\mu\mathrm{m/year}$.

Recent research trends have suggested thermocline packed-bed storage systems [16, 17, 18]

Feature	Expected condition
Receiver outlet temp.	$> 700\,^{\circ}\mathrm{C}$
Power cycle	Brayton
Design cycle eff.	$> 50\,\%$
LCOE [6]	5 ¢/kWh

Table 1.1: Operating conditions of the 3rd generation of CSP plants [3]

as an alternative for high-temperature applications. This passive storage system consists in a rock pile (heat transfer medium) confined in a storage tank where heat is transferred with the HTF during the charge/discharge process. These systems can be coupled with solid industrial byproducts obtained from high-temperature processes, which allow them to have stable operation in applications above 650 °C [17, 19]. In addition, the combination with low-cost HTF such as air reduces the estimated costs of these systems by 35% below molten salt TES systems [17].

1.2 Scope of the thesis

The previous sections evidenced the problems presented by current thermal storage technologies and how they do not fulfill the operating conditions that are projected for the new generations of CSP plants. In addition, thermocline packed-bed systems are briefly discussed as a promising alternative, which will be treated in depth in the following chapters. Thus, within the scope of the thesis, applications of these systems at temperatures up to 650 °C are contemplated, which is compatible with thermodynamic cycles of 3rd generation of CSP plants such as Brayton cycles with compressible gases. Furthermore, the models developed can be extended to different packed-bed storage topologies, and the applicability of the models can also be integrated to any thermal process with heat storage requirements.

Based on the above, a key objective of the work can be established along with the steps to be taken to achieve it.

1.2.1 General objective

Evaluate the high temperature performance of a packed-bed thermal storage system using copper slag as a filler material.

1.2.2 Specific objectives

- Identify the modelling approaches of packed-bed systems.
- Develop an analytical heat transfer model.
- Study the performance of using copper slags as a storage media in a packed-bed TES.
- Analyze the impact of the storage dimensions over the packed-bed's performance indicators.
- Compare different packed-bed topologies for high-temperature TES applications.

1.3 Outline of the thesis

The present MS thesis assess the impact of packed-bed TES design features on its thermal performance. Using industrial byproducts as a storage medium and air as a HTF, a first and second law analysis is conducted to determine metrics and evaluate the system's performance during its operation; therefore, design guidelines are developed by studying the behavior of those metrics with the different conditions of the packed-bed structures. In that context, the studies carried out during the program have been ordered to give a logical structure to the thesis. Its organization consists in 5 chapters, where chapters 2 to 4 have been written as independent self-contained articles, with their own abstract, introduction, and respective conclusions.

This dissertation starts with a literature review regarding the modeling approaches of packed-bed TES for sensible heat applications (chapter 2). In addition, the design considerations, conventional structures, storage materials, and validation methodologies are reviewed. In the discussion of the available thermal models a gap in knowledge is recognized in terms of the radiation heat transfer treatment. As a result, a case study is developed in order to quantify the relevance of the radiation in packed-bed systems.

One of the key parameters on the design of packed-bed TES systems, is the storage medium which stores the heat. In chapter 3 a study on the performance of a cylindrical packed-bed system is conducted, considering different storage materials and storage dimensions. Furthermore, an initial characterization of the copper slags' thermophysical properties is developed, and this industrial byproduct is presented as a novel alternative for high-temperature storage applications.

Another interesting aspect assessed is the effect of the packed-bed topology used. For instance, conventional packed-bed systems are based in a cylindrical storage with axial flow of the HTF; therefore, the fluid flows through a packed-bed column with a constant cross-sectional area. Nevertheless, aiming to decrease the thermal losses and pressure drop, different flow configurations and packed-bed geometries have been proposed. In chapter 4, a comparative study is conducted in terms of the packed-bed topology, and four domains are analyzed. They are compared under the same operating conditions during a consecutive cyclic operation. Additionally, a parametric analysis is developed in terms on the design geometry of the packed-bed topologies. A detailed modelling of the heat transfer phenomena, thermal losses, pressure drop, and entropy generation is performed in order to compare their behavior.

In addition, the efforts to develop an experimental facility are described in Appendix A. Their components and the actual state of the test bench is detailed, including the experiments that will be conducted to study the real performance of an experimental scale packed-bed system using copper slags as filler material. Finally, the general conclusions of this master's thesis are presented in chapter 5 along with a proposal for future research to extend the current work and enhance the potential use of these systems.

Chapter 2

Review on modeling approaches for packed-bed thermal storage systems

Several authors have established single-tank packed-bed storage as a promising alternative that can be coupled with renewable thermal energy sources. The use of such systems can ensue a cost reduction of approximately 33%, compared to two-tank systems, which represents the dominating solution for high-temperature storage. Herein, an overview of the modeling approaches for assessing the yield and efficiency of packed-bed energy storage systems is presented. Additionally, the validation approaches used as well as the conventional materials and structures employed in such systems are described. One of the critical issues that affect the performance of simulation models in packed-bed energy storage systems is the treatment of the radiation exchange among particles. The impacts of the radiation phenomena on the overall performance and internal temperature distribution of the tank, which facilitate the identification of the operating conditions within the influence of radiation and are significant for analytical purposes are discussed herein. Through parametric analysis, it is demonstrated that the radiation heat transfer coefficient could be as high as 32% of the magnitude of the convection coefficient; thus, it should not be underestimated when analyzing operation temperatures above 750 °C.

2.1 Introduction

Sensible thermal energy Storage (STES) systems entail the increment of the internal energy of the storage material using a heat source carried by a heat transfer fluid (HTF) (Figure 2.1), which raises the temperature of the storage material. STES systems have been used in several applications ranging from 120 °C to 1250 °C. These systems have three essential components: (1) the storage medium, (2) the energy transfer mechanism, and (3) the confinement system [20]. Moreover, STES systems can be divided into three main categories: (1) those that operate using high-temperature working fluids as direct storage media, (2) systems that use a solid storage material that is heated using an intermediate fluid, and (3) processes that transfer heat from one fluid to another through a third storage material. Nonetheless, no phase change occurs within the temperature range [21, 22]. The operation of the STES systems is described in Figure 2.1, where a hot heat transfer fluid initially loads the system. Thereafter, this energy is maintained until an external demand requires its release. Subsequently, the unloaded system returns back to the initial state and is ready for a new loading cycle. From the literature, it is commonly accepted that the effectiveness of the system depends on the ratio between the length portion outside the thermocline (useful energy) and the height of the tank [23], as described in Figure 2.2.

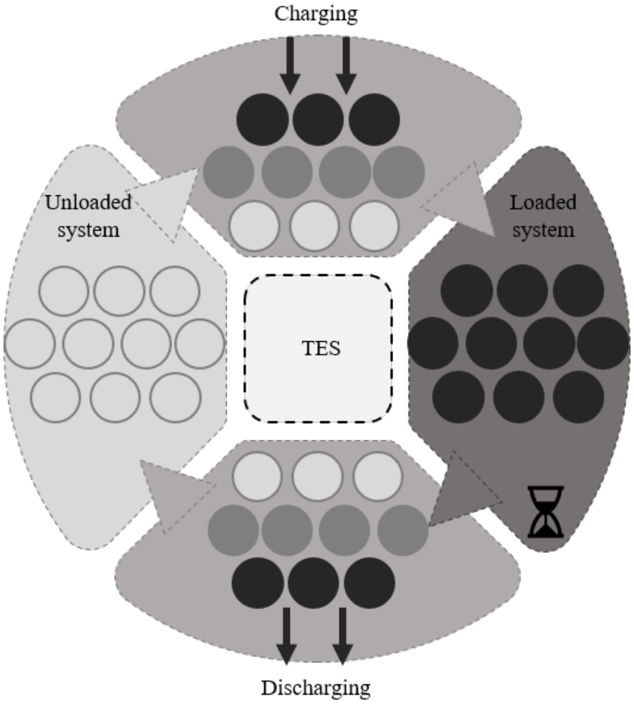

Figure 2.1: Brief description of a STES system round-trip operation.

Based on the STES technologies that have been developed or are currently under investigation, single-tank packed-bed storage has been acknowledged by several authors as an interesting option that can be coupled with renewable thermal energy sources [24]. Packed-bed thermal storage involves the use of solids as the heat storage medium and a HTF in direct contact with the solids to convey heat [25]. Contrary to the conventional two-tank system, packed-bed storage employs a single tank wherein a transition zone separates the hot and cold regions with a thermal gradient called a ”thermocline” (see Figure 2.2). Therefore, the essential operating characteristic is the buoyancy stratification principle that allows fluid separation at the top and bottom regions of the thermal energy storage (TES) tank. This feature enables the system to be discharged from the base and charged at the top in a single tank, which implies cost savings of approximately 33%, compared to two-tank systems [26, 27]. As shown in Figure 2.3, for packed-bed heat storage, all heat transfer mechanisms apply among the solid particles, the tank walls, and the fluid. During charge operation, the hot fluid enters through the top of the tank and transfers heat to the solid material, accumulating energy as sensible internal energy. During the discharge process, when the demand is higher than the power generated directly by the plant, the cold fluid goes to the bottom of the tank to obtain heat from the solid that will be used by the demand block [28]. The amount of energy that can be stored is proportional to the mass, specific heat capacity, and the temperature difference between the initial and final state, also known as the temperature swing. The low thermal capacity of STES materials is balanced by the temperature swing, thereby

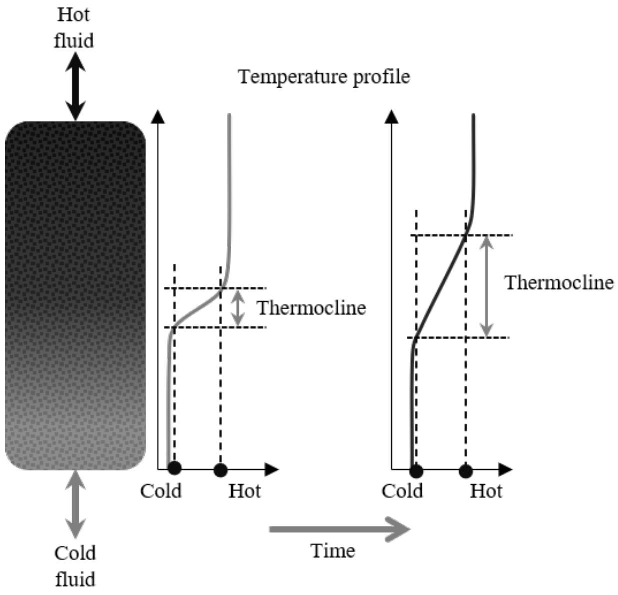

Figure 2.2: Thermocline formation for a STES storage as time progresses. Modified from [23].

making them preferable for high-temperature applications [29]. Some additional advantages of packed-bed systems include: the nonexistence of operating temperature constraints due to chemical instability of the HTF and the solid material. The operating pressure can be close to atmospheric, thus avoiding the need for complex sealings. Moreover, the thermal storage can be coupled directly to the heat source, thereby eliminating the need for heat exchangers between the HTF and thermal storage medium.

Packed-bed systems have been tested using concrete, natural rock, and compound materials, among other alternatives for the solid matrix [25, 18, 31]. Recently, the use of waste from the steel making and mining industries as filler materials in packed-beds has been analyzed. The goal is to reduce the investment cost inherently involved in two-tank molten salts designs, which are commonly used in concentrated solar power systems. Using a filling material can increase the theoretical energy density of the storage system by approximately 50% compared to a two-tank storage system, and the amount of HTF might be reduced by approximately 70% [32]. Moreover, if low-cost solid materials are employed, it would be possible to reduce the overall investment cost of the thermal storage system, leading to a significant reduction in the levelized cost of energy for concentrating solar plants as well as for other renewable technologies [33].

Many of the studies available in the literature focus their efforts on analyzing a single charge-discharge process [31, 34, 35, 36, 37]. Nevertheless, the understanding of a repeated cycling operation is essential in these systems, because from a thermodynamic point of view, the analysis of the cycle should consider the mixing effects, as well as the impact of every heat transfer mechanism in each phase of the operation [38, 39]. For instance, the start of the cycle implies that the storage is in the same initial state as for the previous cycle, implying that the entropy generated during the last cycle must be discarded to return the system to the initial conditions. Therefore, it is highly possible that the temperature profiles developed

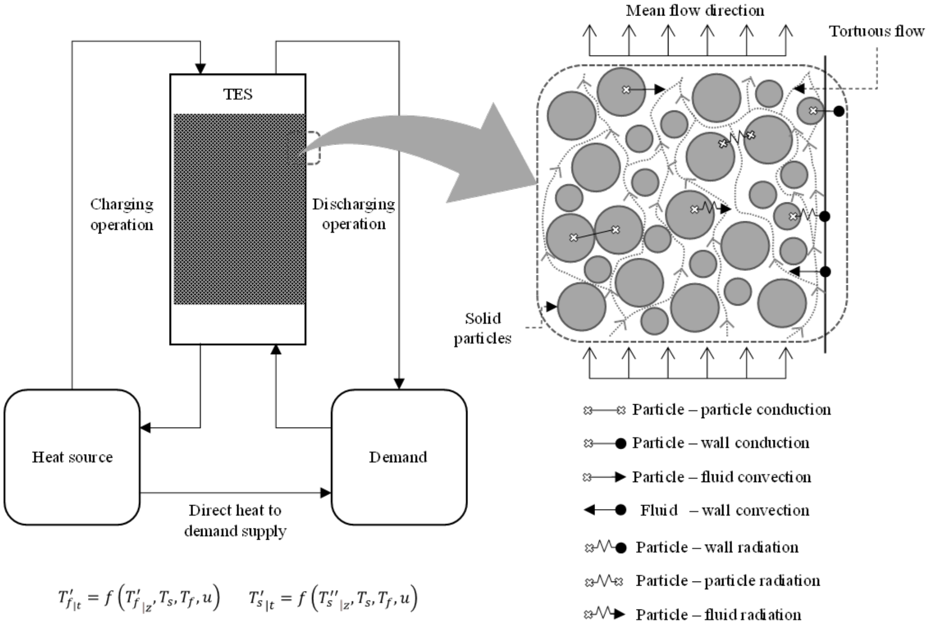

Figure 2.3: General scheme of a solid thermal energy storage system and internal heat transfer mechanisms. Modified from S. Kalaiselvam [29] and Burström et al. [30].

would present different shapes at each cycle, depending on the period between cycles. In this context, specific modeling techniques must be considered to aid the design and operating processes of packed-bed systems. As shown in Figure 2.4, a general modeling approach can be used to contemplate either single or multidimensional variables. Herein, an in-depth analysis of the different modeling approaches used for packed-bed storage is presented. We describe one-, two-, and three-dimensional (1D, 2D, and 3D, respectively) models, as well as the utilization of empirical correlations for simplified modeling. The radiation heat transfer during each phase of the operation is also investigated in deep.

2.2 Operation and key variables

The technical literature shows that using arrays of solid materials, such as rocks, facilitates the development of a system that relies on the abundance of storage materials and their consequent relatively low cost, along with a wide temperature range of applicability [40]. Nevertheless, the determination of essential parameters and design variables is crucial for enhancing the rate whereat heat transfer occurs between the fluid and the solid media, thereby reducing the power required to move such a fluid through the entire system [41]. It has been shown that the key parameters and variables for the operation of packed-bed storage systems include particle size, mass flow rate per unit of superficial area, fluid thermal properties, bed length, thermal losses through the walls, void fraction, packing material, fluid inlet temperature, wall structure, and ambient air conditions [36, 42, 43].

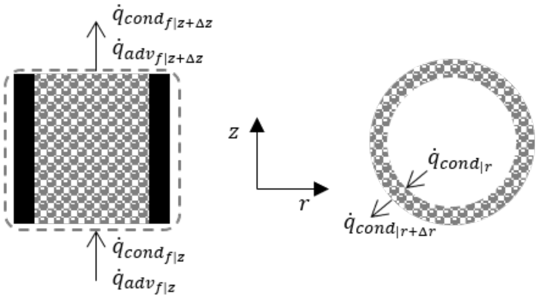

$$\frac{\partial T_f}{\partial t} = \dot{q}_{cond_f} - \dot{q}_{adv_f} + \dot{q}_{conv_f} \qquad \frac{\partial T_s}{\partial t} = \dot{q}_{cond_s} - \dot{q}_{conv_s}$$

$$\dot{q}_{cond_f} = \frac{k^a_{f_{eff}}}{\varepsilon \rho_f C_{p_f}} \frac{\partial^2 T_f}{\partial z^2} + \frac{k^r_{f_{eff}}}{\varepsilon \rho_f C_{p_f}} \left(\frac{1}{r} \frac{\partial T_f}{\partial r} + \frac{\partial^2 T_f}{\partial r^2} \right)$$

$$\dot{q}_{conv_f} = \frac{h_p a}{\varepsilon \rho_f C_{p_f}} (T_s - T_f)$$

$$\dot{q}_{adv_f} = u \frac{\partial T_f}{\partial z}$$

$$\dot{q}_{cond_s} = \frac{k_{s_{eff}}}{(1-\varepsilon)\rho_s C_{p_s}} \frac{\partial^2 T_s}{\partial z^2}$$

$$\dot{q}_{conv_s} = \frac{h_p a}{(1-\varepsilon)\rho_s C_{p_s}} (T_s - T_f)$$

Figure 2.4: General modeling approach for packed bed storage systems.

2.2.1 Charging and discharging processes

The charging process consists of making a hot fluid to flow through the solid storage material. However, the reverse process, i.e., discharging, occurs when the stored energy is regained by inducing a low-temperature flow through the hot solid material in the tank. The outlet heated fluid is then supplied to the demand system, which could be an industrial heat load or a power cycle [36]. Once the thermal energy is depleted, and if there is no power available from the primary heat source, the HTF is halted, which stops the forced convective heat transfer. As soon as the primary heat source is available, the charging cycle restarts [16]. Injecting and extracting energy from the packed-bed is not trivial; several key points need to be considered. In [44], the authors analyzed different experimental charging conditions and their effects on system performance. The analysis considered six charging scenarios that involved the initial stratification degree of the packed-bed, control of the charging temperature, and different cloud conditions. As reported by the authors, the time taken to charge the storage media is critically affected by the thermal properties of the material. Aly and El-Sharkawy [45] determined three key issues for the design and operation of packed-bed systems: (1) the energy employed during the charging process increases proportionally with the density and the specific heat of the storage material, while decreases the rate of the temperature rise during the process; (2) increasing thermal conductivity enables the elevation of the charging rate and amount of energy stored; and (3) a steel packed-bed exhibits a higher storage rate and capacity than a rock or an aluminum bed. Similarly, the latter material shows superior storage than rocks during the first charging hours.

For the discharging process, the operation of the system must consider the temperature decline in the outlet. In Mertens et al.'s work [46], it is shown that steam production using energy from a packed system requires the determination of the breaking temperature that is just above the operating sliding pressure mode of the turbine. After this point, the blades may be damaged owing to the moisture content of the steam. In such studies, the authors also proposed three discharging operational scenarios to evaluate the sensitivity of the packed-bed storage system: (1) a complete discharging process, (2) a cloudy day that shortens the charging process reduced by 2 h, and (3) a discharging that occurs with a 2 d delay due to a turbine breakdown. This evaluation suggests that a packed-bed of rocks might be inadequate for long-term storage considering the thermal losses if the mass flow is considered constant for the charging and discharging operations. However, it is acceptable for short storage periods, as well as sufficiently flexible to tolerate a variety of charging and discharging profiles during steady-state conditions [46].

2.2.2 Storage structure

Figure 2.5 shows a brief depiction of the typical structure for a packed-bed system. As observed in the figure, most packed-bed systems require a containment structure that contains the storage material and facilitate the flow of the HTF, and withstand considerable cyclic stresses. Large-scale designs commonly consider concrete as the primary building material for such structures [47]. Thus, the walls are often composed of several layers of concrete that have high mechanical stability on the packed-bed side and a combination of low-density concrete and insulation at the outside [25]. Other designs have also considered the use of steel alloys in layers with insulating materials and aluminum as the external cover [26]. Inside the tank, besides the heat storage material, some investigations have proposed the use of flow homogenizers at both sides of the tank and support plates to ensure that the HTF is evenly distributed over the cross-section, thereby improving the overall efficiency of the system [26, 46]. In general, packed-bed containers are cylindrical, a shape that presents low mechanical problems and minimizes the lateral surface area for a given cross-section surface, aiming to improve the flow's uniformity [48]. Some studies present the analysis of underground conical truncated tanks that reduce inconveniences, such as rock fracture and tank deformation [27]. Ortega-Fernández et al. [31] concluded that a cylindrical tank should be selected to optimize the thermal performance of the system, and a conical geometry would only be justified for its mechanical performance. Nonetheless, as previously mentioned, according to Marti et al. [49], the most efficient shapes follow a truncated cone with a smaller cross-section on top, a different result compared to other studies where cylindrical and/or inverted cone shape tanks are the recommended options. In any case, the cone angle should be evaluated for each specific design to determine the appropriate efficiency, outflow temperature, height, and volume for determining the excavation foundation [20, 27]. For cylindrical tanks, the aspect ratio is also crucial to evaluate, Ortega-Fernández et al. [31] indicating that for a storage unit of 3 m^3 and a storage capacity of 1 MWh_t a high ratio promotes a more significant amount of energy released because it improves stratification. Nevertheless, it is stated that values over two do not represent a considerable improvement in the system's performance.

2.2.3 Materials and thermophysical properties

For packed-bed storage systems, two phases are involved: a solid medium that allows the storage of heat and an HTF that creates the stratification of temperature in the tank. Thus, a key parameter for material selection is the thermal capacity (ρCp) of the storing media. Ismail and Stuginsky [50] (*apud* [51]) indicate that thermal capacity, thermal conductivity, and particle size dictate the performance of the storage system. This conclusion was achieved under the assumptions that the thermal properties of the particle do not vary with tempera-

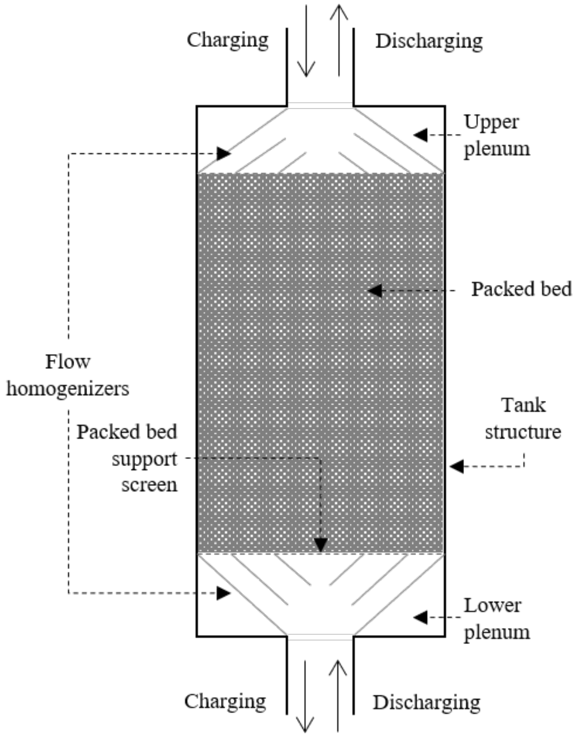

Figure 2.5: Scheme of a typical structure for packed-bed heat storage tank. Modified from Gautam and Saini [20].

ture, and by neglecting the radiation heat transfer and the temperature gradients within the particles. A high thermal capacity leads to a high energy density, which results in a reduction in the volume of the storage vessel, and consequently, the capital cost [17]. Similarly, high thermal conductivity induces a higher rate for thermal charging [45], thereby allowing coupling to different applications. Furthermore, properties such as thermal stability, temperature operation range, and costs of implementation, among others, need to be carefully considered in the selection of sensible heat storage materials.

Solids

Common solid materials for packed-bed systems include concrete and castable ceramics. These materials are considered as reliable at high temperatures and exhibit good thermal and mechanical properties at a relatively low cost [52, 53]. Moreover, aggregates, such as iron oxide and alumina (Al_2O_3) increase the operating temperature over 600 °C [54]. By using aggregates such as rubber, recycled materials, and/or silica, in different water/cement ratios, the thermal properties of concrete mixtures can be modified. For instance, El-Sharkawy et al. [55] improved the specific heat of a regular concrete mixture from 0.801 J/gK to 1.492 J/gK by adding silica fume and superplasticizer.

The use of rocks as filler material in TES systems has been considered an interesting research topic because of their high availability and practically no purchase cost. Grosu et al. [56] analyzed the thermophysical properties of river rocks and magnetite, and verified their feasibility owing to their high density and average specific heat capacity, as described in Table 2.1. A similar approach was followed by Grirate et al. [51], they analyzed a variety of

Table 2.1: Summary of SHS materials used as fillers for packed-bed systems.

Material	ρ [kg/m^3]	c_p [J/gK]	ρc_p [kJ/m^{3}K]	k [W/mK]	Temperature range [°C]	Cost [€/t]	Ref.
Alumina	3960	0.8	3168	18	< 1773	5000	[18, 22]
Cast iron	7200	0.56	4032	37.0	200 - 400	880 [13]	[12]
Cast steel	7800	0.6	4680	40.0	200 - 700	4430 [13]	[12]
Concrete	2750	0.916	2516	1.0	200 - 400	44	[53, 13]
Castable ceramics	3500	0.866	3031	1.35	100 - 390	4500 [61]	[53]
Htun Concrete	2720	1.928	5244	2.465	–	–	[57]
BOF-Slag[a]	3972	0.91	3614	2.15	180 - 320	0	[56]
Magnetite	5155	0.85	4382	2.7	180 - 320	135	[56]
River rock	2835	1.04	2948	2.1	180 - 320	90	[56]
Quartzite	2570	1.185	3046	3.5	100 - 400	0.5 [62]	[51]
Cipolin	2800	1.136	3181	1.6	100 - 400	–	[51]
EAF Slag 1[b]	3430	0.933	3200	1.43	100 - 1100	80 [63]	[18]
EAF Slag 2[b]	3770	0.912	3374	1.41	100 - 1100	80 [63]	[18]
IFS [c]	2583	0.738	1906	–	100 - 1000	–	[17]
C Slag[b]	3610	0.975	3520	1.75	100 - 1000	–	[58]
S Slag[b]	4260	0.858	3655	1.736	100 - 1000	–	[58]

[a] Basic Oxygen Furnace Slag,
[b] Electric Arc Furnace Slag,
[c] Induction Furnace Slag

rocks, such as quartzite and cipolin (materials that are relatively abundant in the Moroccan region), and concluded that they were good candidates to be considered in TES using thermal oil as the HTF. These materials do not exhibit corrosive behavior when in contact with oil and have a high thermal capacity (high density and high specific heat). Similarly, Htun et al. [57] reported a comparison between different mixtures of water, cement, sand, limestone, and steel fiber, which are local materials in Thailand.

Metal alternatives, such as cast iron and stainless steel, present benefits regarding their thermophysical properties (see Table 2.1). However, they present higher costs per kilogram of material (see Table 2.1). Several studies have considered industrial by-products or inorganic industrial waste materials as aggregates on solid mixtures or as storage media. The main alternatives that have been analyzed consist of ferrous by-products, especially from the steelmaking industry, which produces various slags depending on the process considered, such as electric arc and induction furnaces. Such materials present high thermal capacity and thermal stability at high temperatures (up to 1000 °C), because of their ferrous composition [18, 17, 56, 58]. Other authors have considered industrial by-products and recycled materials from the copper and potash industry, as it was analyzed in Navarro et al. [59] and Miró et al. [60], respectively.

Fluids

In packed-bed systems, the HTF must be compatible with the solid material and present suitable thermophysical properties, such as specific heat, thermal conductivity, viscosity, density, and thermal stability [64]. In some configurations, the HTF circulates from the solar field to the TES systems; however, some designs consider a separate HTF for the solar field that captures the solar radiation at the collectors, thereby requiring a heat exchanger to transfer the

Table 2.2: Summary of HTF for packed-bed systems.

Material	ρ [kg/m^3]	c_p [J/gK]	ρc_p [kJ/m^{3}K]	k [W/mK]	μ [Pa·s]	Temperature range [°C]	Cost [€/t]	Ref.
Air*	0.5	1.075	0.537	0.05	$3.4{\cdot}10^{-5}$	–	-/-	[48]
CO_2 (P=150bar)	144.2	1.261	181.8	0.06699	$3.952{\cdot}10^{-5}$	>550	1240	[84]
Water	990	4.180	4138	0.64	$5.8{\cdot}10^{-4}$	0-100	–	[48]
Therminol VP-1	904	2.075	1876	0.11	$0.37{\cdot}10^{-3}$	12-400	25000	[67]
Therminol 66	845	2.380	2011	0.10	$5.7{\cdot}10^{-4}$	0-345	–	[48]
Xceltherml 600	736	2.643	1586	0.13	$0.55{\cdot}10^{-3}$	-29-316	–	[67]
JaCCO	802	2.509	2012	0.11	$1.73{\cdot}10^{-3}$	3-210	835	[67]
Vegetable oils	–	–	–	0.13-0.14	$1.2\text{-}3.5{\cdot}10^{-3}$	-11-250	400-1200	[68]
Solar salt	1835	1.510	2771	0.52	$1.8{\cdot}10^{-3}$	220-600	2.6 [74]	[48]

* Properties at average operating temperature

thermal energy to the HTF used in the TES system. This scheme is commonly employed in systems using thermal oil, a common solution applied in parabolic trough solar power plants. Thermal oils Therminol VP-1 and Therminol-66 have been analyzed in packed-bed systems, thereby verifying the feasibility of dual-media TES systems, and presenting controllable and predictable results regarding the behavior of the thermocline [65, 66, 51]. Other types of oils, such as the crude oil of Jatropha Curcas (JaCCO) [67], and vegetable oils [68] have also been analyzed as HTFs in packed-bed systems. These alternatives presented higher potential regarding their compatibility with the filler materials considered (quartzite, alumina, blast furnace slag). However, they have an operating temperature limit of approximately 235 °C, which is lower than the 400 °C for thermal oils [68].

Currently, two-tank TES systems using molten salts as storage media, dominate the new developments in the CSP industry, especially in central receiver systems [69]. This fluid is used simultaneously as a HTF and storage medium. It has been tested in packed-bed configurations to improve the system's performance and reduce capital costs. The molten salt-packed-bed system has been validated through a series of compatibility tests, considering filler materials such as different types of steel slag [70, 71], quartzite, and other natural rocks [72, 73]. The results concluded the feasibility of using molten salt as HTF in packed-bed tanks and the high potential that presents for a significant cost reduction in CSP systems [74, 75, 76, 77, 78, 79].

Among the gaseous fluids, using air as the HTF allows using a fluid with negligible cost, high availability, no toxicity, and stability at high temperatures. Table 2.2 shows that the thermophysical properties of air are in the average range of the properties observed for other alternatives. The use of air as the HTF has been extensively analyzed and tested under a wide range of conditions [16, 41, 80, 81, 82]. These studies have proven the feasibility of different packed-bed configurations using air as the HTF. Other deeply analyzed alternatives are steam and supercritical CO_2, where sCO_2 concentrates the current research efforts, considering its high performance when coupled with advanced Brayton cycles [83, 84].

2.3 Empirical heat transfer coefficients

Determining heat transfer coefficients through measurements is even more difficult than in mass transfer studies. Thus, considering the heterogeneity of the modeling process, different assumptions have been considered to simplify the analysis of heat transfer mechanism between the HTF and the solid packing material. Numerous correlations for predicting heat transfer coefficients in packed beds have arisen in the technical literature.

2.3.1 Conduction

Some authors have proposed that the heat transfer interaction between a solid packed-bed and a fluid may be represented by a parameter called *effective thermal conductivity.* The physical phenomenon involved in the effective thermal conductivity is shown in Figure 2.6. The heat conduction between the contact points of two adjacent particles is a function of the number of contact points and their contact area. Fluid may be trapped between particles, such that it plays a relevant role in heat conduction through fluid conduction. Furthermore, fluid motion may be present in the vicinity of the particles that interact with the particles by convection.

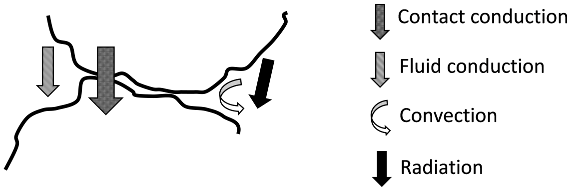

Figure 2.6: Schematic of the physical phenomena involved in effective thermal conductivity in packed beds.

There are two predominant approaches to model packed-bed systems: (1) models that consider a thermal gradient within the particles (Biot number > 1) [85], and (2) continuous models (Biot $\ll 1$). Table 2.3 presents some of the continuous models, including models for single and two phases. The single-phase model assumes that the fluid and solid are at the same temperature; therefore, the axial effective thermal conductivity (k^a_{eff}) is highly dependent on the thermal conductivity of the solid and the fluid when radiation effects are not considered [86]. The two-phase models consider that the fluid and solid have different temperatures, as two interacting media by heat advection. Some authors have proposed that k^a_{eff} affects only the solid phase of two-phase models [87], as shown in equations (2) and (3) in Table 2.3, whereas other authors [88, 89] have suggested that the effective thermal conductivity affects both phases, proposing particular expressions for the solid and fluid, as presented in equations (4) and (5) in Table 2.3.

The models shown in Table 2.3 are based on a 1D approach that considers only axial conduction. This 1D approach may be extended to a 2D model by considering a term that includes the radial effective thermal conductivity k^r_{eff}.

Table 2.4 shows some of the effective thermal conductivity expressions that are included in the continuous models. Figure 2.7 shows some of the correlations proposed in the literature for the motionless stagnant conductivity (k^0_{eff}). They are presented as a function of the void

Table 2.3: Effective conductivity expressions in continuous models

Model	Equation	Ref.
One-phase model	(1) $(\rho_s(1-\varepsilon)C_{p,s}+\rho_f\varepsilon C_{p,f})\frac{\partial T}{\partial t}=k^a_{\mathrm{e}ff}\frac{\partial^2 T}{\partial z^2}-\rho_f\varepsilon C_{p,f}u\frac{\partial T}{\partial z}$	[86]
Two-phase model	(2) $\rho_f\varepsilon C_{p,f}\frac{\partial T_f}{\partial t}=-\rho_f\varepsilon C_{p,f}u\frac{\partial T_f}{\partial z}+h_p a\left(T_s-T_f\right)$ (3) $\rho_s(1-\varepsilon)C_{p,s}\frac{\partial T_s}{\partial t}=k^a_{\mathrm{e}ff}\frac{\partial^2 T_s}{\partial z^2}-h_p a\left(T_s-T_f\right)$	[87]
Two-phase model	(4) $\rho_f\varepsilon C_{p,f}\frac{\partial T_f}{\partial t}=-\rho_f\varepsilon C_{p,f}u\frac{\partial T_f}{\partial z}+k^a_f\frac{\partial^2 T_s}{\partial z^2}+h_p a\left(T_s-T_f\right)$ (5) $\rho_s(1-\varepsilon)C_{p,s}\frac{\partial T_s}{\partial t}=k^a_s\frac{\partial^2 T_s}{\partial z^2}-h_p a\left(T_s-T_f\right)$	[88, 89]

fraction. The determination of $k^0_{\mathrm{e}ff}$ assumes an isotropic behavior on the bed. The plotted correlations consider air as an HTF, limestone as the solid media, and their properties are evaluated considering a temperature of 300 °C. According to Díaz-Heras et al. [85], for the most common range of $10^1 \leq k_s/k_f \leq 10^2$ and below 900 °C, similar results are obtained from the correlations published by Hadley [90], Zehner and Schlünder [91], Krupiczka [92], and Gonzo [93]. The $k^0_{\mathrm{e}ff}$ correlations in Table 2.4 do not consider the radiative effects. Most of the motionless stagnant conductivity correlations that take radiation into account ($k^{0,rad}_{\mathrm{e}ff}$) have been developed for nuclear applications. Some authors, such as [94, 95, 96, 97] have stated that radiation effects are important when the packed temperature is higher than 900 °C [86]. Figure 2.8 presents the $k^{0,rad}_{\mathrm{e}ff}$ correlations as a function of void fraction. The correlations were evaluated considering a packed temperature of 500 K and 1000 K, and a difference of an order of magnitude was observed. The proposed correlations show large discrepancies, but they seem to converge as the porosity falls within a range of 0.5 and 0.7. The axial effective thermal conductivity ($k^a_{\mathrm{e}ff}$) is influenced by $k^0_{\mathrm{e}ff}$ (first term) and a second term, which is a function of fluid motion and fluid properties ($RePr$). Several authors [98, 99, 100] have proposed values for the proportional constant (α_a) of the second term. Figure 2.9 shows the $k^a_{\mathrm{e}ff}$ correlations as a function of the Reynold numbers. The propositions made by Elsari and Hughes [99] and Kuwahara et al. [100] are closer than Yagi et al. [98], which suggests significantly lower values. Díaz-Heras et al. [85] have presented the influence of $k^a_{\mathrm{e}ff}$ during the charge and discharge processes and concluded that the convection phenomenon is much faster than the effects of $k^a_{\mathrm{e}ff}$; thus, the uncertainties on the predicted values are less important. Furthermore, there is a lack of correlation for estimating $k^a_{\mathrm{e}ff}$ when the airflow and heat flux are present in the same direction. In the second formulation of the two-phase model, the axial effective thermal conductivity for the fluid k^a_f and solid k^a_s are required. Ismail and Stuginsky [50] proposed correlations to calculate k^a_f and k^a_s as shown in Table 2.4. The correlations proposed for k^r_{eff} are presented in Figure 2.10, and they show similar behavior to $k^a_{\mathrm{e}ff}$ correlations, and are not highly influenced by variations in the airflow ($\alpha_r < 0.1$) [85]. k^r_{eff} presents values up to two orders of magnitude lower than $k^a_{\mathrm{e}ff}$.

2.3.2 Convection: Volumetric heat transfer coefficient

The convective heat transfer coefficient represents the interaction effect between a flowing fluid and a solid surface. This effect occurs in the complete volume of the porous solid matrix. Usually, for packed beds, it is considered as the volumetric coefficient of the complete volume as a field property, which depends on the flow regime and void fraction of the porous solid

Table 2.4: Effective thermal conductivity.

Model	**Equation**	**Reference**
Motionless stagnant conductivity	k^0_{eff}	[90, 91, 93] [101, 92, 102]
Motionless stagnant conductivity (including radiation)	$k^{0,rad}_{eff}$	[103, 104] [105, 106]
Axial effective thermal conductivity	$k^a_{eff} = k^0_{eff} + k_f \alpha_a \,\mathrm{Re}\,\mathrm{Pr}$	[98, 99, 100]
Axial effective thermal conductivity fluid	$k^a_f = \begin{cases} 0.7\varepsilon k_f & \mathrm{Re} \leq 0.8 \\ 0.5\,\mathrm{Pr}\,\mathrm{Re}\,k_f & \mathrm{Re} > 0.8 \end{cases}$	[50]
Axial effective thermal conductivity solid	$k^a_s = k^a_{eff} - k^a_f$	[50]
Radial effective thermal conductivity	$k^r_{eff} = k^0_{eff} + \alpha_r \,\mathrm{Re}\,\mathrm{Pr}\, k_f$	[107, 100, 108]

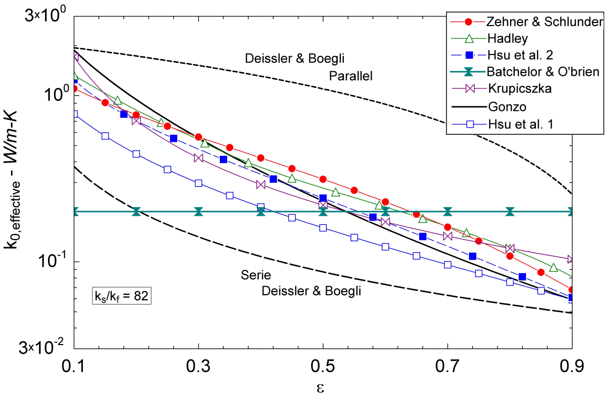

Figure 2.7: Motionless stagnant conductivity correlations according to Table 2.4.

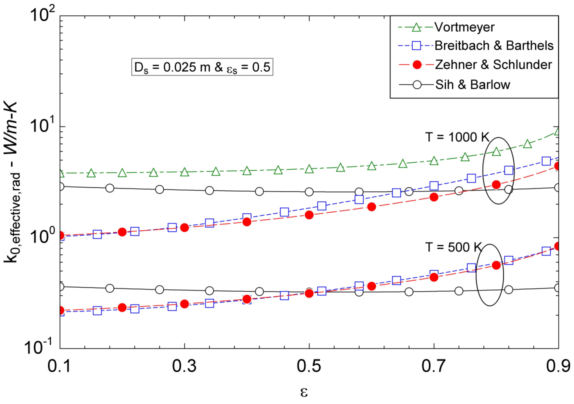

Figure 2.8: Motionless stagnant conductivity with radiation included according to Table 2.4.

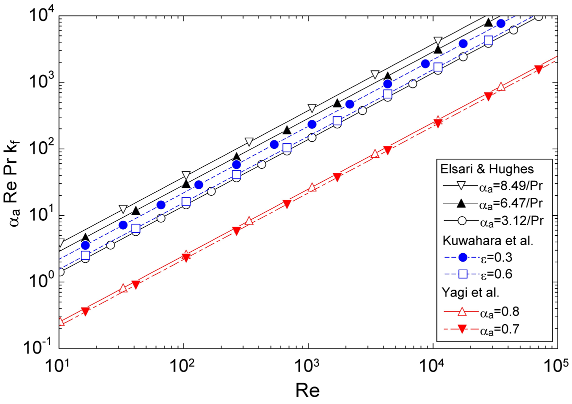

Figure 2.9: Axial effective thermal conductivity according to Table 2.4.

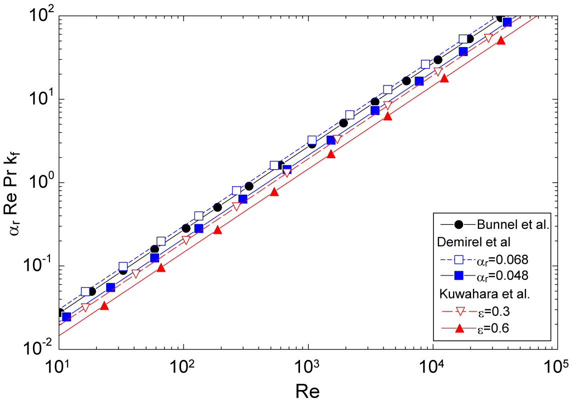

Figure 2.10: Radial effective thermal conductivity according to Table 2.4.

matrix. Nevertheless, because of the different geometries that the packed bed can present, the convective term varies for different configurations. The volumetric convection heat transfer coefficient is proposed as $h_v = c_1 \left(c_G\right)^{c_2}$, where c_1 and c_2 are geometry factors that depend on the void fraction and/or on the characteristic pore diameter of the solid matrix, and c_G is the flow term usually dependent on the mass flow rate or Reynolds number. Several studies have addressed the term h_v from the aforementioned expression, initially proposed by Löf and Hawley [109], where the most relevant expressions are listed in Table 2.5. In their results, Dunkle [110], Alanís et al. [111], Chandra and Willits [41], Coutier and Farber [42], and Wu and Hwang [112] presented correlations based on experimental data over irregular packed beds using hot air as the HTF. The differences observed in Figure 2.11 between these five correlations are due to the differences in porosity and distribution in each experimental set-up. Thus, it is recommended to employ these correlations for heat exchange/storage devices that use randomly distributed packed beds with only air as the HTF. However, Whitaker [113], Gupta et al. [114], Gunn and De Souza [115], and Wakao et al. [116] presented statistical analyses of the experimental data available in the literature. The basis of the analyses includes different fluids, reducing the accuracy in some cases, but giving a wider range of applicability for the correlations.

Table 2.5: Convective heat transfer correlations defined in the literature.

Correlation	**Range**	**Reference**
$h_v = 0.79 \cdot \left(\frac{G}{\mathrm{d}}\right)^{0.7}$ G: Air mass flow per area unit	$400 \leq \frac{G}{\mathrm{d}} \leq 10^4$ $\left(\mathrm{lb\ h^{-1} ft^{-1}}\right)$	[109]
$Nu = \frac{(1-\varepsilon)Pr^{1/3}}{\varepsilon}\left(0.5 \cdot \left(\frac{Re}{1-\varepsilon}\right)^{0.5} + 0.2 \cdot \left(\frac{Re}{1-\varepsilon}\right)^{2/3}\right)$	$100 \leq Re$ $\varepsilon \leq 0.65$	[113]
$Nu = \frac{Pr^{1/3}}{\varepsilon} \cdot \left(2.876 + 0.3023 \cdot Re^{0.65}\right)$	$10 \leq Re$	[114]
$Nu = 2.4 \cdot Re^{0.7} Pr$	$10 \leq Re \leq 10^5$	[110]
$h_v = 824 \cdot \left(\frac{G}{\mathrm{d}}\right)^{0.92}$	$10 \leq Re \leq 10^5$ and $\varepsilon = 0.42$	[111]
$Nu = \left(7 - 10 \cdot \varepsilon + 5 \cdot \varepsilon^2\right)\left(1 + 0.7 \cdot Re^{0.2} Pr^{1/3}\right)$ $+ \left(1.33 - 2.4 \cdot \varepsilon + 1.2 \cdot \varepsilon^2\right) Re^{0.7} Pr^{1/3}$	$10 \leq Re \leq 10^5$ and $0.35 \leq \varepsilon$	[117]
$Nu = 2 + 1.1 Pr^{1/3} Re^{0.6}$	$100 \leq Re \leq 10^5$	[116, 118]
$\frac{h_v \mathrm{d}^2}{k} = 1.45 \left(\frac{\rho U \mathrm{d}}{\mu}\right)^{0.7}$ $\frac{h_v \mathrm{d}^2}{k} = 2.72 \left(\frac{\rho U \mathrm{d}}{\mu}\right)^{0.7}$	$100 \leq Re \leq 10^3$ and $0.38 \leq \varepsilon \leq 0.5$ $500 \leq Re \leq 5 \cdot 10^4$ and $0.38 \leq \varepsilon \leq 0.5$	[41]
$h_v = 700 \cdot \left(\frac{G}{\mathrm{d}}\right)^{0.76}$	$0.04 \leq G \leq 0.24$	[42]
$Nu = 0.32 Re^{0.59}$ $Nu = 8 + 0.004 Re$ $Nu = 0.0032 Re$ $Nu = 0.0022 Re$	$200 \leq Re \leq 7 \cdot 10^3$ and $\varepsilon = 0.39$ $\varepsilon = 0.48$ $\varepsilon = 0.73$ $\varepsilon = 0.97$	[112]

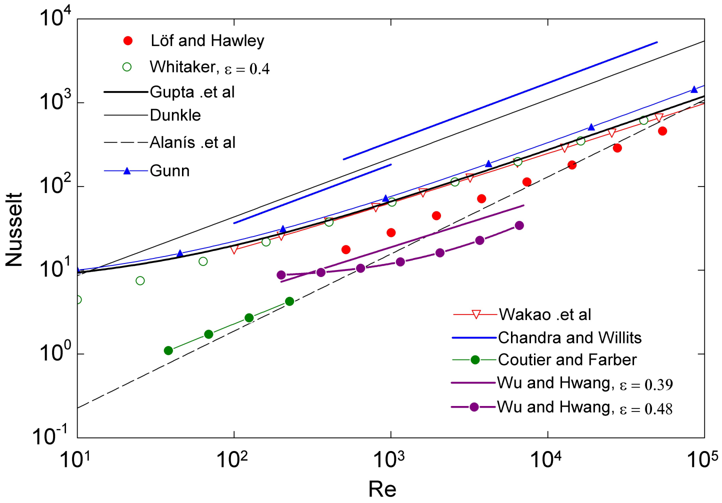

Figure 2.11: Heat transfer correlations presented at Table 2.5.

2.3.3 Fluid/wall heat transfer coefficient

The thermal behavior at the interface between the bed, fluid, and wall is highly relevant to accurately assess the performance of packed-bed storage. Some of the models that have been developed to describe the wall heat transfer coefficient are presented in Table 2.6. The penetration theory suggests that part of the fluid that approaches the wall exchanges heat with the wall reaching thermal equilibrium, and leaves away from the wall being replaced by a new fraction of fluid [119]. The boundary film theory assumes that the void fraction is significantly close to the wall surface [120], decreasing the effective radial thermal conductivity and increasing the axial gas velocity [121]. This film flowing almost freely may interact with the wall by diffusion, either in laminar or turbulent flow regimes. In this context, the effect under turbulent flow might be more significant because the fluid has a higher relative velocity. However some diffusion effects may be significant in flowing gases and comparable to the convective effects [122]. The findings shown in [123] suggest a thermal interaction process in a wall/packed-bed/fluid system. It is schematized in Figure 2.12, where the solid near the wall assumes thermal conduction through the gas near the contact points and radiation between particles and wall surfaces. Within the void (independent of flow conditions), it is considered thermal conduction through the fluid in the direction normal to the flow direction and radiation exchange between the wall and the particles that are not in contact with it. Depending on the flow condition, the convective effects are considered in the void at the boundary film and impacting the flow mixing.

Table 2.6 shows some of the correlations developed to predict the heat transfer coefficient in a wall-bed-fluid interface, which are mainly dependent on a modified Reynolds number, expressed as:

$$Re = \frac{G\mathrm{d}}{\mu} \tag{2.1}$$

where G is the mass flux ($G = \dot{m}/A$), which is determined by assuming an empty tube

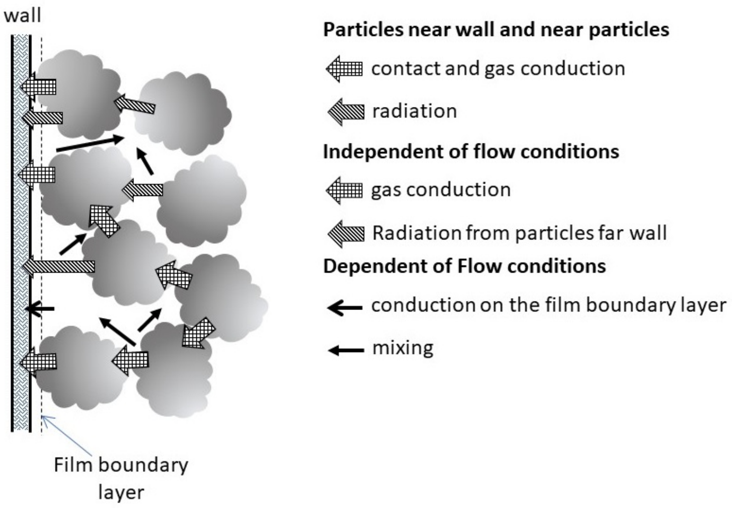

Figure 2.12: Wall-packed-fluid thermal interaction.

cross-sectional area, and the characteristic length is the particle diameter d.

Table 2.6: Correlations developed to predict heat transfer coefficient in the wall-bed-fluid interface.

Correlation	**Range**	**Reference**
$Nu_w = (0.95 : 1.44)\left(\frac{\mathrm{Re}}{\varepsilon}\right)^{0.5}$	$80 < \mathrm{Re}/\varepsilon < 5000$	[119]
$Nu_w = \begin{cases} 0.6\mathrm{Pr}^{1/3}\mathrm{Re}_p^{0.5} \\ \mathrm{Pr}^{1/3}\mathrm{Re}_p^{0.8} \end{cases}$	$1 < \mathrm{Re} < 40$ $40 < \mathrm{Re} < 2000$	[124]
$Nu_w = 2.42\mathrm{Re}^{1/3}\mathrm{Pr}^{1/3} + 0.129\mathrm{Re}^{0.8}\mathrm{Pr}^{0.4} + 1.4\mathrm{Re}^{0.2}$	$\mathrm{Re} > 40$	[122]
$Nu_w = 0.203\mathrm{Re}^{1/3}\mathrm{Pr}^{1/3} + 0.220\mathrm{Re}^{0.8}\mathrm{Pr}^{0.4}$	$\mathrm{Re} > 40$	[125]
$Nu_w = \left(1 - 1.5\left(\frac{\mathrm{d}}{D}\right)^{1.5}\right)\mathrm{Pr}^{1/3}\,\mathrm{Re}^{0.59}$	$3 < \frac{D}{\mathrm{d}} < 12$	[126]

Figure 2.13 shows a comparison of the heat transfer coefficient correlations presented in Table 2.6, which are evaluated using air as working fluid. Most of the correlations were developed for the mass transfer analysis. Therefore, the correlations estimate a wide range of Nusselt number values, showing differences over one order of magnitude. Beek's [125] and Yagi and Wakao's correlations [124] show similar behavior. Dixon et al.'s correlation [126] is evaluated only within the range $3 < D/\mathrm{d} < 12$, overpredicting (in comparison with Beek's [125]) the heat transfer coefficient in the range of Reynolds number below 100, and underpredicting the heat transfer coefficient for Reynolds numbers higher than 100. Hanrattry's correlation [119] is evaluated for different constants $(0.95 - 1.44)$ and different void fractions $(\varepsilon = 0.3 - 0.6)$. However, the predicted heat transfer coefficient calculated using Hanrattry's correlation [119] shows a large uncertainty. The prediction from Thoenes and Kramers's correlation [122] differs largely from the others for small Reynolds numbers. Indeed, none of the presented correlations have been validated for small Reynolds numbers [127].

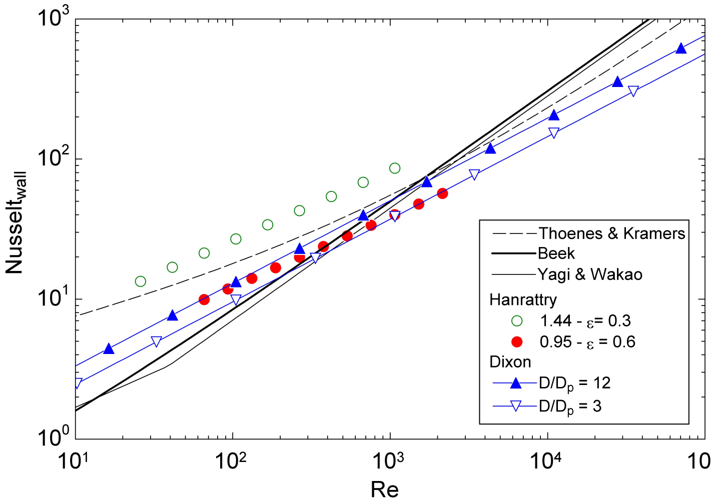

Figure 2.13: Heat transfer correlations presented at Table 2.6.

2.3.4 Pressure drop

Packed beds commonly present excellent heat transfer capacity owing to their large exchange area. Nevertheless, the large exchange area implies an increment in the hydraulic resistance (or body forces) of the porous media to the flow. Based on the work developed by Whitaker [128], Kaviany [129] derived the momentum equation for a porous medium, where the volumetric body forces include the drag force in the flow, related to the presence of the solid phase. This is expressed as follows,

$$\nabla P = -\frac{\mu}{K} u_D - \frac{C_E}{K^{1/2}} \rho u_D u_D \tag{2.2}$$

where the first and the second terms on the right represent the microscopic viscous shear stress (Darcy's term) and the microscopic inertial force (Forchheimer's), respectively. Moreover, C_E is an empirical parameter, and K is the permeability term, which is related to the porosity and characteristic pore diameter.

In 1952, Ergun [130] proposed an empirical relation based on experimental results to determine the pressure drop in a packed bed for a wide range of Reynolds numbers, from 1 to 10^4, linking the expressions previously presented by Blake-Kozeny and Burke-Plummer [131]. Macdonald et al. [132] revisited Ergun's analysis [130] establishing the strong dependence of the inertial term with the shape of the bed elements. Dunkle [133] and Chandra and Willits [41] presented an experimental analysis of the pressure drop and heat transfer characteristics of packed beds of rock, using air as the HTF. Similar to Ergun's analysis [41] identified a strong dependence between the rock size, bed porosity, and air mass flow rate with the pressure drop of the storage system, but the correlations are restricted to their experimental conditions. Later, du Plessis and Woudberg [134] confirmed Ergun's equation [130] for uniform packed spheres using an analytical analysis. The correlations are detailed in Table 2.7, where the variable G is the air mass flux, U is the average velocity (Darcy's velocity, or superficial velocity), and L is the height of the tank.

Table 2.7: Pressure-drop correlations.

Correlation	**Range**	**Reference**
$\frac{\Delta P}{L} = 150\frac{(1-\varepsilon)^2}{\varepsilon^3}\frac{\mu U}{\mathrm{d}^2} + 1.75\frac{1-\varepsilon}{\varepsilon^3}\frac{GU}{\mathrm{d}}$	$1 \leq Re \leq 10^4$	[130]
$\frac{\Delta P}{L} = 1750\frac{\mu U}{\mathrm{d}^2} + 21\frac{GU}{\mathrm{d}}$	$1 \leq Re \leq 10^5$	[133]
$\frac{\Delta P}{L} = \begin{cases} \frac{180}{\varepsilon^{0.6}}\frac{(1-\varepsilon)^2}{\varepsilon^3}\frac{\mu U}{\mathrm{d}^2} + \frac{1.8}{\varepsilon^{0.6}}\frac{(1-\varepsilon)}{\varepsilon^3}\frac{GU}{\mathrm{d}} & \textbf{Smooth Solids} \\ \frac{180}{\varepsilon^{0.6}}\frac{(1-\varepsilon)^2}{\varepsilon^3}\frac{\mu U}{\mathrm{d}^2} + \frac{4}{\varepsilon^{0.6}}\frac{(1-\varepsilon)}{\varepsilon^3}\frac{GU}{\mathrm{d}} & \textbf{Rough Solids} \end{cases}$	$0.123 \leq \varepsilon \leq 0.919$	[132]
$\frac{\Delta P}{L} = \frac{\mu^2\varepsilon^{-2.6}}{\rho \mathrm{d}_p^3}\left(185\left(\frac{\rho U \mathrm{d}_p}{\mu}\right) + 1.7\left(\frac{\rho U \mathrm{d}_p}{\mu}\right)^2\right)$	$1 \leq Re \leq 10^3$ $0.3 \leq \varepsilon \leq 0.5$	[41]
$\frac{\Delta P}{L} = 25.4\frac{(1-\varepsilon)^{4/3}}{(1-(1-\varepsilon)^{1/3})(1-(1-\varepsilon)^{2/3})^2}\frac{\mu U}{\mathrm{d}^2} + 1.9\frac{(1-\varepsilon)}{2\varepsilon(1-(1-\varepsilon)^{2/3})^2}\frac{GU}{\mathrm{d}}$		[134]

2.4 Numerical modeling

The most common heat transfer model for packed beds is Schumann's model [135]. It is a 1D two-phase heat transfer model based on the assumption of ideal plug flow of the fluid across the packed-bed, not considering the conduction resistance in the solid particles [118]. The model is expressed by the following equations for the fluid and solid phases, respectively.

$$\frac{\partial T_f}{\partial t} = -u\frac{\partial T_f}{\partial z} + \frac{h_p a}{\varepsilon \rho_f C_{p_f}}\left(T_s - T_f\right) \tag{2.3}$$

$$\frac{\partial T_s}{\partial t} = -\frac{h_p a}{\left(1-\varepsilon\right)\rho_s C_{p_s}}\left(T_s - T_f\right) \tag{2.4}$$

where the subscripts f and s denote the fluid and solid phase, respectively, t represents the time, and z is the axial coordinate. Both equations are coupled by a heat transfer constant $K = h_p a$, as stated in Schumann's formulation [135], representing the heat exchange by convection between the solid particles and the fluid. h_p is the convective heat transfer coefficient between the fluid and the particles, $a = 6 \cdot \left(1-\varepsilon\right)/\mathrm{d}$ is the shape factor, which is the ratio of the surface area of the solids to the volume of a rock with an equivalent diameter d. u is the axial fluid velocity in the packed bed, ε is the void fraction of the packed bed, and ρ, C_p, and T are the density, specific heat, and temperature, respectively.

2.4.1 Single-phase models

From the two-phase *C-S* model, Vortmeyer and Schaefer [87] derived a single expression for heat transfer in a packed-bed, based on the interactions between the fluid and solid phases. The model does not consider the thermal equilibrium between the phases; however, two approaches can be used depending on the fluid phase's thermal capacity. If the thermal capacity of the fluid phase is much smaller than that of the solid, it can be neglected, and assuming that $\frac{\partial^2 T_f}{\partial z^2} = \frac{\partial^2 T_s}{\partial z^2}$, holds the following expression:

$$(1-\varepsilon)\,\rho_s C_{p_s}\frac{\partial T_s}{\partial t}=\left(k_0+\frac{G^2C_{p_f}^2}{h_p a}\right)\frac{\partial^2 T_s}{\partial z^2}-\dot{m}_f C_{p_f}\frac{\partial T_s}{\partial z} \tag{2.5}$$

where k_0 is the axial effective thermal conductivity proposed by Yagi et al. [98] and G is the fluid mass flux rate. Even though Vortmeyer and Schaefer [87] did not specify the ratio of the specific heat capacity between the phases, Anderson et al. [36] stated that for an alumina packed bed with air as the HTF, the volumetric heat capacity of the alumina is $\sim 2500-11500$ times higher than the air in the temperature range analyzed. Additionally, it is stated that the single-phase approach may be suitable when sCO_2 is employed as the HTF as the volumetric heat capacity ratio between the alumina and sCO_2 is ~ 29. Nevertheless, further research is required in this area to determine the specific limit of the heat capacity ratio between the phases.

For the cases wherein the thermal capacity of the fluid cannot be neglected, it is assumed that the temperature profile is moving across the bed with constant velocity w. Thus, the following expression holds:

$$w=\frac{GC_{p_f}}{\varepsilon\rho_f C_{p_f}+(1-\varepsilon)\,\rho_s C_{p_s}} \tag{2.6}$$

The single-phase equation for non-negligible thermal capacity fluids is obtained using the equivalence of the second derivatives in the same manner as in Equation 2.5, and introducing the expression: $\frac{\partial T_s}{\partial t}=-w\frac{\partial T_s}{\partial z}$; thus, Vortmeyer and Schaefer [87] proposed the following expression:

$$\begin{aligned}\left(\varepsilon\rho_f C_{p_f}+(1-\varepsilon)\,\rho_s C_{p_s}\right)\frac{\partial T_f}{\partial t}&=-GC_{p_f}\frac{\partial T_f}{\partial z}+\left(k_0+\frac{\left(w\,(1-\varepsilon)\,\rho_s C_{p_s}\right)^2}{h_p a}\right)\frac{\partial^2 T_f}{\partial z^2}\\&+\frac{w\,(1-\varepsilon)^2\,\rho_s C_{p_s}k_s}{h_p a}\frac{\partial^3 T_s}{\partial z^3}\end{aligned} \tag{2.7}$$

The third-order term in Equation 2.7 is relatively small [87]. It is crucial to consider the fact that using a packed-bed provides the option of working with different HTF, either in gaseous or liquid phases. Similarly, for the two-phase models, the equation proposed by Vortmeyer and Schaefer [87] can be extended for a 2D temperature distribution. For both models, the thermal losses can be accounted for by assessing the overall heat transfer coefficient of the tank (U_T). U_T considers the internal convection between the hot airflow and the tank's wall, the conduction resistance in each layer of the insulation of the wall, and the convection outside the tank. The following sections present in-depth other methods for characterizing the effects of the walls on the thermal behavior of the packed-bed.

2.4.2 Two-phase models

Continuous solid-phase model (*C-S*) The Schumann's model [135] is applicable for regimes with large Reynolds numbers [87]. Nevertheless, for small Reynolds domains, a new expression should be included in Equation 2.3 and Equation 2.4, related to the axial conduction through the solid phase. Thermal diffusion in the fluid might also be considered [118]; however, some authors neglect that effect, assuming that the thermal conductivity in the fluid is much smaller than the conductivity in the solid phase [16, 135, 136].

According to Littman et al. [137], the thermal conductivity of both solid and fluid phases should be evaluated in terms of the bed cross-sectional area. Thus, the governing equations of the *C-S* model are as follows:

$$\frac{\partial T_f}{\partial t} = \frac{k_{f_{eff}}}{\varepsilon \rho_f C_{p_f}} \frac{\partial^2 T_f}{\partial z^2} - u \frac{\partial T_f}{\partial z} + \frac{h_p a}{\varepsilon \rho_f C_{p_f}} \left(T_s - T_f\right) \tag{2.8}$$

$$\frac{\partial T_s}{\partial t} = \frac{k_{s_{eff}}}{\left(1-\varepsilon\right) \rho_s C_{p_s}} \frac{\partial^2 T_s}{\partial z^2} - \frac{h_p a}{\left(1-\varepsilon\right) \rho_s C_{p_s}} \left(T_s - T_f\right) \tag{2.9}$$

where $k_{f_{eff}}$ and $k_{s_{eff}}$ are the effective thermal conductivity for the fluid and solid phases, respectively.

An extended version of the *Continuous solid-phase model* considers heat conduction in the radial direction for the solid and fluid phases, yet some authors neglect the effect for the fluid phase [50]. This model should be applied when the wall influence on the storage tank is significant, inducing flow heterogeneity and thermal losses through the walls. Meier et al. [34] stated a lower limit where the flow heterogeneity near the wall can be neglected, which is $D/\mathrm{d} \geq 40$ [16], where D is the bed diameter and d the particle diameter.

Dispersed Concentric model The *Dispersed Concentric* (*D-C*) model proposes a more accurate approach for assessing the thermal behavior of a packed-bed. It assumes that the fluid flows in a dispersed plug flow regime, and the solid phase has intraparticle gradients with radial symmetry. The model was developed by Handley and Heggs [138], who proposed a numerical solution of the partial differential equation (PDE) system. Subsequently, Gunn and De Souza [115, 118], based on the assumption of the radial symmetry of the temperature profile within the particles, developed a study regarding the thermal frequency response to determine the dispersion coefficients in a packed-bed structure. The heat transfer model according to Handley and Heggs [138] is expressed as follows:

$$\frac{\partial T_f}{\partial t} = \kappa_{f_{ax}} \frac{\partial^2 T_f}{\partial z^2} - u \frac{\partial T_f}{\partial z} + \frac{h_p a}{\varepsilon \rho_f C_{p_f}} \left(T_s \Big|_{r=R} - T_f \right) \tag{2.10}$$

$$\frac{\partial T_s}{\partial t} = \kappa_s \frac{1}{r^2} \frac{\partial}{\partial r} \left(r^2 \frac{\partial T_s}{\partial r} \right) \tag{2.11}$$

where the temperature profile for the solid particle is solved using the following boundary condition:

$$k_s \left(\frac{\partial T_s}{\partial r} \right) = -h_p \left(T_s - T_f \right) \ \text{ at } \ r = R \tag{2.12}$$

Assuming that the packed-bed arrangement can be approximated as mono-sized spheres, r is the radial coordinate, while R represents the sphere radius, and $\kappa_s = \frac{k_s}{\rho_s C_{p_s}(1-\varepsilon)}$ is the thermal diffusivity coefficient of the solids.

The term $\kappa_{f_{ax}}$ is called the **dispersion coefficient**, which was initially determined by Gunn and De Souza [115]. Nevertheless, the proposed expression presents an anomalous behavior at low Reynolds numbers. Two years later, Wakao [139] proposed a different expression that shows a good response for low Reynolds flows, which is expressed as follows:

$$\kappa_{f_{ax}} = \frac{k_{\mathrm{e}ff_{ax}}}{\varepsilon C_{p_f} \rho_f} \tag{2.13}$$

where $k_{\mathrm{e}ff_{ax}}$ is the effective thermal conductivity in the axial direction proposed by Yagi et al. [98].

2.4.3 Three phases models

Using models that consider more than two phases provides a deeper approach for several key effects. As demonstrated by Hasegawa and Oshima [140], the void fraction of packed-beds decreases as the size distribution of particles spread is crucial for the pressure drop and for determining the amount of energy that a packed-bed can store. Few authors have studied the effects of a multisized arrangement of rocks and thermal analysis, which involves coupling a new equation for the energy balance.

Models based in wall temperature gradient Beasley and Clark [141] proposed an analysis in two dimensions of a packed-bed TES, considering both axial and radial dispersion of temperature, and a third equation for the temperature distribution on the wall.

$$\frac{\partial T_f}{\partial t} + u \frac{\partial T_f}{\partial z} = \frac{k^a_{f_{\mathrm{e}ff}}}{\rho_f C_{p_f}} \frac{\partial^2 T_f}{\partial z^2} + \frac{k^r_{f_{\mathrm{e}ff}}}{\rho_f C_{p_f}} \left(\frac{1}{r} \frac{\partial T_f}{\partial r} + \frac{\partial^2 T_f}{\partial r^2} \right) + \frac{h_p a}{\rho_f C_{p_f}} \left(T_s - T_f \right) \tag{2.14}$$

$$\left(1 - \varepsilon \right) \rho_s C_{p_s} \frac{\partial T_s}{\partial t} = h_p a \left(T_f - T_s \right) \tag{2.15}$$

$$\rho_w C_{p_w} \frac{\partial T_w}{\partial t} = k_w \frac{\partial^2 T_w}{\partial z^2} + h_w A^{\mathrm{i}}_w \left(T_f - T_w \right) + h_{ext} A^{o}_w \left(T_w - T_{\mathrm{ext}} \right) \tag{2.16}$$

where h_w is the heat transfer coefficient through the storage wall, h_{ext} the coefficient of global thermal losses to the environment, T_w and T_{ext} are the wall and the outside temperatures, the inner and outer areas of the container walls are defined as A_w^{i} and A_w^o, respectively. The thermophysical properties of the tank are also considered, such as the thermal conductivity k_w, density ρ_w, and specific heat C_{p_w}.

However, Hoffmann et al. [142] formulated a 1D transient model with three coupled equations: (1) one for the solid phase, (2) another for the HTF, and (3) the storage wall effects are accounted for as a third phase considering a heat transfer equation to model the thermal gradient developed, which are expressed as follows:

$$\varepsilon \rho_f C_{p_f} \left(\frac{\partial T_f}{\partial t} + u \frac{\partial T_f}{\partial z} \right) = k_{f_{eff}} \frac{\partial^2 T_f}{\partial z^2} + h_p a \left(T_s - T_f \right) + h_w \frac{A_{f,w}}{V_f} \left(T_w - T_f \right) \tag{2.17}$$

$$\left(1 - \varepsilon\right) \rho_s C_{p_s} \frac{\partial T_s}{\partial t} = k_{s_{eff}} \frac{\partial^2 T_s}{\partial z^2} + h_p a \left(T_f - T_s \right) + h_w \frac{A_{s,w}}{V_s} \left(T_w - T_s \right) \tag{2.18}$$

$$\rho_w C_{p_w} \frac{\partial T_w}{\partial t} = k_w \frac{\partial^2 T_w}{\partial z^2} + h_w \left(\frac{A_{f,w}}{V_f} \left(T_f - T_w \right) + \frac{A_{s,w}}{V_s} \left(T_s - T_w \right) \right) + h_{\text{ext}} \frac{A_{w,\text{ext}}}{V_w} \left(T_w - T_{\text{ext}} \right) \tag{2.19}$$

where V_f, V_s, and V_w are the fluid, solid, and wall volumes, respectively. $A_{f,w}$, $A_{s,w}$, and $A_{w,ext}$ are the areas between the fluid and the storage walls, the solid and the storage walls, and the storage walls and the outside, respectively. The other variables in the above-mentioned equations are the same as those described in subsection 2.4.2 regarding Beasley and Clark's formulation [141].

Comparing both approaches, the formulation proposed by Beasley and Clark [141] considered the radial dispersion in the fluid phase; thus, Equation 2.14 has an additional term contrasted to Equation 2.17. The thermal losses through the contact between the solid phase and the storage wall are not considered in the model proposed by Beasley and Clark [141], and is only considered the convective heat transfer between the fluid and solid phase, as in Schumann's model [135]. Nevertheless, Hoffmann et al. [142] included the diffusion term in the solid-phase equation and the thermal losses through the walls. This formulation can be understood as an extension of the *C-S* model. A similar approach was developed by Aly and El-Sharkawy [45] to study the effects of the wall temperature on packed-bed storage systems, which consists of a 2D two-phase model for the heat transfer equations, where the radial dispersion is also included in the equation for the solid phase. Aly and El-Sharkawy [45] solved the system for different wall temperatures, and one of the main conclusions of the work is that the wall temperature showed negligible effects on the phase temperatures along the bed centerline. Conversely, an increase in the wall temperature has a significant impact on the solids near the wall, and that behavior could be modeled considering that $T_s = T_s(r, z)$ because the wall temperature is a boundary condition in the radial direction. Thus, for design considerations, a 2-D formulation would be highly recommended.

Models based in multisized particles Odenthal et al. [143] proposed a three-equation model for packed-beds with an arrangement of different particle sizes. The formulation is based on Schumann's model [135] for the two solid-phase equations: one for the larger particles and the other for the smaller ones. As both particle sizes are in the same storage tank, it is defined as a *weighting factor* for the volume occupied w_v by an average size of spheres confined in the tank, denoted by d.

$$\mathrm{d} = w_v \cdot \mathrm{d}_1 + (1 - w_v) \cdot \mathrm{d}_2 \tag{2.20}$$

where d_1 and d_2 are the diameters of the large and small rocks, respectively. Thus, the three-equation model is expressed as follows:

$$\varepsilon \rho_f C_{p_f} \frac{\partial T_f}{\partial t} + \rho_f C_{p_f} u \frac{\partial T_f}{\partial z} = h_{p1} a_1 \left(T_{s1} - T_f\right) + h_{p2} a_2 \left(T_{s2} - T_f\right) \tag{2.21}$$

$$w_v \cdot (1 - \varepsilon) \rho_{s1} C_{p_{s1}} \frac{\partial T_{s1}}{\partial t} = h_{p1} a_1 \left(T_f - T_{s1}\right) \tag{2.22}$$

$$(1 - w_v) \cdot (1 - \varepsilon) \rho_{s2} C_{p_{s2}} \frac{\partial T_{s2}}{\partial t} = h_{p2} a_2 \left(T_f - T_{s2}\right) \tag{2.23}$$

where the subscripts 1 and 2 denote the large and small particles. Thus, the convective heat transfer coefficient h_p and the shape factor a must be evaluated for the respective diameter.

The previous equations constitute an extension of the two-phase model with an equivalent description of the heat transfer phenomenon. The energy balance for each type of particle couples with the HTF through their respective heat transfer coefficients. Therefore, the same assumptions considered by the Schumann's model [135] are applied in this formulation.

Mixed models The study performed by Esence et al. [24] stands out by introducing a combination of the dispersed concentric model (*D-C*) [138, 115] and the single-phase approach, which allows the analysis of the thermal behavior of a packed-bed composed of two different sizes of rocks. For relatively large particles, a modified *D-C* model is applied where the evolution of the thermal profile within the solids involves different behaviors in two periods. It considers a spherical solid with a uniform initial temperature $T_{r,0} = T_{r,\mathrm{ini}}$ during the first period, due to the heat exchange between the fluid and the external layers of the solid, inducing a change in the internal temperature profile in the solid, R_r to the radius of the thermal front δ (Figure 2.14a). In the second period, the thermal front is extended to the center of the solid, and the central temperature of the particle varies with time (Figure 2.14b). For both periods, a temperature profile following the distribution $T_r(r_r) = a r_r^2 + b r_r + c$ is assumed, where the coefficients of the polynomial are calculated analytically at each time-step. Thus, no numerical resolution is developed to solve the temperature profile, saving computing time with the approach exposed by Esence et al. [24].

A single-phase equation is established for the smaller particles by assuming that the solid and fluid phases are in thermal equilibrium. The model also includes an energy balance for

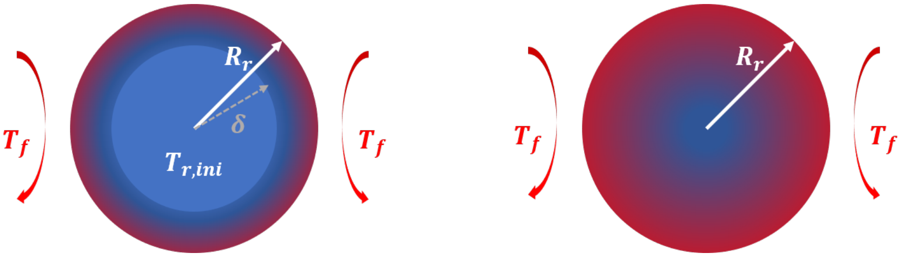

(a) First period of the particle thermal profile. (b) Second period of the particle thermal profile.

Figure 2.14: Temperature profile evolution within the particles according to Esence et al. [24].

the walls of the storage tank; hence, it suits the modeling of small storage tanks. The PDE system of the model proposed by Esence et al. [24] is expressed as follows:

$$\rho_r C_{p_r} V_r \frac{\partial \overline{T}_r}{\partial t} = h_{p_r} a_r \left(T_f - T_r \Big|_{r_r = R_r} \right) \tag{2.24}$$

$$\begin{aligned} \varepsilon C_{p_f} \frac{\partial \left(\rho_f \cdot T_f \right)}{\partial t} + w_{v,s} \rho_s C_{p_s} \frac{\partial T_s}{\partial t} + \varepsilon C_{p_f} \frac{\partial \left(\rho_f \cdot u_f \cdot T_f \right)}{\partial z} &= \frac{\partial}{\partial z} \left(k_{eff} \frac{\partial T_f}{\partial z} \right) \\ + h_{p_r} a_r \left(T_r \Big|_{r_r = R_r} - T_f \right) &+ h_{eff,w} a_{w,int} \left(T_w - T_f \right) \end{aligned} \tag{2.25}$$

$$w_{v,w} \rho_w C_{p_w} \frac{\partial T_w}{\partial t} = w_{v,w} \frac{\partial}{\partial z} \left(k_w \frac{\partial T_w}{\partial z} \right) + h_{eff,w} a_{w,int} \left(T_f - T_w \right) + h_{w,ext} a_{w,ext} \left(T_{ext} - T_w \right) \tag{2.26}$$

$$\frac{\partial \rho_f}{\partial t} + \frac{\partial \left(\rho_f \cdot u_f \right)}{\partial z} = 0 \tag{2.27}$$

where the equations 2.24 to 2.26 represent the energy balances at the storage tank, and the subscripts r and s denote the large and small particles, respectively. The formulation considers the volume fraction of the small particles per unit of bed volume $w_{v,s}$, and a volume fraction for the wall volume $w_{v,w}$. Besides, the continuity equation (Equation 2.27) determines the velocity field of the fluid across the storage.

Finally, Table 2.8 presents a comparison of the studied models. In general, two-phase models are applied to study the global thermal behavior of a packed bed separating the fluid from the solid phase, without considering thermal losses or wall effects. These models can include conduction heat transfer if the Reynolds number is low ($Re < 25$) and intraparticle thermal gradient if the Biot number is high ($Bi > 0.1$). However, it is necessary to mention that integrating thermal losses or thermal diffusion over the Reynolds limits allow for a more robust modeling because more relevant factors are included. On the other hand, the single-phase formulation is applied to study packed beds when the solid and fluid phases can be assumed to be close to thermal equilibrium; this is the case for small particles (such as sand) or when the volumetric thermal capacity of the fluid is small compared to the volumetric thermal capacity of the solid (Ratio > 29) [36, 87]. These models have a lower computing

Table 2.8: Main characteristics of each heat transfer model described.

Model	Phases	Dim.		Diffusion	Advection	Heat loss/ Wall effect	Multi-size	Intra-part. grad.	Suitable for	Ref.	Special cases	Exp. studies	HTF	Sol. method	Radiation
		1D	2D												
Single	1	✓	✓	✓	✓	✗	✗	✗	$\frac{(\rho c_p)_f}{(\rho c_p)_s} \ll 1$	[87]	Wall eff.: [36],[144], [145],[146]	[145],[147], [148],[40], [146],[44]	Air: [87], [36],[38], [145],[40], [146] sCO$_2$:[144], [148] Oil:[149], [147],[44]	IFVM^a: [36], [144] EFDM^b: [149], [146] IFDM^c: [147] FEM^d: [40]	-
Schumann	2	✓	✗	✗	✓	✗	✗	✗	$Re \geq 25$	[135],[118], [150],[151], [152],[138]	-	-	Air: [150], [138] Oil:[150], [151] Molten salt: [150]	AM^e: [135]	-
C-S	2	✓	✓	✓	✓	✗	✗	✗	$Re \leq 25$	[137],[118], [87]	Wall eff.: [16],[50], [38],[151], [153]	[34],[65], [66],[154], [155],[45], [156],[157], [158]	Air: [34], [16],[38] ,[156],[157], [158] Oil: [151], [154],[65], [66],[155] Molten salts: [153]	IFVM: [153] EFDM: [154]	-
D-C	2	✓	✗	✓	✓	✗	✗	✓	$Bi > 0.1$	[138],[139], [38],[159]	-	[138],[115]	Air: [138], [139],[38]	IFVM: [159] IFDM: [138] AM: [139]	-
Wall grad.	3	✓	✓	✓	✓	✓	✗	✗	Experimental, pilot scale packed bed.	[141],[142], [160],[161]	-	[142],[162], [141],[37]	Air: [141], [37], [160], [161] Fuel gas: [162] Oil: [142]	IFVM: [160] IFDM: [142], [141],[37] FEM: [162], [161]	[162],[141], [37],[160], [161]
Bi-dispersed	3	✓	✗	✗	✓	✗	✓	✗	Arrangements of different particle sizes.	[143]	-	-	Air: [143]	-	
Mixed	3	✓	✗	✓	✓	✓	✓	✓	Generalized for any Bi.	[24]	-	-	Air: [24] Flue gas: [24] Oil: [24]	AM: [24]	[24]

[a] Implicit Finite Volumes Method,
[b] Explicit Finite Differences Method,
[c] Implicit Finite Differences Method,
[d] Finite Element Method,
[e] Analytic Method

time compared to the two-phase models because of the lower number of equations to solve. The thermal losses and the wall effects can be modeled precisely by adding an equation for the storage walls to the two-phase formulation. However, the influence of these variables is important to small packed beds, or in zones close to the walls of the packed bed, as pointed out by Beasley and Clark [141]. This influence can be neglected in the center of packed beds for regular-size storage. Besides, the three-phase formulation can be extended for systems with multiple-size particles, allowing modeling heterogeneities within the packed-bed. Finally, there is a basic formulation for each model that is contrasted in Table 2.8, and adding more complexity and detail to the model is part of the assumptions made by the analyst to develop the study. Thus, considering more dimensions in the model enable capturing more phenomena involved in the heat transfer process, but with the disadvantage of having a higher computational cost, which also occurs by including more equations to the model.

2.5 Experimental studies

For high-temperature thermal storage in packed beds using air as a HTF, Meier et al. [34] developed a computer code that solves a one-phase 1D heat transfer equation, called PACKBEDA. The code allows the evolution of the temperature profiles across the packed-bed, assuming temperature-dependent properties and heat losses through the walls. The code was validated by comparing experimental data from a test bench specially built for that purpose. The test bench considered a cylindrical vessel, which presented high heat losses through the walls due to its geometry. Nevertheless, this behavior was efficiently reproduced by the heat transfer model. Hänchen et al. [16] also used the empirical results from Meier et al. [34] to validate a 1-D heat transfer model based on the *C-S* formulation, and coupling a heat loss term in the equation for the fluid phase. A parametric analysis was carried out to evaluate the charging/discharging process and the cyclic operation in terms of the thermal efficiency and capacity ratio, varying the dimensions of the packed-bed, mass flow rate, particle diameter, and the material employed as storage media.

Another experimental study was developed by Zanganeh et al. [25], consisting of a 6.5 MWh thermal storage unit, with a truncated conical shape. The experimental facility was used to validate a two-phase heat transfer model for the packed-bed, using air as the HTF. Different comparisons were carried out considering the geometry of the storage (cylindrical or conical) and the temperature dependence of thermophysical properties.

Figure 2.15 shows the temperature and energy profiles across the tank for different shapes. A higher amount of energy is stored at the tank's upper side due to its larger diameter at the top of the conical storage [25]. Nonetheless, the thermal losses related to the cover area are larger in the conical tank. Thus, the temperature of the air is lower than that observed for the cylindrical tank.

Zanganeh et al. [25] also compared the influence on the temperature profiles of considering temperature-dependent properties for the fluid and the solid phases against considering constant properties evaluated at an average temperature. In Figure 2.16, 20 h of the charging process was evaluated for a conical tank shape, highlighting the underpredicted temperature values for the hot region and over predicted values in the cold region for the fluid phase. This

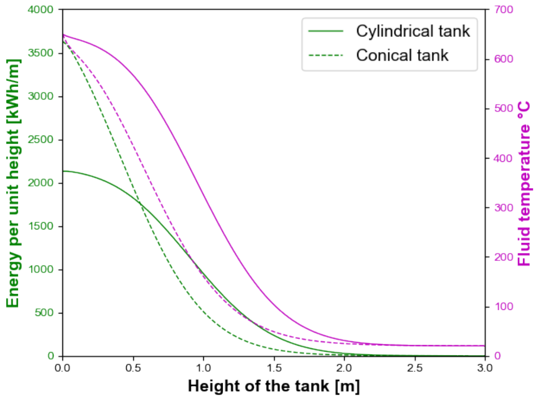

Figure 2.15: Temperature and energy distribution after 8 hours of charging. Modified from Zanganeh et al. [25].

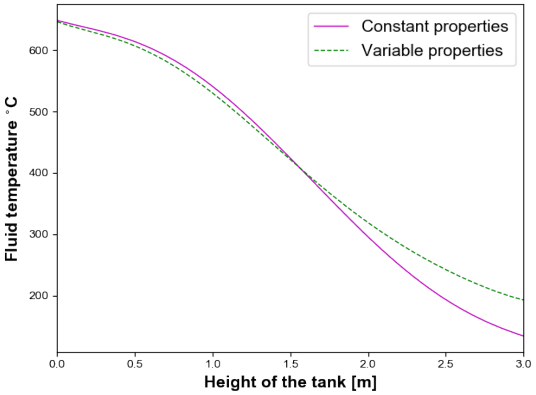

Figure 2.16: Temperature profiles after 20 hours charge for constant and variable solid and fluid properties. Modified from Zanganeh et al. [25].

effect is explained by the consideration of constant properties for the solid phase.

Anderson et al. [145] developed a one-phase thermal model for a packed-bed using α-alumina particles as the solid phase and air as HTF. Temperature-dependent thermophysical properties were used in the model, which was validated against experimental data. The study was developed for two cases of maximum temperatures: 120 °C and 700 °C, where a direct comparison was carried out considering models using constant and variable properties. In both cases, there were significant differences, which are even more critical when the system is at a high temperature, close to 700 °C.

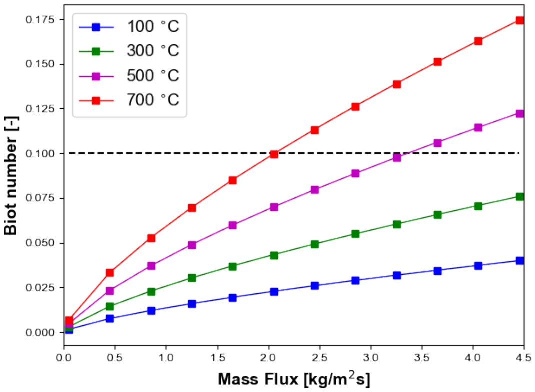

Figure 2.17: Biot number as a function of mass flux and different temperatures. Modified from Anderson et al. [36].

For the model considering variable thermophysical properties within the phases, the Biot number was assessed to analyze the temperature limits at which the intraparticle gradients can be neglected for the geometry proposed in the article (see Figure 2.17). Thus, at higher temperatures and mass flow rates, neglecting intraparticle gradients is no longer a valid assumption [36].

For the 1D three-phase formulations, the bi-dispersed model introduced by Odenthal et al. [143] focuses on accurate modeling of the multisized packed-bed arrangements. The study compares the results obtained by the novel formulation with those obtained by the Schumann's model [135], which considers different combinations of average size particles and void fractions. A simulation assessment of the model considered both single blow and cyclic operation for heat storage using molten salts as the HTF.

Figure 2.18a presents that deviations are up to 6 K for a single blow operation scenario when the sizes of the particles are different. The differences observed for the cyclic operation were even higher for the heterogeneous distribution scenario (Figure 2.18b). In other cases, the differences cannot be neglected. Thus, the author suggested the use of a bidisperse model for packed beds with at least two different particle sizes and dense fluids such as molten salts or thermal oil [143].

Hoffmann et al. [142], studied the temperature distribution of three scales of storage tanks: a small tank (8.3 kWh), a medium-size tank (2.3 MWh), and an industrial-scale tank (170 MWh). The study compared the accuracy of the predictions delivered by the 1D single-phase and 1D two-phase formulations. The comparison was conductes using experimental

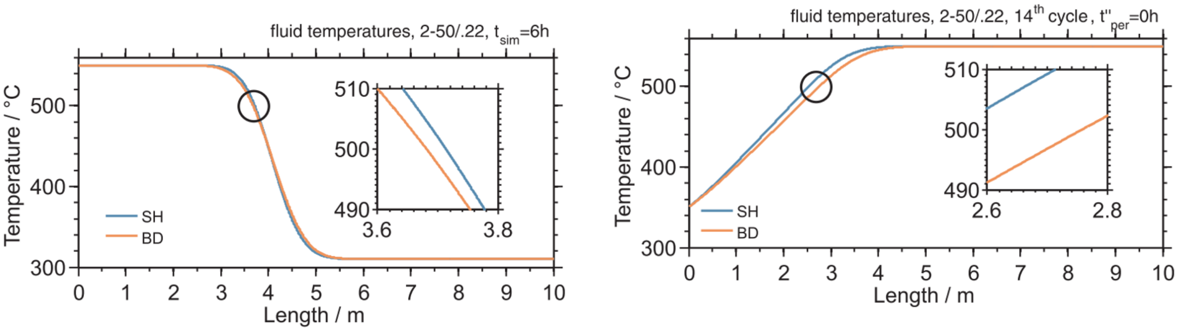

(a) Temperature profiles for single blow.

(b) Temperature profiles at the beginning of the last discharge process after 14 cycles.

Figure 2.18: Bidispersed model comparisons by Odenthal et al. [143].

data from the different storage tanks described above. Both models considered thermal losses, although for the two-phase model, a new equation was coupled with the storage walls' effect. The experimental validation confirmed that for small-scale tanks, a two-phase formulation is more accurate. In contrast, for industrial-scale tanks, the single-phase approach exhibited a close agreement with the experimental measurements. In addition, the effects of considering thermal losses and the wall temperature distribution were essential for capturing the thermal behavior of small tanks. It is demonstrated in an experimental set-up considering a storage tank of 8.3 kWh.

Previously presented 2D models were formulated as an extension of the 1-D approach, aiming to establish an accurate method to analyze the thermal behavior of a packed-bed TES. Some authors developed suitable experimental settings to validate the proposed models. For instance, Beasley and Clark [141] validated a two-dimensional three-phase formulation for packed beds using thermocouple measurements in the radial and axial directions of the flow. The model showed an outstanding consistency with the experimental data for a wide range of conditions regarding Reynolds numbers. Furthermore, with the experimental data in the radial coordinate, the effects of the void fraction on the fluid flow were assessed.

Another relevant element in determining the radial temperature gradients of the phases is the effect of the storage walls. In this regard, a numerical study was carried out by Aly and El-Sharkawy [45], where a 2D model was employed to predict the temperature profiles of a packed-bed with different wall temperatures imposed. The study results proved that along the bed centerline, the wall temperature did not affect the air or solid temperature profiles. However, for the solids near the storage wall, the temperature showed a strong influence on the storage outlet temperatures. Moreover, the radial variation distribution could be explained by the increase in the thermal boundary layer's thickness during the charging operation. It reached approximately 60% of the bed cross-sectional area during 6 h of operation.

Regarding the analysis of high-temperature air storage in porous media, Rodrigues and de Lemos [163] developed and validated a 2D CFD model to investigate the transient behavior of temperature fields and the thermocline thicknesses of TES systems as a function of the ratio between the thermal conductivity and the thermal capacity of the fluid and solid. The model demonstrated its suitability by determining the thickness of the thermocline in the transient regime and different turbulent flows. In addition, the model was able to assess the transient stratification and storage efficiency for different conductivity ratio (k_s/k_f) and thermal capacity ratios ($\rho_s C_{cs}/\rho_f C_{cf}$).

An entropy generation approach for the stratification process due to heat losses, in standby mode, was implemented by Bai et al. [164] using a 2D CFD model to capture the cooling process in a TES tank. In addition, different aspect ratios were evaluated. The two-dimensional model was validated against experimental data of the temperature profiles measured through the axial dimension of the tank. The simulations were compared against experimental data, obtaining an acceptable fit. The authors hold that for the simulations, the velocity fields were small; thus, the mass transport process can be simplified into a heat transfer model. Through a one-dimensional model, the thermal stratification was assessed and validated against experimental measurements. A tank with an aspect ratio of 1 showed the highest energy and exergy efficiencies, as well as the lowest entropy generation during the cooling process. Further analyses showed that considering aspect ratios larger than 3 had small influences on the energy and exergy efficiencies.

2.6 Radiation exchange

Thermal radiation has significant relevance during the operation of granular packed beds at high temperatures. The overall heat transfer process between the storage elements (particles and walls) is profoundly affected by the radiation exchange at temperatures higher than 900 °C, and therefore cannot be neglected [86]. The process of heat exchange by radiation has been mainly treated in granular packed beds by developing effective thermal conduction coefficients for the radiation exchange ($k^{0\,rad}_{eff}$) using experimentally determined correlations. In recent years, some authors have proposed the development of heat transfer models in granular packed beds by explicitly incorporating heat exchange by radiation [165, 166, 167]. A detailed analysis of the heat exchange by radiation in each element was performed inside a granular packed-bed (with high particle density) in such studies. This approach has shown an unacceptable computational cost for practical applications, as it has to evaluate the view factors between all the elements of the storage. Therefore, different spatial models for modeling the interaction via thermal radiation between the confined particles have been defined in the literature. Wu et al. [168] developed a study analyzing the effect of three radiation models with different spatial ranges: short-range model, long-range model, and particle scale model.

Short-range models: These models consider that particles only exchange heat by radiation with their neighboring particles. Depending on the domain discretization method, it means direct particle contact or with particles in adjacent cells. This model usually underestimates the heat exchange by radiation because the sum of the view factors for a particle is usually much lower than the unity, reaching values of 0.834 for discretization in Voronoi cells [168]. This model usually allows achieving acceptable results for temperatures lower than 1250 °C and when the thermal conductivity of the solid is similar to the effective thermal conductivity including radiation ($k_s \sim k^{0\,rad}_{eff}$). This is because this approach usually overestimates the heat transfer by conduction, causing both errors to be canceled out and to agree with the experimental results.

Long-range models: These models consider that particles exchange heat by radiation with particles within a radius of interaction (R_{int}), with respect to a reference defined center in a function of the density of particles in the storage. The following tolerance range (τ) is defined for selecting the radius of interaction:

$$\left| \sum_{\text{i}=1}^{n} F_{\text{i}j} - 1 \right| > \tau \longrightarrow R_{\text{int}} = R_{\text{int}} + \nabla\delta \tag{2.28}$$

$$\left| \sum_{\text{i}=1}^{n} F_{\text{i}j} - 1 \right| < \tau \longrightarrow R_{\text{int}} = R_{\text{int}} \tag{2.29}$$

where $F_{\text{i}j}$ corresponds to the view factor between the particle i and particle j, $\nabla\delta$ corresponds to the correction factor for R_{int}, when it does not meet the tolerance set for the sum of the view factors. The model requires the development of an algorithm to estimate the obstructed view factors between the particles in the packed-bed and a locator algorithm used by the discrete element method. Wu et al. [168] pointed out that this model is suitable for estimating the heat transfer by radiation when the thermal conductivity of the solid is much higher than the effective thermal conductivity including radiation ($k_s \gg k_{\text{e}ff}^{0\,rad}$) and for temperatures up to 1500 °C.

Particle scale model: Wu et al. [168] proposed developing a microscopic model when the assumption of constant surface temperature on the particle cannot be ensured. This situation occurs when the dimensionless thermal conductivity of the solid is lower than 10 ($\Lambda < 10$). For this purpose, the surface of each sphere is discretized into meshes of uniform temperature. Thereafter, the radiation heat exchange is calculated with the neighboring particles. This model shows good results for estimating the effective thermal conductivity ($k_{\text{e}ff}$), used for assessing the process of heat transfer inside a packed-bed due to diffusion phenomena. However, the computational resources required for its application make this approach impractical.

To evaluate the accuracy of these models, Wu et al. [168] determined the coefficient of effective thermal conductivity ($k_{\text{e}ff}$) and the coefficient of effective thermal conductivity for radiation ($k_{eff}^{0\,rad}$) for each of the models presented. The authors compared the models against correlations for the same parameters proposed in the literature [91, 169, 170], obtaining good agreement under the conditions previously indicated for each model.

2.6.1 View factors

Determining and effectively evaluating view factors in packed-beds is complex because of the random configuration that particles acquire inside the tank. One of the first studies devoted to determining the view factors in packed-bed systems was carried out by Wakao et al. [171], proposing an algorithm for calculating the view factors between hemispheres (of equal or different radius) in contact. In a similar approach Juul [172] and Felske [173] deduced analytical expressions to approximate the view factor between two near spheres.

Several years later, Tanaka [174] proposed an analogous solution for the case of two spheres of equal size with no obstacles between them.

Han et al. [175] proposed a two-dimensional space algorithm based on Hottel's cross-string theorem [176], which allows determining the view factor between circles of different sizes and randomly ordered in a plane. This algorithm includes a methodology for calculating the view factor between both circles obstructed by others. This approach has the disadvantage that considering two-dimensional bodies may not represent the view factor between spheres. Indeed, 3D objects do not comply with the assumption made by Hottel. Moreover, it should be noted that this algorithm requires an additional search algorithm to determine the positions of the particles.

Following a more traditional approach, Feng and Han [177] proposed an algorithm based on a deterministic ray-tracing methodology to estimate the view factor between spheres of equal size and with obstacles between them. In this study, the integral for calculating the view factor between the spheres is discretized using three tools: the (1) Tanaka [174] integral to determine the intersphere form factor, (2) the standard Fibonacci numeric integration scheme [178] and (3) a nonuniform scaling variable (as a variable change for the z coordinate). It is important to note that the algorithm requires the implementation of a search algorithm, such as that proposed by Han et al. [175]. Moreover, using Han et al.'s [175] or Feng and Han's [177] algorithms in packed beds with large numbers of particles require defining the radius of interaction between particles to determine the view factor between them. The effectiveness of the radius of interaction is evaluated by defining the tolerance level. This algorithm was validated for the case of spheres with no obstacle in between, compared to the analytical expression of Tanaka [174].

Wu et al. [168] proposed a practical method to estimate the view factor between neighbored spheres employing Voronoi cells and deduced an analytical expression. In recent time, these authors also proposed a novel method employing a multi-layer neuronal network to compute the view factor matrix for random distribution particle packed bed [179].

Considering that the application of the analytical solutions described above is limited, several authors have evaluated the heat exchange by radiation using a stochastic approach, such as the Monte Carlo-based ray-tracing methods [180, 181, 182, 183].

2.6.2 Relevance of radiation heat transfer on packed-bed modeling

Because of the high temperature achieved in packed-bed storage applications, radiation heat transfer can play a significant role in developing the temperature profile across the tank during the operating cycle. Neglecting the contribution of radiation exchange may not be recommended under certain conditions. As pointed out in the previous sections, several authors have included the effect of radiation through correlations of the effective thermal conductivity [25, 82]. This approach takes into consideration the temperature of the particle but does not model the radiation exchange with the neighboring elements.

This section describes a simple study to assess the influence of radiation heat exchange in the operation of packed-bed storage during the charging process and standby periods. It assesses the heat transfer phenomena by considering the radiation exchange by including an explicit term based on the interaction between the surrounding particles. Through a parametric analysis, thermal radiation is compared to the energy transferred by forced convection.

Simplified model

The domain of the discrete model corresponds to a vertical column of identical spheres, which are located in the centerline of a packed-bed storage, surrounded by the HTF. A subdivision of the column is made by cubic cells that enclose a single sphere and the fluid around it (Figure 2.19); thus, the porosity of the structure can be calculated as: $\phi = \left(V_{cell} - V_{sphere}\right)/V_{cell}$, where $V_{cell} = \mathrm{d}^3$ is the volume of the cell that contains the sphere with diameter d and volume V_{sphere}.

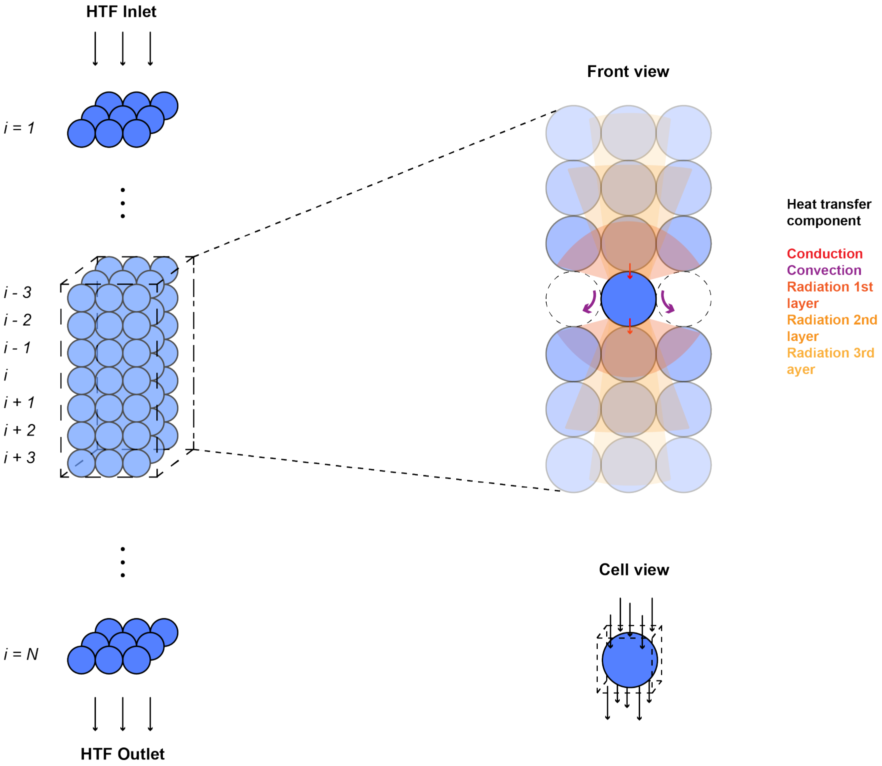

Figure 2.19: Scheme of the heat transfer phenomena involved within the arrangement.

The proposed model is based on the assumptions of Schumann's formulation with the addition of unidirectional heat transfer between particles, diffusion into the surrounding fluid, and radiation between neighbors. In the following paragraphs, the heat transfer mechanisms considered herein are briefly explained.

Conduction, $\dot{Q}_{cond}$ For each phase, the Fourier's Law [184] is employed considering an effective area of conduction, expressed by Equation 2.30. During the charging process, the thermal conductivity is modeled as motionless stagnant conductivity for the solid phase and as the axial effective thermal conductivity for the fluid (Table 2.4).

$$A_{eff} = \begin{cases} \phi \cdot \mathrm{d}^2 & \text{for fluid phase} \\ (1-\phi) \cdot \mathrm{d}^2 & \text{for solid phase} \end{cases} \tag{2.30}$$

Convection, $\dot{Q}_{conv}$ The convective heat transfer coefficient, h, depends on whether forced or natural convection occurs. During forced convection, the volumetric heat transfer coefficient h_v is determined using the expression proposed by Coutier and Farber [42], considering the relationship between h_v and the convective heat transfer coefficient, $h = h_v \cdot (V_{cell}/A_{sphere})$. For natural convection, two scenarios are considered: if the temperature of the solid is higher than the fluid, h is estimated using the correlation proposed by Nellis and Klein [184]; on the contrary, h is estimated using $Nu = 2$.

Radiation, $\dot{Q}_{rad}$ Two approaches were considered to include thermal radiation. First, an implicit formulation, where the radiation phenomenon is included in the effective thermal conductivity using the correlation of Zehner and Schlünder [91]. Additionally, an explicit approach was considered, where the radiation effect was considered by assuming the spheres as gray surfaces [184], and assessing the radiation exchange between spheres that are located up to three times their diameter apart, as observed in Figure 2.19. The analyzed sphere manages to "see" the superior and inferior planes composed by neighboring spheres, which are approximated to the squares of side 3·d, and the view factors for the present arrangement are calculated as suggested in [177].

Charging and Standby process

A time-dependent energy balance was carried out for the fluid and the i-th solid sphere enclosed by the cubic domain. The thermophysical properties for each phase are assumed to be constant and the analysis was developed for air and the waste material *EAF Slag 1*, whose properties are presented in Table 2.1. For the charging process, the following equations represent the energy balances for each phase:

$$\rho_s V_{cell}(1-\phi)C_{p,s}\frac{\mathrm{d}T_{s,\mathrm{i}}}{\mathrm{d}t} = \dot{Q}_{cond,s,\mathrm{i}-1} - \dot{Q}_{cond,s,\mathrm{i}+1} + \dot{Q}_{conv,\mathrm{i}} + \sum_{n=1}^{3}\left(\dot{Q}_{rad,\mathrm{i}-n,\mathrm{i}} - \dot{Q}_{rad,\mathrm{i}+n,\mathrm{i}}\right) \quad (2.31)$$

$$\rho_f V_{cell}\phi C_{p,f}\frac{\mathrm{d}T_{f,\mathrm{i}}}{\mathrm{d}t} = \dot{Q}_{cond,f,\mathrm{i}-1} - \dot{Q}_{cond,f,\mathrm{i}+1} - \dot{Q}_{conv,\mathrm{i}} + \rho_f A_{sup}\phi u\frac{C_{p,f}}{2}\left(T_{f,\mathrm{i}-1} - T_{f,\mathrm{i}+1}\right) \quad (2.32)$$

where the subscripts s and f relate to the solid and the fluid phase, respectively. The term A_{sup} in Equation 2.32 represents the upper area of the cubic cell where the fluid enters the domain. For the implicit model, the radiative terms are not considered, and the effective thermal conductivity for the solid phase is recalculated using the correlation proposed by [91]. The initial conditions for the charging process consider that the temperature of the phases is equivalent to the surroundings (25 °C). In the first cell, the fluid enters the domain with an inlet temperature, as presented in Table 2.9. The formulation of the standby process is analogous to the charging process, but neglecting the energy transportation term, and the initial conditions are the temperature profile obtained at the end of the charging process for each phase.

The energy balance results are depicted in Figure 2.20 for both charge and standby processes. As observed in the figure, there is a significant discrepancy between the temperature

Table 2.9: Operating conditions of the proposed model.

Parameter	Value
Re	60
d [mm]	25
Inlet temperature °C	1100
Number of spheres in the column	100
Emissivity	0.8
Charging time [h]	4
Standby time [h]	2

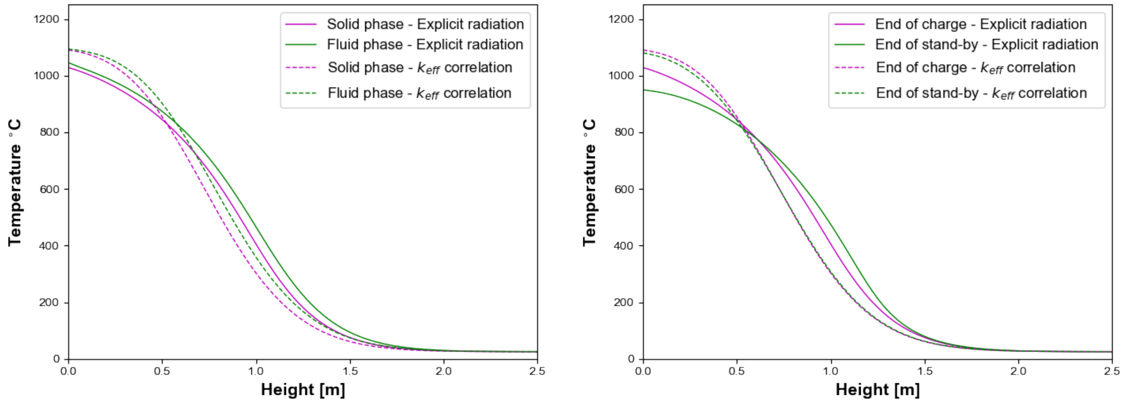

(a) Charging process.

(b) Standby process.

Figure 2.20: Temperature profile comparisons between implicit and explicit radiation.

profiles when considering radiation explicitly and applying the correlation of Zehner and Schlünder [91]. The model that considers explicitly the radiation incorporates the interaction between seven particles during the heat transfer, whereas in the implicit formulation, the radiation is considered in the conduction term, involving three particles in the heat exchange process. The above consideration explains that, using the explicit model, the upper zone of the arrangement exhibits lower temperatures, while at the center of the arrangement, the temperatures are higher. This effect is due to radiation being transmitted quickly from the particles with higher temperature to the particles located in the center of the storage. In the lower zone of the arrangement, the slopes of the curves through both approaches are similar, which is due to the weaker influence of radiation heat transfer at low temperatures. In addition, during the standby process, the radiation effect can be evidenced through an alteration in the thermocline generated, suggesting that the phenomenon described could have a negative impact on the performance of storage systems.

By calculating an equivalent effective conductivity for the exposed radiative model, using Equation 2.33 for radiation coming from above and the Equation 2.34 for the radiation that goes to the particles below, a comparison can be made against other correlations proposed in the literature. For instance, the correlations formulated by Kunii and J.M. [170] and Schotte [169].

$$k_{rad,up,\mathrm{i}} = \frac{\mathrm{d} \cdot \sum\limits_{n=1}^{3} \dot{Q}_{rad,\mathrm{i}-n,\mathrm{i}}}{A_{\mathrm{e}ff,s} \cdot \left(\frac{\sum\limits_{n=1}^{3} T_{s,\mathrm{i}-n}}{3} - T_{s,\mathrm{i}} \right)} \tag{2.33}$$

$$k_{rad,low,\mathrm{i}} = \frac{\mathrm{d} \cdot \sum\limits_{n=1}^{3} \dot{Q}_{rad,\mathrm{i}+n,\mathrm{i}}}{A_{\mathrm{e}ff,s} \cdot \left(T_{s,\mathrm{i}} - \frac{\sum\limits_{n=1}^{3} T_{s,\mathrm{i}+n}}{3} \right)} \tag{2.34}$$

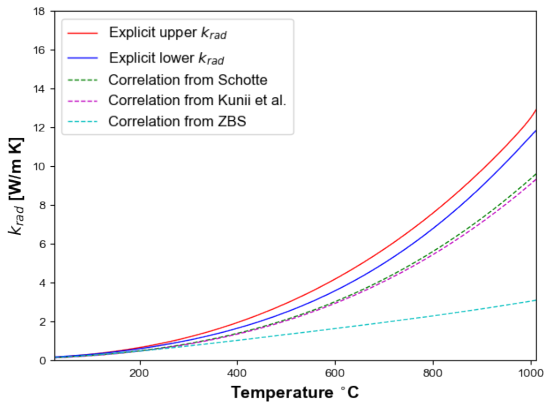

Figure 2.21: Effective thermal conductivity comparisons.

From Figure 2.21, a temperature limit can be set for which the formulations are equivalent, which is around 300 °C. Above that temperature level, there are significant discrepancies between the models.

The effects of the radiation heat transfer within a packed-bed can also be modeled by calculating the overall radiation heat transfer coefficient, which must consider the exchange of both the upper and lower planes. Thus, the formulation depends on whether the solid is gaining or losing energy due to radiation. Considering that parameter, the explicit radiation can be compared against forced convection during the charging period. In this context, the values of h are calculated with the temperature-dependent properties of air.

$$h_{rad} = \begin{cases} \dfrac{\left(\sum\limits_{n=1}^{3} \dot{Q}_{rad,\mathrm{i}-n,\mathrm{i}} - \sum\limits_{n=1}^{3} \dot{Q}_{rad,\mathrm{i}+n,\mathrm{i}}\right)}{A_{sphere} \cdot \left(\dfrac{\sum\limits_{n=1}^{3} T_{s,\mathrm{i}-n}}{3} - T_{s,\mathrm{i}}\right)} & \text{if} \quad \sum\limits_{n=1}^{3} \dot{Q}_{rad,\mathrm{i}-n,\mathrm{i}} - \sum\limits_{n=1}^{3} \dot{Q}_{rad,\mathrm{i}+n,\mathrm{i}} > 0 \\ \dfrac{\left(\sum\limits_{n=1}^{3} \dot{Q}_{rad,\mathrm{i}-n,\mathrm{i}} - \sum\limits_{n=1}^{3} \dot{Q}_{rad,\mathrm{i}+n,\mathrm{i}}\right)}{A_{sphere} \cdot \left(\dfrac{\sum\limits_{n=1}^{3} T_{s,\mathrm{i}+n}}{3} - T_{s,\mathrm{i}}\right)} & \text{if} \quad \sum\limits_{n=1}^{3} \dot{Q}_{rad,\mathrm{i}-n,\mathrm{i}} - \sum\limits_{n=1}^{3} \dot{Q}_{rad,\mathrm{i}+n,\mathrm{i}} < 0 \end{cases} \tag{2.35}$$

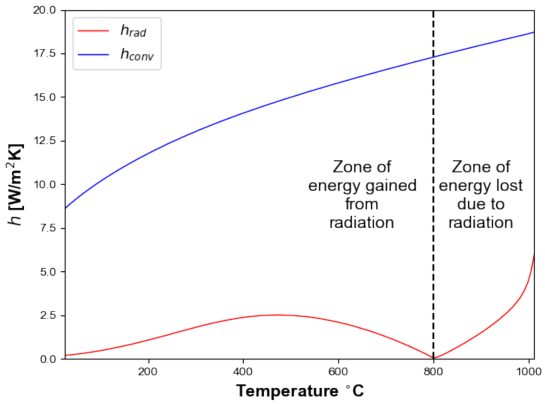

Figure 2.22: Comparison of convection and radiation coefficients for nominal conditions.

As observed in Figure 2.22, two zones are identified: one where the particles decrease their internal energy due to radiation heat transfer, and a second zone where the particles increase their internal energy due to the radiation coming from the upper levels. Furthermore, comparing the maximum values of h_{rad} in the decreasing and increasing zones against the h_{conv} evaluated at the respective temperatures, the radiation coefficients can reach values that represent 32% and 17% of the convective heat transfer coefficient, respectively.

Parametric analysis

The proposed model is used to perform a parametric analysis to assess the operating conditions' influence on the radiation heat transfer observed in packed-bed storage. The coefficient h_{rad} expressed in Equation 2.35 is compared to the forced convection heat transfer coefficient. The effect of two variables was analyzed: the Reynolds number and the particle diameter. The effects of such variables are assessed in the complete arrangement at the end of the charging process. In Table 2.10, the conditions defined for the parametric analysis are listed, and the results are presented in Figure 2.23.

Varying the Reynolds number results in different temperature profiles within the arrangement; thus, the radiation heat transfer exhibits a different behavior for each regime. On the other hand, at higher values of Re, the particles reach higher temperatures, and the curves of h_{rad} in Figure 2.23 allow to distinguish the two areas described above. On the other hand, the convective heat transfer coefficient increases its value, and when compared to radiation at

Table 2.10: Operating conditions of the parametric analysis.

Parameter	Value	Number of cases
Re	15 – 150	10
d [mm]	25 – 45	2
Inlet temperature °C	1100	-
Charging time [h]	4	-

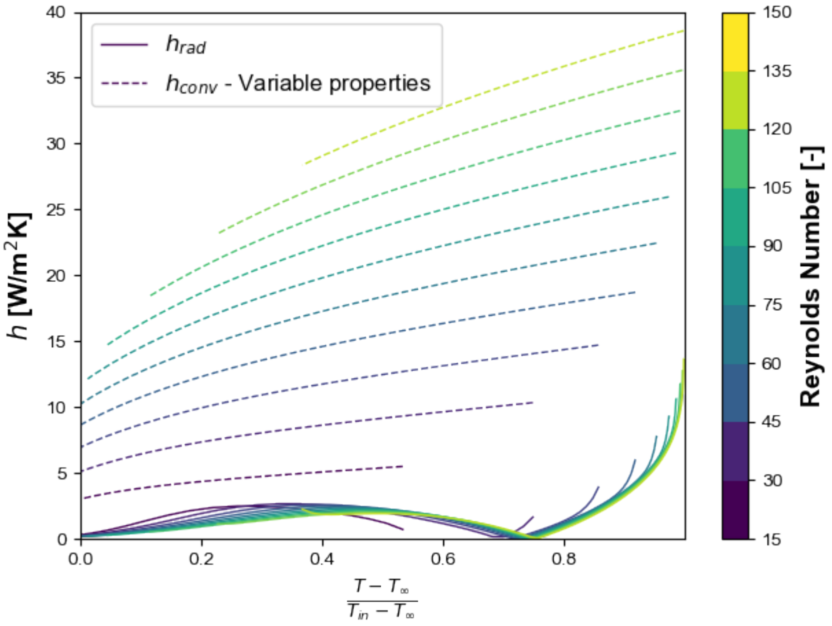

(a) Study with d = 25 [mm].

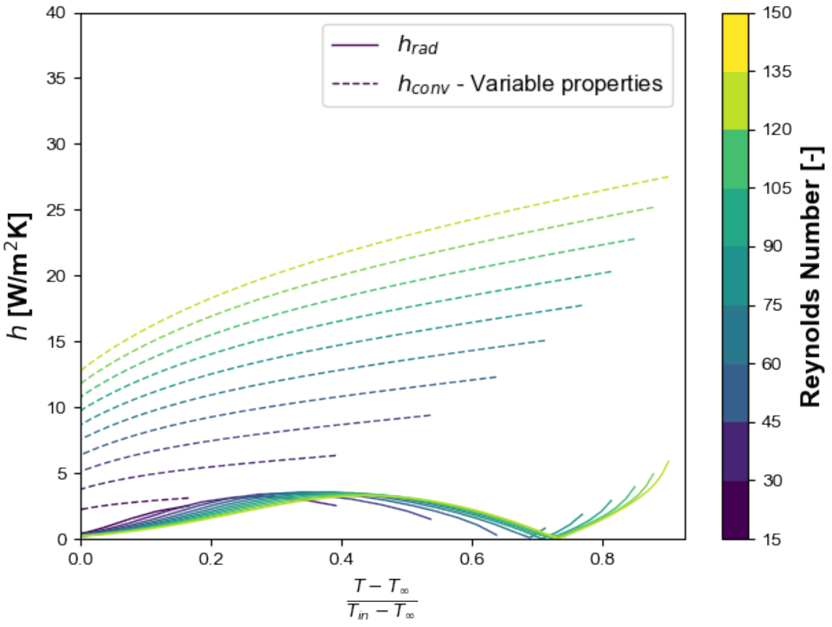

(b) Study with d = 45 [mm].

Figure 2.23: Convection and Radiation coefficients for different Reynolds numbers.

high temperatures, a predominance of the h_{conv} can be established. However, this effect does not indicate that radiation can be neglected, since, in the upper regions of the storage (inlet zone of the charging process), the temperature of the fluid and the temperature of the solid can be close, making the convection heat transfer lower due to thermal equilibrium, which is a mechanism of contact interaction. Radiation in these regions may be relevant because radiation allows distance interaction between particles in the upper regions and particles in the middle regions of the storage, which have a higher temperature difference in comparison with near particles. Regarding the influence of the particle diameter on the radiation coefficient, higher values are reached in the middle of the arrangement, but conversely, the convection heat transfer seems to have no significant variations.

2.7 Conclusions

This paper presents a comprehensive review of the different approaches described in the literature for modeling and assessing the performance of packed-bed storage systems. One of the main differences observed within the models is considering the radiation exchange within the particles in the tank. A simple study was carried out, allowing the identification of its influence as a function of the particle temperature. The main findings are summarized as follows:

- The heat transfer coefficients proposed in the literature show significant differences between each other; hence, a generalization only based on characteristics terms as porosity and dimensionless number may be ventured. The limitations for applying such heat transfer coefficients are given by the fact that they were defined for a specific configuration that does not apply to a broad range of conditions. The empirical heat transfer coefficients are considered an adequate tool for assessing the magnitude of the heat transfer phenomena involved in a packed-bed.
- Regarding the size of the storage tanks, several aspects of the modeling must be considered, and therefore advanced modeling techniques would allow highly accurate simulations. However, it can be computationally expensive. Simplified formulations adequately approximate the phenomena observed in pilot-scale tanks, allowing to assess the system's performance with acceptable accuracy.
- Assessing the thermal interaction between the particles in the packed-bed, the fluid, and the wall is highly relevant to conduct an accurate evaluation. There are simple approaches that use correlations or by assessing the heat transfer coefficients by analyzing the features of the wall, which becomes significant for small storage tanks.
- The magnitude of the errors reported in the literature is highly related to the assumptions and simplifications made during the formulation. One of the approximations most employed assumes constant properties for both the HTF and the solid phase, which introduces errors in a range between 1 and 5%, but significantly reduces the computational time compared to the variable properties approach.
- The effect of the heat transfer by radiation in packed beds is commonly neglected. Studies that have considered it explicitly reduce the assessment to one heat transfer mechanism. The correlations reported in the literature for the effective thermal conductivity due to thermal radiation only consider the temperature of the particles, and do not include the temperature gradient around it. This issue was evidenced in the

simple analysis, showing significant discrepancies with respect to the correlations for assessing the temperature profiles at high operating temperatures. In this context, the heat transfer coefficient for radiation could be as high as 32% of the convection coefficient, and thus should not be neglected at temperatures higher than 750 °C and should be treated as a long-distance interaction mechanism.

The proper selection of the modeling approach is crucial for building cost-effective storage systems that can enable the introduction of renewable energy sources in the electricity-generating matrix, or for facilitating the integration of renewable heat into industrial processes.

Chapter 3

Assessing the use of copper slags as thermal energy storage material for packed-bed systems

Thermocline tanks using packed-bed of rocks have become feasible candidates for improving the performance of Concentrated Solar Power plants, enabling high operating temperatures and reduced capital costs when industrial byproducts are employed as filler materials and low-cost working fluids, being competitive against molten salts thermal storage systems. The present work assesses the potential of using copper slags in packed-bed systems as filler material. Through a thermal characterization, it is demonstrated that copper slags show similar properties to other slags proposed in the literature for thermal storage medium and better thermal capacity (1.4 - 1.5 J/(g K)). A heat transfer model was developed to predict the cyclic behavior of a packed-bed storage using copper slags and employed in a parametric analysis to assess the impact of storage dimensions on 1^{st} and 2^{nd} law efficiencies for different storage materials, allowing to identify several design considerations depending on tank's volume. The main findings indicate that the high thermal capacity of copper slags favors the development of a steeper thermocline, keeping a low rate of exergy loss at storage's outlet, and also higher energy density stored of $138\,\mathrm{kW\,h/m^3}$ against $129\,\mathrm{kW\,h/m^3}$ of other byproducts under similar storage dimensions.

3.1 Introduction

The current trends in energy supply and use are highly unsustainable socially, economically, and environmentally. The need for a substantial change on the development path has encouraged the scientific community to study environmentally friendly energy systems as a measure to achieve a substantial reduction of greenhouse gas emissions. In that context, one of the main difficulties for increasing the share of renewable energy in the energy matrix is the availability of reliable and affordable energy storage solutions. Energy storage technologies can contribute to a better integration of electricity and heat network systems, playing a crucial role in improving energy systems' efficiency and enabling the introduction of large share sustainable sources [9]. For instance, Concentrated Solar Power (CSP) plants are equipped with thermal energy storage (TES) systems, which provide heat in a dispatchable way to a power block, and give operational flexibility even during periods of low solar radiation.

CSP plants commonly use molten salt mixtures as heat transfer fluid (HTF), which is also employed as sensible heat material for thermal storage due to its high thermal capacity. The most common mixture of salts in CSP plants is 60% KNO_3 and 40% $NaNO_3$ (weight) [8], which is commonly called "*Solar Salt.*" However, the use of molten salts has several techno-economical disadvantages, such as a higher operational temperature of around 600 °C [185] due to their chemical stability limit. That constraint also represents a thermodynamic limit for achieving higher conversion efficiencies through the implementation of advanced and efficient power cycles. In addition to that, the salt must not operate at temperatures lower than the freezing point, which is 228 °C for solar salt [186].

The CSP industry and the scientific community have devoted significant efforts during the last years to develop new concepts in central receiver systems and thus achieve higher energy conversion efficiencies. In that context, the utilization of compressible gases cycles has received considerable attention in recent years. Among the cycles analyzed, the use of supercritical CO_2 and atmospheric air have been pointed out as interesting candidates for the future developments, since these operate in a wider temperature range and achieve higher conversion efficiencies [187, 188].

Atmospheric air has been analyzed since the early 90s as a potential working fluid in CSP plants [189]. The use of atmospheric air as a working fluid has several advantages: it is nontoxic, low-cost, readily available, environmentally friendly, and chemically stable at high temperatures [64]. This last feature is crucial for achieving a higher conversion efficiency [190]. In that regard, several prototypes of volumetric receivers have been tested [191], which have led to the construction of two demonstrative plants using air as a working fluid: Jülich (Germany - 1.5 MW) and Daegu (Korea - 200 kW). Although those plants were able to validate the concept, the technology still has to overcome several challenges to achieve its commercial maturity. One of those critical issues is the integration with thermal storage systems [192].

One of the strengths of using compressible gases as a working fluid is the possibility of exploring thermal storage options with higher energy density and lower costs than the molten salts' technology (as shown in Table 3.1). Among the storage technologies that have been analyzed for coupling to CSP systems using air as a working fluid, single-tank packed-bed storage has been pointed out by several authors as the most suitable alternative [16, 11].

3.1.1 Packed-bed thermal storage

A packed-bed thermal storage system consists of using solids as a heat storage medium and a heat transfer fluid (HTF) in direct contact with solids to convey heat [25]. Figure 3.1 shows a generic scheme for a central receiver plant coupled to a packed-bed storage where the solar radiation is absorbed in the receiver of the solar tower, and the heat transfer fluid is later conveyed to the power block. In cases when a surplus of energy exists, it is conveyed to the thermal storage system. Later, during low radiation periods, the thermal storage is discharged by delivering heat to the power block, allowing it to continue its operation. Comparing packed-bed systems with the currently dominating storage technology in CSP

Table 3.1: Sensible heat energy storage alternatives (experimental and commercial scale)

Storage configuration	HTF	Storage material	Material cost [\$/kg]	Temperature range [°C]	Energy density [kWh/m^3]	Cost [\$/kWh]	Ref.
Two tank storage	Water/steam	Hitec/HitecXL	0.9 - 1.2[193]	220 - 340	97		[8, 194]
	Molten salt	Molten salt	0.5[193]	288 - 566	206 - 270	24 - 26[194] (system)	[8, 13]
	Air (demo)	Molten salt	0.5[193]	220 - 565	206 - 270		[8]
	Synthetic oil	Molten salt	25 (oil)[67]	288 - 388	80		[8]
Single tank thermocline storage	Air	Reinforce concrete	0.06	200 - 400	100	1.0	[13, 194]
	Air	Rocks and fire bricks	0.15 - 2.0[13]	20 - 700	400 - 600	4.2 - 6.0	[25, 12]
	Thermal oil	Quartzite	0.6[62]	100 - 400	250	n.a.	[51]
	Molten salt	Cofalit	9.7 [18]	290 - 560	200	n.a.	[195]
Steam accumulator	Steam (DSG)	Steam	–	120 - 330	20 – 30	0.17 - 0.34	[8, 194]

plants (molten salts), the main advantages of packed-bed systems are the following: the operating temperature constraints due to chemical instability of the HTF or the rocks are eliminated; the operating pressure can be close to ambient, avoiding the need for complex sealings; and thermal storage can be incorporated directly after the receiver, eliminating the need for heat exchangers between the HTF and the thermal storage medium [16].

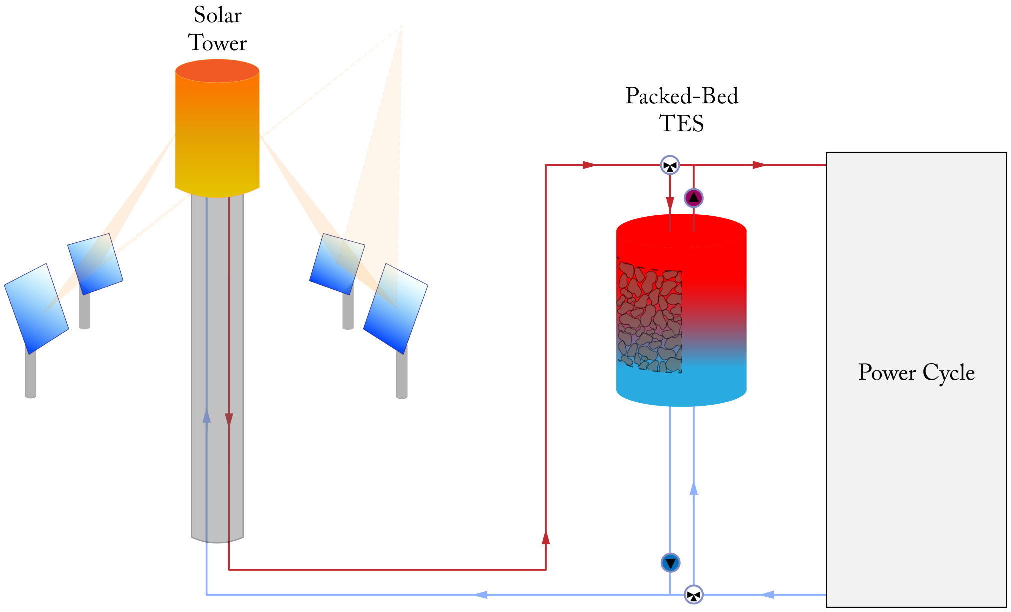

Figure 3.1: Packed-bed storage integrated with central receiver CSP system

Some of the disadvantages of packed-bed systems using air as HTF are associated to the large mass flow rate and the surface area needed, due to air's low volumetric heat capacity and thermal conductivity [16]. These drawbacks imply higher pressure drops and energy losses [11]. That issue is explained because the absolute and relative dimensions of the tank as well as the solid elements of the bed influence flow distribution and velocity profiles, significantly affecting the heat transfer phenomena and the thermal stratification in the storage [48]. Research has demonstrated that the relative influence of the walls over velocity profiles is higher in small tanks than in large tanks due to edge effects [27]. Flow channeling near the walls is also influenced by the tank-to-particle diameter ratio, which must be carefully addressed for storage system's yield assessment [48].

In terms of the design variables of the tank that affect the thermal behavior of the storage system, the cross section area is fundamental. Although most of the systems reported a cylindrical shape [16, 142, 36], recent works have opted for a truncated conical tank [27, 196], aiming to reduce the thermomechanical stresses observed in cylindrical tanks (even though it reduces its thermal performance and increases the pressure drop). Consequently, the design of packed-bed storage systems results in a trade-off evaluation among mechanical performance, flow distribution, pressure drop, thermal losses, and stratification easiness. The packed-bed systems reported in the literature commonly present height and diameter of the same order of magnitude [48], which increases compactness of the storage and hence reduces thermal losses.

Achieving high efficiency for energy storage in packed-beds is closely related to keeping a high degree in thermal stratification during cycling operation. Research has shown that high energy recovery is achieved when a small amount of mixing occurs between the hot and cold zones in the storage tank. Thus, it is crucial for the control system and the shape of the thermal front. Fluid flow conditions also need to be considered (e.g. the minimization of the pressure drop allows the extraction of more useful energy from the system [36]).

Many studies have proposed assessing the performance of packed-beds through the first law of thermodynamics, or what is called "round-trip efficiency." The latter is defined as the ratio between the useful energy released from the storage system during the discharging process and the energy delivered to the system during the charging process [197, 198]. Li et al. [200, 199] carried out a thorough analysis that considered multiple dimensionless numbers. The authors stated that the first law's efficiency (η) for these systems is primarily a function of the following: the ratio between the dimensionless charge and discharge time, a dimensionless quantity that relates the mass flow rate, the heat capacity of the fluid, the height of the packed-bed, and the surface area of the filler material per unit length; and the ratio between the fluid heat capacitance and the filler heat capacitance.

Other authors have indicated that thermal storage systems used for power generation should be designed and evaluated by methods considering the 2^{nd} law of thermodynamics [201] (exergy). Exergy analysis assesses the potential power losses generated from operational conditions, such as pressure drop and its effect on the energy required for pumping [89]. Torab and Beasley [202] showed the existence of a tipping point where the total exergy available increases with decreasing particle diameter and enlarging the height of the storage tank, resulting in pumping energy requirements. Moreover, regarding the mass flow rate, exergy efficiency is higher for smaller flows because the thermal diffusion and mixing effects produce low exergy destruction [145]. Mctigue et al. [39] went one step forward in the assessment, establishing a balance between the entropy rejected at the exit of the storage and the internal entropy generated by irreversibilities. That balance allowed them to determine a trade-off between round-trip efficiency and energy density.

3.1.2 Packed-bed systems using waste materials

As reported in the literature, the pilots of packed-bed storage systems implemented are mainly at the laboratory and prototype scales, while very few at the commercial scale [48]. Several filler materials have been tested (e.g. natural rocks, asbestos, concretes, and industrial byproducts) and assessed in terms of cost reduction potential. One of the potential options is using industrial byproducts that have an extremely low cost and favorable thermal properties [54, 59].

Filler materials in packed-bed systems should be able to operate in a wide range of temperatures (from 50 °C to 1100 °C) and have a stable performance for a large number of thermal cycles, as reported in several studies [203, 56, 204, 54]. The use of recycled materials particularly from metallic industrial processing, such as the steel making process and its variations (electric arc furnace, induction furnace), has been assessed due to high availability, the large amount of material produced, and the thermal performance of the slag. Additionally, due to the absence of a market for industrial slag, its cost is practically null as compared to other sensible heat storage materials presented in Table 3.1.

Ortega-Fernández et al. [18] concluded that steel slag from the electric arc furnace (EAF) process is thermally stable up to 1100 °C; moreover, the structure of the slag influences in the thermal properties as it increases its temperature: higher crystallinity results in a decrease of the specific heat and an increase on thermal conductivity (See Table 3.3). Wang et al. [58] analyzed the thermophysical properties of EAF slags as well. However, they considered samples from two different countries and included a wear behaviour analysis of the slag rocks, concluding their suitability for TES in a packed-bed configuration. As for other types of industrial byproducts, copper slag from the pyrometallurgical processing of copper ore has been brought to discussion in the last decade, as reported by Navarro et al. [59], where the thermophysical properties of copper slag as an aggregate for mortar mixtures and other types of recycled materials were characterized and compared to molten salts based on their techno-economical advantages. This case study determined that these materials performed better in terms of energy density at a lower cost than molten salts.

A parametric study developed by Ortega-Fernández et al. introduced guidelines for the optimal design of a packed-bed using industrial byproducts. The authors analyzed the behavior of storage capacity and round-trip efficiency by varying the aspect ratio of the storage, mass flow rate, and particle diameter. Hence, for a fixed mass flow rate, aspect ratios close to 2 showed promising results in terms of thermal performance. These results also suggest the importance of maintaining a certain balance between mass flow rate and particle diameter to compensate for heat transfer mechanisms in storage and prevent the spread of the thermocline [31].

The first attempt at using copper slag as sensible heat material was proposed in 1980 by Curto [205], due to the advantages offered by its thermal properties, especially considering that this byproduct has a high percentage of ferrous compounds. In addition to that, up to date copper slag has no subsequent use, and therefore, it has a negligible value. It is a waste material with high availability, especially in Chile.

As stated by Curto [205], the application of copper slags as a filler material in packed-bed storage systems has significant advantages for being used in gas power cycles and industrial processes. It could be used in a relatively high operation temperature range: from 650 °C to 1200 °C, remaining chemically, thermally, and mechanically stable. The thermophysical properties reported initially ranged between 4.3 to 4.4, for the specific gravity, while the heat capacity ranges between 0.670 kJ/(kg K) to 1.004 kJ/(kg K), within a temperature range between 20 °C to 1000 °C. Curto [205] assessed the use of copper slags in a packed-bed tank of 21 000 m^3 using air as HTF and showed outstanding performance. Despite the high potential and cost effectiveness exhibited by copper slags, this performance has not been sufficiently studied in the literature or in engineering applications.

The present work describes the assessment of the potential use of copper slags as filler material in packed-bed storage systems. One of the contributions of the present study is extending the characterization of copper slags by including data of slag from two Chilean foundries, considering the high heterogeneity expected in the thermophysical properties of copper slags. Such heterogeneity is due to their origin and solidification rates after the smelting process. Thus, the variations in the thermophysical properties impact significantly on their performance as a storage material. Another achievement of the present work is a comparison of the thermal performance of copper slags against other industrial byproducts commonly used, and considering several storage configurations.

The article describes the processes for the thermal characterization of the material (section 3.2). Considering the thermal features of the slag, a numerical 1D model is developed and described in section 3.3, which has been validated against data from the literature (subsection 3.3.2). The analysis considers 1^{st} and 2^{nd} law efficiencies as performance indicators. A parametric analysis is conducted for assessing the performance of packed-bed storage systems using copper slags, configured in applications of constant Reynolds number. The proposed analysis aims to identify the best application scenarios for the slags and to extend the methodology initially proposed in [31], allowing a direct comparison between the systems (section 3.4). Finally, a detailed analysis of the results is presented in terms of the round-trip and exergy efficiencies (section 3.5).

3.2 Thermal characterization of copper slags

Copper slag is a byproduct of the pyrometallurgical processing of copper ore, mainly due to copper sulphides processing. During matte smelting, two separate liquid phases are formed: copper-rich matte (sulphides) and slag (oxides). The formation of such phases is explained by the sulfiding process of copper ore, which results in the formation of Cu_2S and FeS. The latter continues to react and oxidizes until silica (SiO_2) is added to the smelting process, forming what is known as copper slag, with a primary composition of FeO and SiO_2 [206].

The production of one ton of copper generates approximately 2.2 to 3 tons of copper slag [207]. The options for making use of the copper slags include recycling, metal recovering, production of value-added products (e.g. cement), and disposal in stockpiles. Currently, copper slags are also being widely used for abrasive tools, roofing granules, cutting tools, abrasive tiles, glass, road-base construction, railroad ballast, asphalt pavements, cement and concrete industries [208].

Copper slags have an irregular shape, as observed in Figure 3.2. The material possesses a highly variable density, ranging between 3 to 4 g/cm^3, depending on the amount of iron content. The water absorption of copper slag is relatively low, but it depends on the cooling method applied after the smelting process. Slowly cooled slag forms a dense, hard crystalline product, whereas quick solidification generates a granulated amorphous slag. Thus, granulated copper slag presents a higher water absorption compared to air-cooled copper slag [207].

Figure 3.2: View of copper slag samples

3.2.1 Thermophysical properties

Samples of copper slags from two different foundries were analyzed E slag (ES) from the *Chilean National Mining Corporation (ENAMI)* [209], and C slag (CS) from the *National Copper Corporation of Chile (Codelco)* [210]. In order to determine the main thermophysical properties, the tests described in the following sections were performed.

3.2.2 Thermogravimetric Analysis (TGA)

The thermal stability was analyzed through TGA tests considering a temperature range from room temperature (RT) to 800 °C and three heating runs for each sample, at a temperature rate of 10 °C/min. The equipment employed for the analysis consisted in TGA Q50 by *TA Instruments* (see Table 3.2), using a N_2 atmosphere.

The results from the TGA analysis for the ES and CS samples are presented in Figure 3.3. The first heating run of each sample presented a slight mass decrease during the heating process at temperatures below 400 °C, where the mass loss in both cases is about 0.2 % of the initial mass. It is likely that the initial mass decrease results from the evaporation of water and volatile compounds present in the slag, as it is stated in [18] and [58] on their respective analysis of electric arc furnace (EAF) slags. In temperatures higher than 400 °C the mass of the samples started to increase about 1 % to 2 % of the mass at that point. It is likely that the mass gain is caused by oxidation of elements on the sample surface, such as metal oxides presented in slags of this sort that increase their oxidation rate at higher temperatures [211]. On the other hand, during the second and third heating runs, only a slight mass increase is observed, represented by a lower slope, showing a total gain of 0.5 % of the initial mass, which is a value small enough that allows to consider that thermal stability is reached after

Table 3.2: Accuracy performance of the equipments used for properties measurements.

Equipment	Model	Performance	Accuracy
TGA	Q50 TA instruments	Weighing	±0.1%
DSC	Q20 TA Instruments	Temperature	±0.1 °C
		Calorimetric	±1%
DSC	DSC 4000 PerkinElmer	Temperature	±0.1 °C
		Calorimetric	±2%
SH-1 dual sensor	KD2 PRO Decagon Devices	Thermal conductivity	±10% (0.2 to 2 W/mK) ±0.01 W/mK (0.02 to 0.2 W/mK)
		Volumetric specific heat	±10% (at k above 0.1 W/mK)

the third heating cycle. Thermal stability of TES materials is essential since their purpose is to operate in continuous heating cycles during the storing process.

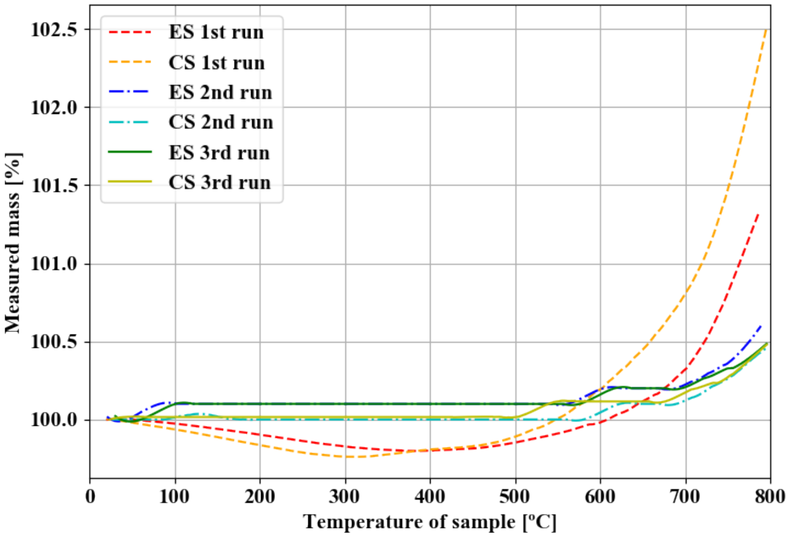

Figure 3.3: TGA results for samples ES and CS

3.2.3 Differential Scanning Calorimetry (DSC)

The specific heat capacity (c_p) of copper slag samples was analyzed through a DSC testing in a large range of temperatures, from room temperature and up to 500 °C. The tests were performed considering N_2 and Ar atmospheres, at a temperature heating rate of 10 °C/min. The equipment employed (see Table 3.2) for the tests was a DSC Q20 by *TA Instruments* and a DSC 4000 system by *PerkinElmer* (maximum temperature of operation of 450 °C). The samples were classified depending on their preparation method, primarily on whether or not the samples received the previous heating treatment up to 800 °C.

For DSC, testing can be carried out by applying different theoretical approaches for measuring the specific heat (c_p). For the test carried out in the present work, the heat flow required for the sample to reach a specific temperature was registered. Then, by using the corresponding software, the system's signal bias was removed. Through Equation 3.1 and Equation 3.2, the apparent c_p was calculated, where H is the heat flow adjusted after defining the baseline, m the mass of the sample, and β the temperature increase rate for the test [212].

$$c_p = \frac{H}{m\beta} \tag{3.1}$$

$$\beta = \frac{\Delta T}{t} \tag{3.2}$$

Figure 3.4 presents the results of the DSC runs in terms of the c_p, for samples ES and CS, under Ar and N_2 atmospheres. The apparent c_p profiles shown in Figure 3.4 are identified as XX-Y-Z, where XX denotes the foundry, Y the atmosphere considered for the test, and Z the sample number. It should also be noted that the samples were tested as received from the foundry plant; thus, no previous heating treatment was performed. As previously stated, copper slag is a highly heterogeneous material inducing a high variation between the results from one sample to another. This effect is probably caused by different solidification rates of the slag after the smelting process, creating glassy and crystalline structures in different proportions within the slag. Nonetheless, there are temperature marks at which the c_p curves behave similarly; specifically throughout the first 200 °C to 250 °C, most of the curves behaved practically stable. In contrast, at higher temperatures, the c_p curves started to decrease at different rates and presented peaks of possible chemical reactions or phase transitions. Only sample ES-N-ST received a previous heating treatment (three cycles) up to 800 °C, and indeed that sample shows a c_p profile that increases steadily with the temperature. Based on that result, it can be argued that the heating treatment allows the completion of reactions during the smelting process, and therefore, the sample is thermally stabilized before the DSC testing. Such behaviour is similar to the c_p measurements reported by Ortega-Fernández et al. [18] and Wang et al. [58]. ES-N-ST slag sample was analyzed during the heating and cooling processes, presenting almost equivalent results for the c_p, ranging from 0.8 J/gK to 1.1 J/gK. These values are similar to the measurements of c_p reported by Navarro et al.. The overall results for the c_p observed in the test carried out without precooking were considerably higher, ranging from 1.4 J/gK to 2.1 J/gK; yet, they were highly unstable. Nonetheless, the results for the c_p are still higher than conventional solid storage materials and the measurements reported for EAF slag in the literature (see Table 3.3). These results, however, must be interpreted with caution because the performance of the stabilized material assessed only up to 450 °C, due to restrictions on the equipment employed; therefore, further tests with a higher number of samples and at higher temperatures would be useful.

3.2.4 Thermal conductivity and density

The Transient Line Source method (TLS) (Figure 3.5) was applied in order to determine the thermal conductivity of the copper slag samples, using the KD2 Pro equipment by *Decagon Devices*. This equipment measures the thermophysical properties of rocks and soils. Through a double needle sensor (SH-1) (see Table 3.2), thermal conductivity and the specific heat were measured. Six samples were analyzed (see Table 3.4) at room temperature and atmospheric conditions.

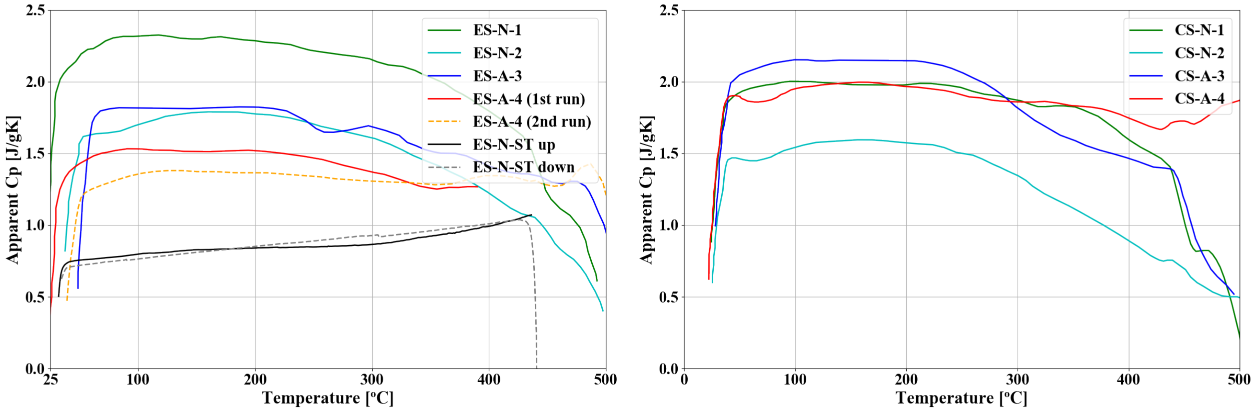

(a) Results from the DSC tests for the ES samples (b) Results from the DSC tests for the CS samples

Figure 3.4: Apparent c_p as a function of temperature obtained from the DSC analysis

It is clear from the results in Table 3.4 that the thermal conductivity values differ significantly from one sample to the other, and the values regarding the thermal conductivity (k) are higher than those reported by Navarro et al.. However, the results for c_p are of the same order of magnitude than those measured by the DSC at room temperature.

The slag samples from each foundry plant presented an average density of 3456 kg/m^3 and 3715 kg/m^3, and high standard deviations: 811 kg/m^3 and 606 kg/m^3, respectively. These values are consistent with the density values reported in the literature.

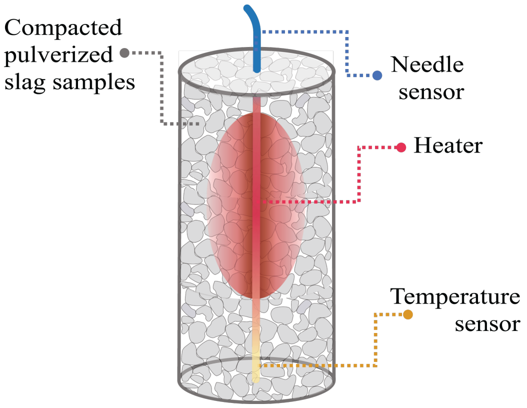

Figure 3.5: Transient line source method apparatus scheme

Table 3.3: Thermophysical properties results from the present work and the literature

Type of slag	Sample id	ρ [kg/m^3]	k [W/(m K)]	c_p [J/(g K)]	c_p[a][J/(g K)]	Thermal stability [°C]	Ref.
Copper	ES-N[a,b]	3500	1.595	0.7 - 1.1	0.9 (338 °C)	up to 800	-
Copper	ES-A[a]	3700	2.173	1.4 - 1.5	1.45 (338 °C)	up to 800	-
Copper	Curto C. Slag	4350	-	0.670 - 1.004	-	up to 1200	[205]
Copper	Slag P[a]	3600	0.8	0.571 - 1.180	0.683 (300 °C)	up to 800	[59]
Copper	Slag B	3700	1.1	0.650 - 0.990	-	up to 800	
Steel	EAF 1[a]	3430	1.47	0.865	0.865 (350 °C)	up to 1000	[19]
Steel	EAF 2	4110	1.51	0.837	-	up to 1000	
Steel	Slag 1	3430	1.65 - 1.23	0.710 - 0.950	-	up to 1100	[18]
Steel	Slag 2	3770	1.50 - 1.73	0.690 - 0.890	-	up to 1100	
Steel	S slag	3600	1.695 - 1.74	0.713 - 0.858	-	up to 1000	[58]
Steel	C slag	3700	1.84 - 1.75	0.717 - 0.975	-	up to 1000	

[a] Values considered for the parametric analysis
[b] Sample thermally stabilized

Table 3.4: Results from KD2 Pro analysis using the double needle sensor SH-1

Sample id	k [W/(m K)]	ρ [kg/m^3]	c_p [J/(g K)]
ES-1	2.173	3700	1.415
ES-2	1.595	3500	0.668
ES-3	1.537	3769	0.732
ES-4	2.210	3700	0.922
ES-5	1.682	3519	0.819
ES-6	1.600	3588	1.198

3.3 1-D Modeling of a copper slag packed-bed storage

To assess the potential of copper slags as a storage material, a heat transfer model is proposed in order to compare its performance against other slags reported in the literature. The domain consists of a cylindrical tank which is filled with rocks from top to bottom, and air flowing through the voids generated by the arrangement of the pile surrounding the particles. The details of the heat transfer analysis and the validation of the model are described in the following sections.

3.3.1 Heat transfer model

A 1-D transient model was developed by coupling the heat transfer equations of the solid and fluid phases, as well as considering convection and conduction heat transfer based on the Continuous Solid model (*C-S*) [118]. In that context, the proposed model considers the following basic assumptions to study heat transfer in packed-bed systems [16, 48]: (i) plug flow is assumed in the fluid phase to prevent mixing and keep the fluid stratified [213, 48], (ii) there is neither mass transfer between the phases nor internal heat generation, (iii) the temperature gradient in the radial direction is neglected, (iv) radiation heat transfer is not considered in the analysis, (v) heat conduction is neglected in the fluid phase since the airflow makes advective effects predominate over the diffusive ones, (vi) there is an uniform temperature of the particles due to $Bi \leq 0.1$, (vii) void fraction is constant in the radial and axial direction, (viii) the thermal gradient in the isolation wall of the storage tank is not considered, and (ix) the shape of the rocks is approximated to spheres of uniform size.

Moreover, for the solid and fluid phases, the thermophysical properties are considered constant and are evaluated at the average operating temperature $T = \left(T_{\text{in}} + T_{\infty}\right)/2$. The energy balances for each phase are presented in Equation 3.3 and Equation 3.4:

$$\varepsilon \rho_f c_{p,f} \frac{\partial T_f}{\partial t} + \varepsilon \rho_f c_{p,f} w \frac{\partial T_f}{\partial z} = h_v \left(T_s - T_f\right) + \frac{U_T \left(\pi D_T\right)}{A_T} \left(T_\infty - T_f\right) \tag{3.3}$$

$$\left(1 - \varepsilon\right) \rho_s c_{p,s} \frac{\partial T_s}{\partial t} = h_v \left(T_f - T_s\right) + k_{s,eff} \frac{\partial^2 T_s}{\partial z^2} \tag{3.4}$$

where the subscripts f and s refer to the fluid and solid phases, respectively. The term h_v is the volumetric heat transfer coefficient between the fluid and the solid surface. Several experimental correlations are used to characterize the phenomenon analyzed herein, showing good agreement with the experiments and constituting a good approach to predict the convective heat transfer between the phases. Among the correlations reported in the literature those proposed by Coutier and Farber, Pfeffer, Wu and Hwang stand out due to their different approaches to determine the h_v value [42, 214, 112]. A detailed analysis of these correlations is presented in subsection 3.3.2 along with the selection of the present model, which is based on the mean percentage error (MPE) that the temperature profile of the model presents against the experimental data.

Regarding effective thermal conductivity, many correlations have also been proposed depending on the different assumptions established for the heat transfer model [85]. Since in the present work the radiation effects are neglected, conduction heat transfer should represent the interaction between the adjacent rocks and between the HTF and the rock. Thus, considering that the air fills the voids in the tank, Equation 3.5 for the conductivity holds:

$$k_{s,eff} = \varepsilon k_f + \left(1 - \varepsilon\right) k_s \tag{3.5}$$

The boundary conditions for each of the processes developed in the storage tank are depicted in Figure 3.6. For the initial conditions, it is necessary to establish the temperature distribution in the tank at the beginning of the initial charging process, as shown in Equation 3.6.

$$T_s \left(t = 0\right) = T_f \left(t = 0\right) = T_\infty \tag{3.6}$$

Meanwhile, for the discharging process, the temperature distribution is equivalent to the distribution observed at the end of the charging process. Thus, the expressions presented in Equation 3.7 and Equation 3.8 hold the following for the first and subsequent discharging processes:

$$T_f\left(t=0\right)=T_f\left(t_{\mathrm{end}}\right) \tag{3.7}$$

$$T_s\left(t=0\right)=T_s\left(t_{\mathrm{end}}\right) \tag{3.8}$$

where t_{end} represents the time when the previous process finishes.

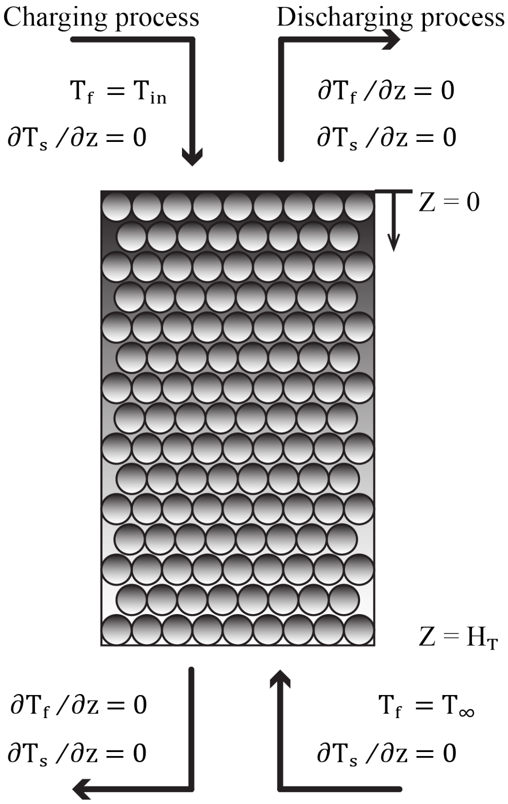

Figure 3.6: Scheme of the boundary conditions for modelling charging and discharging processes

The coupled system of partial differential equations (PDE) is solved using a numerical method based on finite differences. The first-order forward scheme for time derivatives was used, the Lax-Wendorff explicit scheme was considered for first-order derivatives in z, and the central difference was used for second-order derivatives [215]. To ensure numerical stability, the Courant Friederichs-Lewy condition is applied to the fluid phase [216]: $CFL = \left(w\Delta t\right)/\Delta z < 1$, and $\Delta t < \frac{1}{2}\Delta z^2 \frac{(1-\varepsilon)\rho_s c_{p,s}}{k_{s,eff}}$ to the solid phase, which are the results of the Von Neumann stability analysis considering the equations above, without the source terms [215]. The numerical algorithm was programmed in Python, where the library CoolProp was employed to determine the thermophysical properties of the air at the given states [217]. The simulation was executed by setting the basic parameters at the beginning of the first charging process, such as the number of operation cycles, the air inlet temperature, the air mass flow rate, the dimensions of the storage tank, the solid's thermal properties, and the number of grid points used in the spatial domain. The time-step is calculated by applying

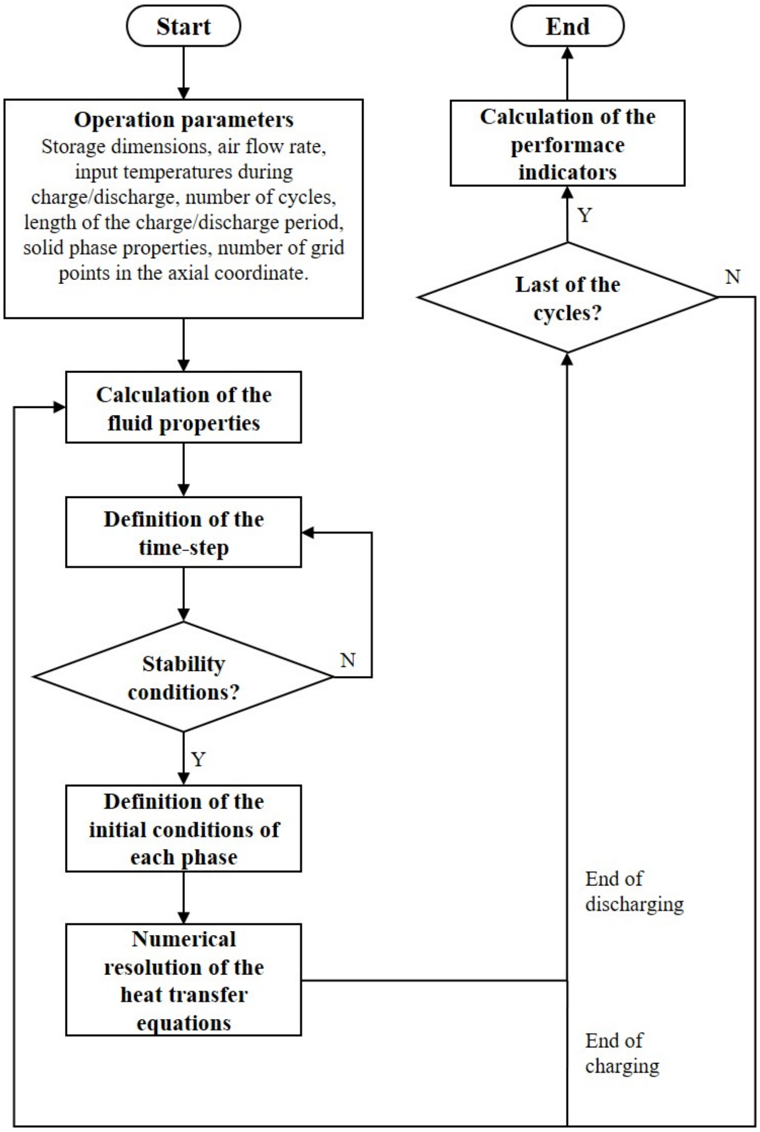

Figure 3.7: Flowchart of the numerical algorithm to solve the cyclic operation of the storage.

the stability conditions mentioned above. Then, for each time-step, the discrete PDEs were solved explicitly, which helped to determine the temperature distribution at the next time step for each phase within the whole spatial range. The temperature profiles of the phases at the end of the charging process are used as initial conditions for the discharge process; thus, considering that information, the fluid properties and the heat transfer coefficients are recalculated, so the same code is implemented for the discharge and the next operation cycles analyzed. Figure 3.7 shows a scheme of the algorithm, which includes the process for determining the performance indicators discussed in the following sections.

3.3.2 Model validation

The validation of the thermal model was carried out by comparing its results against the data from the experimental setup developed by Meier et al. and reported in [34]. The test bench consisted of a vertically oriented packed-bed of crushed steatite inside of a cylindrical stainless steel vessel. The data was also used by Hänchen et al. to validate their own model [16], using the parameters listed in Table 3.5.

Table 3.5: Parameters of the experimental study by Meier et al. [34]

Parameter	Value
T_{in}	823 K
T_∞	293 K
G	0.225 kg/(m^2 s)
H_T	1.2 m
D_T	1.48 m
A_T	0.0172 m
ε	0.4
d	0.02 m
ρ_s	2680 kg/m^3
$c_{p,s}$	1068 J/(kg K)
k_s	2.5 W/(m K)
U_T	0.678 W/(m^2 K)

The results of the comparison between the proposed model and the experimental results reported in the literature are assessed in terms of the mean percentage error (MPE), which is calculated with the formula in Equation 3.9 and presented in Table 3.6. The results are assessed considering different correlations for the h_v, identified by the respective authors listed in Table 3.6. Additionally, the use of the temperature-dependent fluid properties approach against the constant fluid properties simplification explained above are contrasted. As observed, the most accurate correlation is suggested by Coutier and Farber, showing an error lower than 2% for both cases, while using temperature-dependent fluid properties exhibits an improvement on the error by less than 0.5%. In that context, employing fluid properties calculated at the mean working temperature is an acceptable assumption for a parametric analysis.

$$\text{MPE} = \frac{1}{N} \cdot \sum_{\text{i}=1}^{N} \frac{|T_{p,\text{i}} - T_{m,\text{i}}|}{T_{m,\text{i}}} \tag{3.9}$$

where $T_{p,\text{i}}$ is the i-th predicted temperature by the model at the same axial position and time instant of the i-th measured temperature $T_{m,\text{i}}$, and N is the total number of experimental data.

Finally, the analytical model is contrasted with the experimental results extracted from [16] in Figure 3.8. Using the h_v correlation proposed by Coutier and Farber, it can be noticed a good agreement between the predicted values and the temperature data along the tank reported at time instants 1200, 3000 and 4800 s.

Table 3.6: MPE of the model considering different h_v correlations

		MPE %	
Author	Correlation	Constant fluid prop.	Temp-dep. fluid prop.
Coutier and Farber [42]	$700 \cdot \left(\frac{G}{\mathrm{d}}\right)^{0.76}$	1.82	1.39
Pfeffer [214]	$6 \cdot \frac{(1-\varepsilon)}{\mathrm{d}} \cdot \left(1.26\left(\frac{1-(1-\varepsilon)^{5/3}}{W}\right)^{1/3}(c_{p,f}G)^{1/3}\left(\frac{k_f}{\mathrm{d}}\right)^{2/3}\right)$ with $W = 2 - 3\gamma + 3\gamma^5 - 2\gamma^6$ and $\gamma = (1-\varepsilon)^{1/3}$	3.13	2.74
Wu and Hwang [112]	$6 \cdot \frac{(1-\varepsilon)}{\mathrm{d}} \cdot \left(\frac{k_f}{\mathrm{d}}\right) \cdot \left(0.32\left(\frac{G\mathrm{d}}{\mu_f}\right)^{0.59}\right)$	4.32	4.23

3.4 Parametric analysis

The parametric analysis enabled the assessment of the storage materials described in the previous sections as well as the potential of copper slag as a new candidate for a storage medium. The proposed model is used to analyze different scenarios of packed-bed systems' design and rating, in terms of the storage tank dimensions (i.e., storage volume V_T and aspect ratio $AR = H_T/D_T$). As for the other parameters, they are considered as constant. In order to make the evaluated scenarios fully comparable, dimensionless numbers are considered for characterizing the phenomena occurring within the flow of the working fluid and the heat transfer to/from the storage medium. It should be noted that this analysis does not consider thermal losses to the ambient.

3.4.1 System description

Several input parameters are defined for characterizing the operating conditions of the storage tank in different scenarios. As mentioned, in order to make cases fully comparable, dimensionless numbers such as Reynolds and Biot were studied in depth. By keeping the Reynolds number constant, it is ensured that all cases exhibit the same flow regime. The ratio D_T/d is also relevant for neglecting the wall effects of the fluid flow [16]; therefore, a single particle diameter was chosen in order to keep the value of $D_T/\mathrm{d} \geq 40$, as suggested by Meier et al. [34]. Finally, the Biot number is also evaluated for each material, aiming to verify if the suggested parameters exceed the $B\mathrm{i} \leq 0.1$ limit, which implies that neglecting thermal gradients within particles is no longer valid. Regarding modelling, the analysis considers a single tank initially at ambient temperature. Then the charging process is simulated as hot air flows through the tank for 8 hours. The discharging process is simulated afterwards, considering that cold air flows through the packed-bed during the same number of hours. Those consecutive processes are repeated for 3 cycles aiming to capture the effect of the previous cycles in the amount of stored energy. After 3 cycles, the subsequent temperature profiles have no significant change in thermocline shape beyond an increase in temperature at the

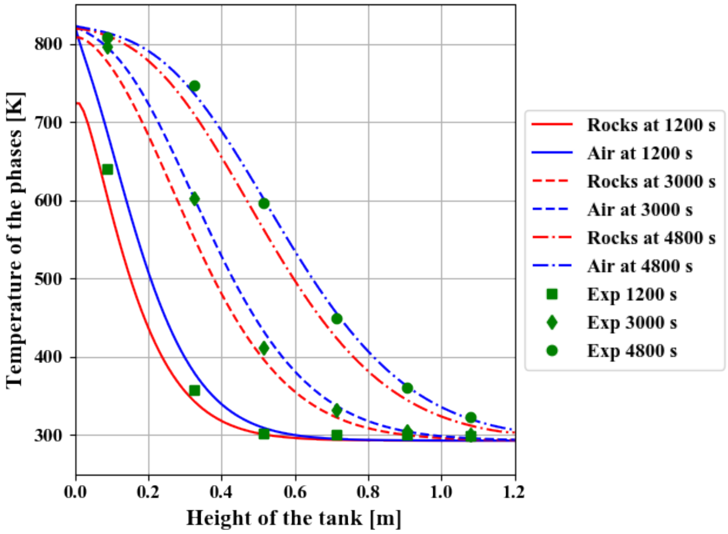

Figure 3.8: Comparison between the proposed model and experimental data from Hänchen et al.

bottom of the tank.

The heat transfer model and the boundary conditions are equivalent to the equations presented in subsection 3.3.1. Table 3.7 shows the values of the storage's input conditions, where G and d are chosen to ensure that the turbulent regime is not reached in the packed-bed ($Re < 300$ according to Dybbs and Edwards [218]) and that no temperature gradient is developed in the rocks ($Bi \leq 0.1$). Both values of the adimensional numbers are illustrated in Table 3.7 and were calculated considering the fluid properties at mean operating temperature for all the materials assessed in the parametric analysis. In contrast to previous works, such as Ortega-Fernández et al., where the mass airflow rate is kept constant and the aspect ratio varied, in the present study, an analysis considering a fixed Reynolds number is performed. The minimum and maximum values of the aspect ratio and the tank volume are shown in Table 3.7, where the range chosen is subject to the restriction $D_T/\mathrm{d} \geq 40$ and $Bi \leq 0.1$ considering a given airflow and particle diameter for the different filler materials assessed. Thus, for each combination of (AR, V_T) there is a storage tank that is evaluated with different filling materials.

3.4.2 Performance indicators

To facilitate the assessment of the packed-bed configurations, several performance indicators defined in the literature are used in the context of the present work. The indicators considered are the following: the amount of energy that the medium is capable to store after several cycles of operation, the ratio between the energy extracted by the fluid and the energy initially supplied to the system. In addition to that, a simplified exergy analysis was carried out, which measured the effectiveness of the storage in terms of the useful work that it can provide.

Table 3.7: Operating conditions considered in the parametric study

Parameter	Value
T_{in}	923 K
T_∞	293 K
G	0.025 kg/(m^2 s)
ε	0.4
d	0.017 m
AR	from 1 to 2
V_T	from 0.5 to 2.5 m^3
charge/discharge time	8 h
Re	23.1
Bi range	0.034 - 0.094

Energy density

Energy density is defined as the amount of energy that can be stored by the filling material in a given volume, and it is evaluated at the end of the charging process. The energy stored in the packed-bed is expressed as

$$E_{st} = \int_{z=0}^{z=H_T} (1-\varepsilon)\rho_s c_{p,s} A_T \left(T_s(z, t=t_{\mathrm{end}}) - T_s(z, t=t_{start})\right) \mathrm{d}z \tag{3.10}$$

where t_{end} is the time at the end of the charging period, and t_{start} is the time at the start of the charging process or at the end of the previous cycle's discharging process. Finally, the energy density is expressed as follows:

$$\hat{E}_D = \frac{E_{st}}{V_T} \tag{3.11}$$

where V_T is the total volume of the storage tank.

Round-trip efficiency

Round-trip efficiency is defined as the ratio between the recovered energy during the discharge process and the energy supplied during the charging process. It also considers the energy consumed by the pump/fan during those stages. The energy delivered/recovered is expressed as,

$$E_{ch/\mathrm{d}ch} = \int_{t_{start}}^{t_{\mathrm{end}}} G A_T c_{p,f} \left(T_{top} - T_{bottom}\right) \mathrm{d}t \tag{3.12}$$

where *top* and *bottom* refer to the upper and the lower zone of the tank, respectively. G is the mass flux, A_T is the cross-sectional area of the tank, and $c_{p,f}$ is the thermal capacity of the fluid phase. Furthermore, the work consumed by the pump/fan is expressed as follows:

$$W_{pump} = \int_{t_{start}}^{t_{\mathrm{end}}} \frac{A_T G}{\rho_f} \Delta p \mathrm{d}t \tag{3.13}$$

where ρ_f is the density of the fluid.

Regarding the pressure drop (Δp) across the packed-bed of rocks, it is assessed by the expression proposed by Ergun and Orning as follows:

$$\Delta p = \frac{H_T G^2}{\rho_f \mathrm{d}} \left(1.75 \left(\frac{1-\varepsilon}{\varepsilon^3} \right) + 150 \left(\frac{1-\varepsilon}{\varepsilon^3} \right) \frac{\mu_f}{G\mathrm{d}} \right) \tag{3.14}$$

where d is the particle diameter, ε is the void fraction, and μ_f is the dynamic viscosity of the fluid.

Considering the previous equations, the round-trip efficiency is defined by the following equation [11]:

$$\eta_{rt} = \frac{E_{\mathrm{d}ch}}{E_{ch} + W_{pump_{ch}} + W_{pump_{\mathrm{d}ch}}} \tag{3.15}$$

Exergy efficiency

A global exergy balance was also developed to assess the performance of the storage tank, accounting for the second law of thermodynamics. The exergy balance of the whole storage system holds Equation 3.16 [220]. For simplicity, during the charging process, it is assumed that the air is expelled to the environment and is not used for any other process. On the other hand, the air recovered during the discharge process might be used in a power cycle or industrial process, depending on the particular application.

$$\Xi_{\mathrm{in}} + W_{pump} - \Xi_{exp,ch} - \Xi_{rec} = \Xi_{\mathrm{d}est} \tag{3.16}$$

The exergy input, $\Xi_{\mathrm{i}n}$, is the high temperature air flow entering the packed-bed during the charging process. For the balance, the exergy associated to the pumping work consumed by the fan is also considered, as it enables the operation of the packed-bed. Hence, the exergy input is expressed as:

$$\Xi_{\mathrm{in}} = \int_{t_{start,ch}}^{t_{\mathrm{end},ch}} G A_T c_{p,f} T_\infty \left(\frac{T_{\mathrm{in}} - T_\infty}{T_\infty} - \ln\left(\frac{T_{\mathrm{in}}}{T_\infty} \right) + \frac{R}{c_{p,f}} \ln\left(\frac{P_{\mathrm{in}}}{P_\infty} \right) \right) \mathrm{d}t \tag{3.17}$$

where T_∞ and P_∞ are the reference temperature and pressure, respectively. R is the ideal gas constant, T_{in} is the inlet temperature during the charging process. $t_{start,ch}$ and $t_{\text{end},ch}$ are the time at the start and at the end of the charging process, respectively.

As the air expelled during the charging process increases its temperature, the outlet flow presents higher temperature than the ambient reference. Thus, this energy flow accounts as exergy that cannot be recovered as useful work, $\Xi_{exp,ch}$. Consequently, the previous situation becomes even more relevant as more storage cycles are executed. The mathematical expression of the exergy loss (waste) holds,

$$\Xi_{exp,ch} = \int\limits_{t_{start,ch}}^{t_{\text{end},ch}} G A_T c_{p,f} T_\infty \left(\frac{T_{out}(t) - T_\infty}{T_\infty} - \ln\left(\frac{T_{out}(t)}{T_\infty}\right)\right) \mathrm{d}t \tag{3.18}$$

where $T_{out}(t)$ is the air temperature at the bottom of the tank during the charging process.

The exergy balance also takes into consideration the work consumed by the air blower during the charging and discharge processes. On the other hand, the recovered exergy during discharge of the storage is calculated as follows:

$$\Xi_{rec} = \int\limits_{t_{start,\text{d}ch}}^{t_{\text{end,d}ch}} G A_T c_{p,f} T_\infty \left(\frac{T_{out,\text{d}ch}(t) - T_\infty}{T_\infty} - \ln\left(\frac{T_{out,\text{d}ch}(t)}{T_\infty}\right)\right) \mathrm{d}t \tag{3.19}$$

where $T_{out,\text{d}ch}(t)$ is the air temperature at the upper zone of the tank during the discharging process. $t_{start,\text{d}ch}$ and $t_{\text{end,d}ch}$ are the time at the start and end of the discharging process, respectively.

Finally, the exergy efficiency is determined by applying the definition in [11]:

$$\Psi_{\text{ex}} = \frac{\Xi_{rec}}{\Xi^*_{\text{in}} + W_{pump}} \tag{3.20}$$

where $\Xi^*_{\text{in}} = \Xi_{\text{in}} - \Xi_{exp,ch}$.

3.5 Results and Analysis

Considering the configuration described in section 3.4, the parametric study was carried out aiming to analyze the impact of the main design parameters of packed-bed systems on its performance considering copper slags. Thus, the following sections describe the assessment of the packed-beds in terms of the metrics previously defined.

3.5.1 Temperature profiles

The temperature profile in the packed-bed system depends significantly on the size of the storage tank and on its geometry configuration. In that context, the temperature profiles of two configuration scenarios are depicted in Figure 3.9, where the temperature profile corresponds to the end of the third charge/discharge cycle. Figure 3.9 shows the temperature profiles for different materials evaluated at different sizes and aspect ratios: a tank with an aspect ratio of 1 and a volume of $0.5\,\mathrm{m}^3$ (Figure 3.9a), and a tank with an aspect ratio of 2 and a volume of $2.5\,\mathrm{m}^3$ (Figure 3.9b). Comparing the temperature profiles of each material assessed, the proposed copper slags (ES-A and ES-N) showed a similar distribution during the operating cycles. Nonetheless, the thermophysical properties such as specific heat affected the steepness of the temperature gradient across the tank. Materials with smaller specific heat (SP sample, for instance) show a temperature profile with the highest temperature outlet during the charging process, which is not a desirable response for the TES systems. Indeed, increasing the number of cycles, the difference between the hot and cold zones would be lost due to the remaining heat stored in the material at the end of the discharge cycles. However, considering the behavior observed by the ES-A sample, using materials with high thermal capacity leads to a low spread of the thermocline within the storage, keeping the temperature profile stratified after the consecutive cycles. The previous statement can be justified with the expression of the velocity of the thermal front $v = \frac{\varepsilon \rho_f c_{p,f} w}{\varepsilon \rho_f c_{p,f} + (1-\varepsilon)\rho_s c_{p,s}}$ [221, 222] which decreases when the specific heat of the solid phase is high. Regarding the temperature profiles after the last discharge cycle, no significant differences can be observed related to the temperature of the fluid at the top of the tank for the different materials assessed.

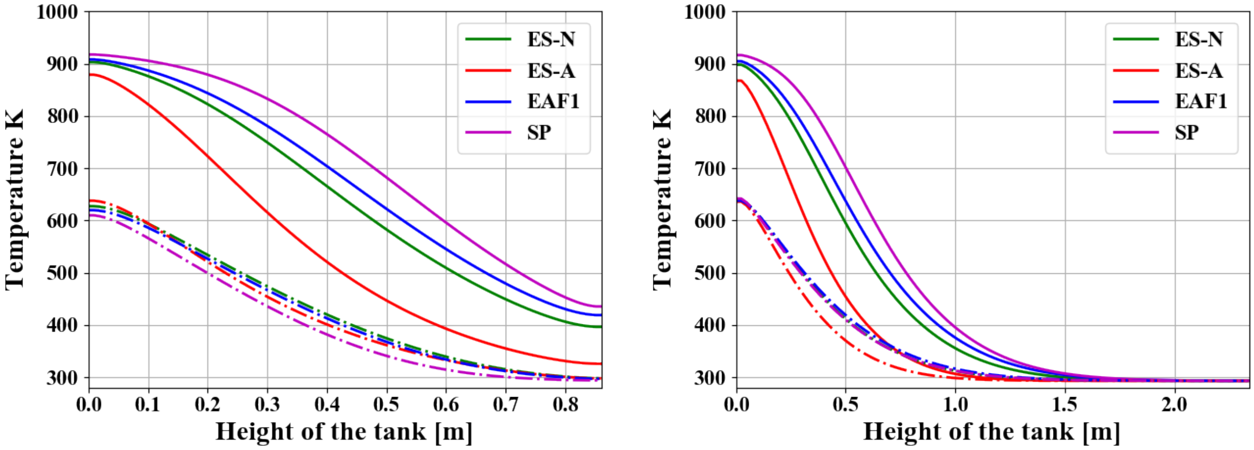

(a) $AR = 1$ and $V_T = 0.5\ m^3$.

(b) $AR = 2$ and $V_T = 2.5\ m^3$

Figure 3.9: Temperature profiles of the fluid phase at the end of the third charging (solid line) and discharging process (dashed line).

By increasing the tank's volume at a fixed aspect ratio, higher temperatures could be achieved at the tank's outlet during the discharging process. To analyze that behavior, the dimensionless temperature $\theta = (T - T_\infty)/(T_{\text{in}} - T_\infty)$ is evaluated during the charging process. Figure 3.10 shows the dimensionless temperature profile for a tank considering the ES-N slag as filler material at the end of the 3^{rd} charging and discharging cycle, with a normalization of the axial coordinate in terms of the height of the tank. In that way, all the storage volumes evaluated in the parametric analysis can be compared in the same graph and represented by a color scale. Moreover, three scenarios for the aspect ratio are shown, depicting the effect of the storage dimensions in the temperature profiles observed in the same figure. Regarding the behavior described in the figure, the outlet temperature during the charging process is lower at high volumes, as observed in Figure 3.10. The same effect is observed when the aspect ratio is increased at fixed volumes; thus, it can be deducted that the dimensions of the tank have a strong influence in the temperature profiles, for instance, with a longer rock bed, the high temperature front would require more time to go through the whole arrangement. In the lower part of the storage, the rocks temperature is incremented as the aspect ratio or the tank volume are reduced; consequently, the heat transfer rate is greater at the beginning of the discharge process, which makes the transition between the high and low temperature region in the storage less steep at the end of discharging process (see Figure 3.10). In contrast, as the aspect ratio or the tank volume are incremented, it favors a well-defined thermocline during longer periods of time, and a more intense heat transfer rate is produced at the top of the storage because of a greater temperature difference between the rock and the air.

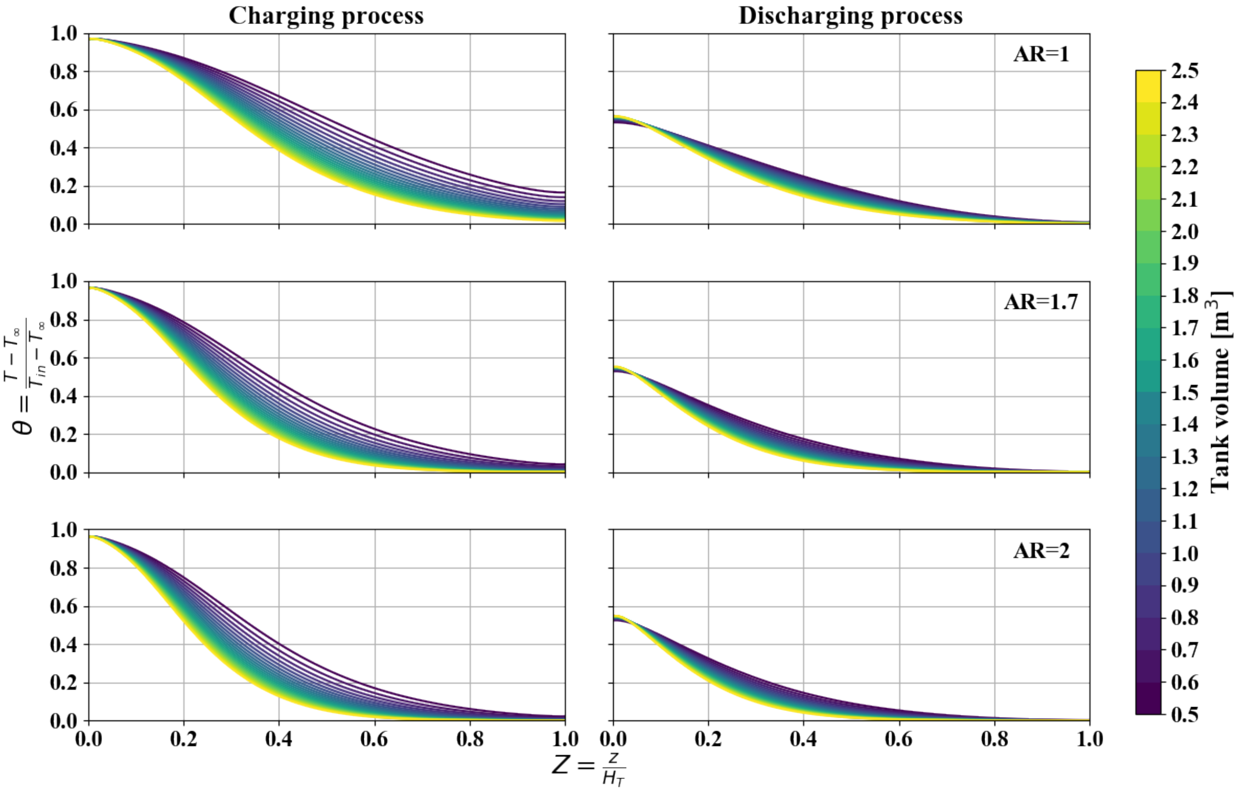

Figure 3.10: Dimensionless temperature distribution at the end of the third charge/discharge cycle for the ES-N slag.

3.5.2 Round-trip efficiency

Aiming to assess the impact of the storage configuration on the round-trip efficiency, four scenarios were outlined in Figure 3.11, assessing two aspect ratios and two sizes for the tank, and all the slags analyzed herein. It is observed that a similar behavior is developed in all the scenarios, in terms of the variations on the round-trip efficiency. It is worth mentioning that the SP slag reached the highest values at the end of the cycle, due to the higher temperatures achieved. Moreover, it is noted that the copper slag ES-N presents similar values than the material reported in [19]. The specific energy per unit of volume charged in a storage filled with the ES-A slag is higher than the other materials due to the larger thermal capacity obtained in the characterization of the slags. That difference is even more significant at the lowest aspect ratio and tank volume, due to the lower temperatures reached at the bottom of the storage, compared to the temperatures observed for the other slags (Figure 3.9a).

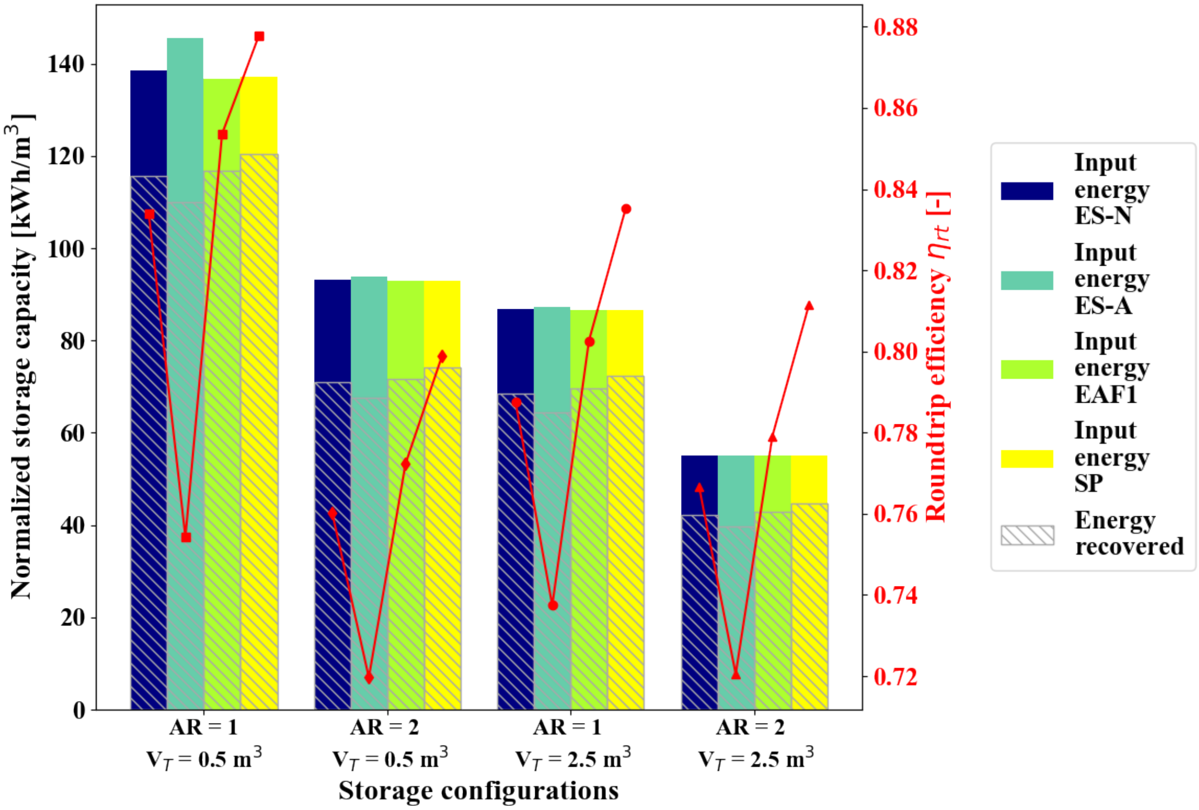

Figure 3.11: Round-trip efficiency after 3 cycles for different storage and materials.

Regarding the effect of the tank volume in η_{rt}, it is observed in Figure 3.11 that at $AR = 1$ the round-trip efficiency decreases as the volume increases, but when the aspect ratio increases to $AR = 2$, such behavior is extremely different. In order to better describe such effect, Figure 3.12 shows in deeper detail the round-trip efficiency variations for the ES-N copper slag. According to Figure 3.12 it is noticed that as the volume of the tank increases, the round-trip efficiency reaches an asymptotic value, while an aspect ratio of 1.4 and higher, a minimum value of the round-trip efficiency can be recognized before reaching such asymptotic behavior. For a fixed value of G, and increasing in the diameter of the tank, the mass flow rate rises as well. Nevertheless, the variation of the volume for a given value of the aspect ratio has a higher impact due to the storage height, rather than to its diameter. Since there would not be significant changes in the air velocity, we can suggest the existence of a stagnation in the thermal front inside of the tank and, consequently, a better differentiation between the hot and cold zones.

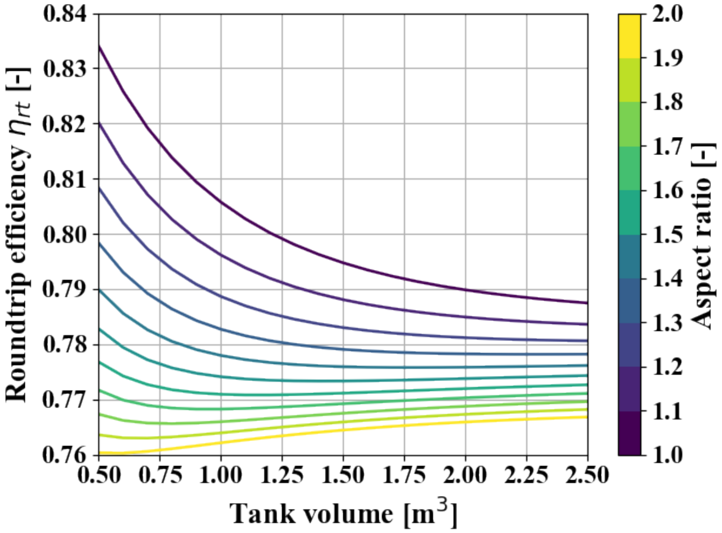

Figure 3.12: Round-trip efficiency as a function of tank volume and aspect ratio after 3 cycles for the sample ES-N.

3.5.3 Exergy efficiency and energy density

For all the simulations executed in the context of the parametric analysis, the exergy efficiency and the energy density of the tank were assessed. The parametric plot presented in Figure 3.13 shows the results obtained for all the materials studied herein, where several phenomena are recognized. The data regarding the energy density and exergy efficiency is plotted for each tank simulated according to the geometric features defined by the duple (AR ,V_T). The shaded areas represent each material assessed in the present work. The dashed lines are curves obtained for a fixed aspect ratio when it is analyzed from right to left, the storage volume increases. The color scale indicates the direction where the aspect ratio grows and the solid line represents a fixed volume. A detailed analysis of the Figure 3.13 enables the identification of several design issues of packed bed storage systems. First, when increasing volume and the aspect ratio, the amount of energy density of the storage tank decreases and that can be explained by the same arguments used on section 3.5.1. In a better stratified tank, the differences between the initial and final states in the temperature profile during the charging cycles become progressively smaller, then the stored energy during that charging period decreases as well. The exergy efficiency shows a different response at fixed aspect ratios. As the storage volumes increases, the stratification of the thermal profile is steeper (Figure 3.10) and during the discharge process, higher temperatures of air at the outlet can be recovered. Moreover, the exergy expelled to the environment at the bottom of the tank during the charge decreases due to the closeness to the reference temperature, as it is shown in Figure 3.9. Then, there is more available work to recover from the storage. Meanwhile, at higher aspect ratio values, for a given tank volume, the exergy efficiency is smaller as a consequence of a reduction on the tank diameter, since the amount of energy stored and the work potential that can be recovered from it in a reduced cross section is also small. Nonetheless, as mentioned above, the increase of the aspect ratio plays an important role in the stratification of the thermal profile as well, but with flattened geometries, the temperature difference between the top and bottom of the packed-bed is lower than for slim geometries;

hence, the air extracts exergy from a source with a higher temperature and as a consequence, with a superior work potential, improving the exergetic efficiency for low aspect ratios.

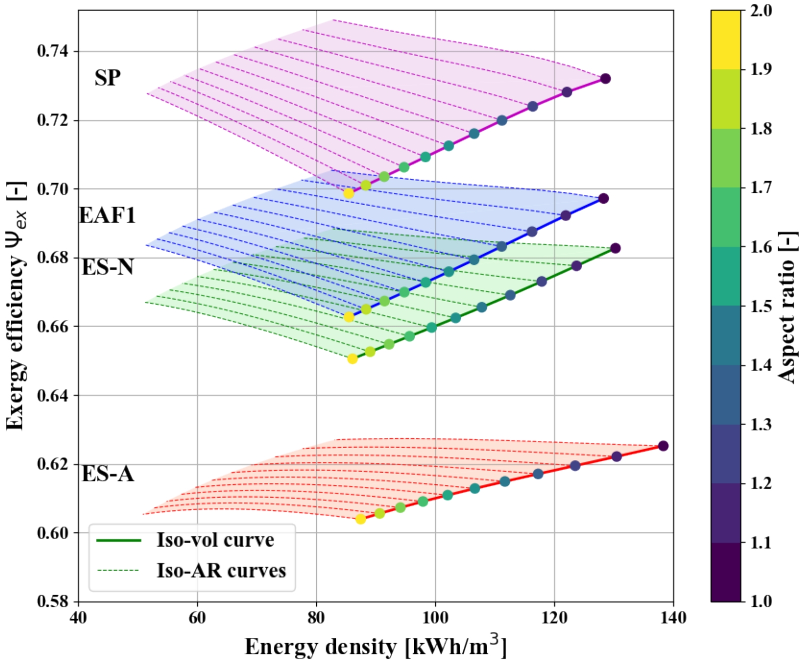

Figure 3.13: Exergy efficiency vs Energy density for all storage scenarios.

For each material assessed in Figure 3.13, Iso-volume curves are determined at $V_T = 0.5\,\mathrm{m}^3$. As an example, the depicted Iso-volume curve for the slag ES-N shows that for an increase of 2.5% of the exergy efficiency, the energy density grows approximately 50% if the aspect ratio is reduced from 2 to 1.2. Thus, the plots in Figure 3.13 show the best configurations that can be achieved considering the material employed and the geometry distribution.

To describe the differences observed during the operation of the packed-bed, when using different slags as filler materials, the combination $AR = 1$ and $V_T = 0.5\,\mathrm{m}^3$ is used for evaluating the change on the exergy flows, as depicted in Figure 3.14. It includes an instantaneous exergy efficiency, which is determined in the same way as the exergy efficiency (Equation 3.20) except that the exergy values are evaluated instantaneously. It is observed that the exergy delivered at the outlet of the tank during the charging process, increases in time when materials with low thermal capacity are employed. In contrast, using a slag with high thermal capacity, as the ES-A, leads to lower temperatures at the bottom of the tank, as shown in Figure 3.9. Hence, the exergy delivered at the outlet is smaller due to the closeness to the reference temperature. The analysis of the curves' behavior at the end of the discharging period shows that a large exergy recovered rate can be reached using the ES-A, constituting a promising option for power generation processes where consecutive cycles of operation can be expected. A material with a higher value of c_p shows a better stratification during the charge/discharge process and a higher exergy output during long discharge operation periods. Regarding the evolution of the exergy efficiency in time, all the materials assessed reach similar values at the end of the process, but in early stages of recovering exergy, the storage filled with slag P (SP) has superior values for both recovered exergy and instantaneous exergy efficiency as a consequence of the higher temperatures reached within the tank at the end of the charging period.

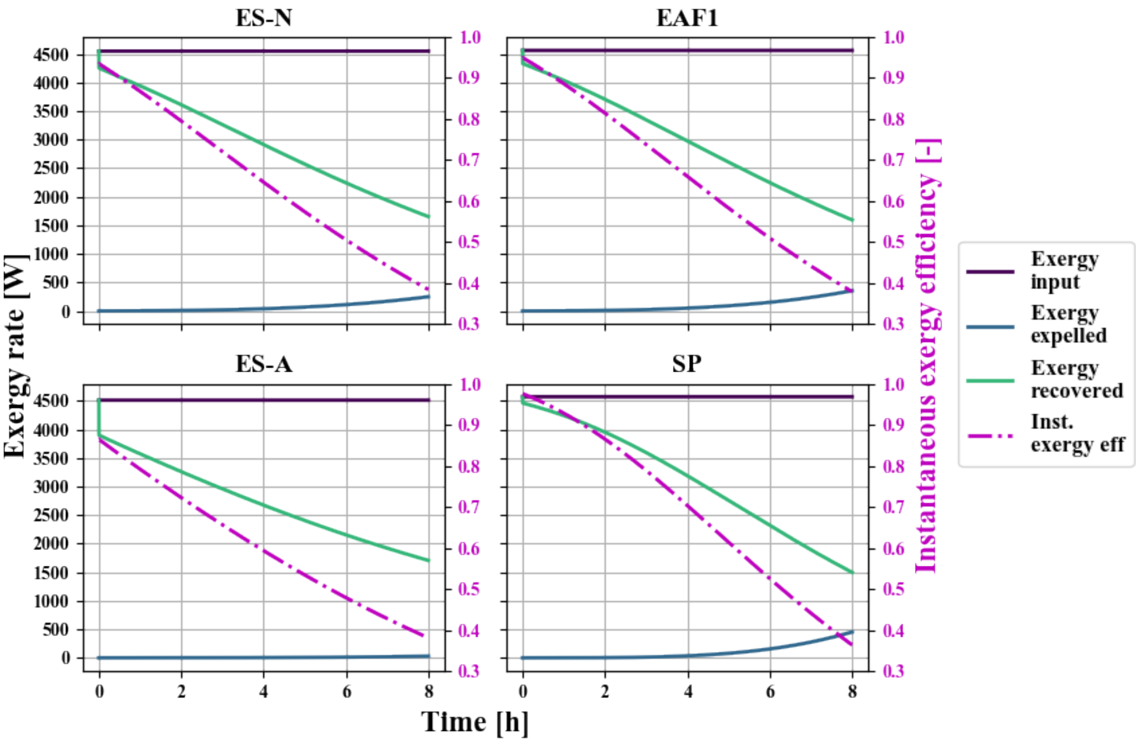

Figure 3.14: Exergy rates for different materials for a tank with $AR = 1$ and $V_T = 0.5\ m^3$.

3.6 Conclusions

The present work analyzes the use of an industrial byproduct, copper slags, as a storage material candidate for high temperature storage in packed-bed systems. Several tests were performed to characterize the thermo physical properties of copper slags samples from two different foundries: ES-N ($c_p = 0.7 - 1.1$ J/(g K), $k = 1.6$ W/(m K), $\rho = 3500$ kg/m^3) and ES-A ($c_p = 1.4 - 1.5$ J/(g K), $k = 2.1$ W/(m K), $\rho = 3700$ kg/m^3). Furthermore, the results from the TGA analysis validate the thermal stability of the copper slags at temperatures up to 800 °C, being suitable for use in high temperature applications, such as power generation in CSP.

Using the measured properties, a 1D thermal model was developed for a cylindrical packed-bed storage using the slags as filling material and air as the heat transfer fluid. Through a parametric analysis, it is shown that the high thermal capacity of copper slags 1.4 - 1.5 J/(g K) (ES-A) compared to 0.6 - 1.2 J/(g K) (SP) allows the development of a steeper thermocline, inducing a better stratification. Moreover, high thermal capacity materials keep a low rate of exergy loss at the storage's outlet, improving the exergy efficiency of the system during long-term operation cycles, which is the case of CSP plants.

This study shows that the initial assessment of copper slags' use as filler material in packed-bed systems is promising because of their high thermal capacity (1.4 - 1.5 J/(g K)). Nonetheless, the tests conducted were limited to the temperature range allowed by the equipment, up to 500 °C. That temperature level makes the material a competitor of molten salts applications, or even as a potential filler material combined to molten salts tanks. Further research could perform new tests at higher temperatures to determine the temperature limit for operating with copper slags and to characterize the full potential of this byproduct as storage material.

Chapter 4

Comparative and parametric study on packed-bed flow topologies for high-temperature thermal energy storage

Packed-bed thermal energy storage is a current trend aiming to improve the performance of renewable power generation, due to the high temperatures that they can achieve and the low operating costs. Experimental studies have demonstrated their feasibility of implementation under conventional storage concepts like vertical cylinder or truncated cone shape; however, the technology is still in a development stage. The present work assesses the performance of four different packed-bed topologies, including the novel radial flow packed-bed concept. Through a cyclic operation study and a parametric analysis, a detailed characterization of their thermal losses, round-trip efficiency, and irreversibilities is conducted. Main findings indicate that radial flow concept reduces the thermal losses by 80% compared to conventional packed-bed configurations. In addition its performance is less sensitive to changes in geometric dimensions, with variations up to 12% against a 58% of variation in a truncated cone shape TES, which enables the radial flow TES to be a promising candidate for high-temperature thermal storage systems.

4.1 Introduction

Thermal energy storage (TES) systems have become a promising alternative to address the mismatch between energy demand and the availability of renewable resources [3]. Their implementation allows a flexible supply of thermal energy and/or electricity, as well as a significant reduction regarding congestion issues on the grid. In general, TES systems are stand-alone components, which allow coupling to any thermal source, such as solar thermal systems, geothermal plants, waste heat from industrial processes, and cogeneration plants [223]. Depending on the application, different storage methods can be used: sensible heat storage (SHS), latent heat storage (LHS), and thermo-chemical storage (TCS) [223, 224], which also present different levels of performance, costs, and energy density. For instance, SHS presents thermal efficiencies within the range of 50-90 % and costs of 0.1-10 €/kWh, while the efficiencies for LHS and TCS may vary between 75-90 % and 75-100 %, but their costs range between 10-50 €/kWh and 8-100 €/kWh [224], respectively. Consequently, sensible TES is an inexpensive alternative compared to LHS and TCS, and it can be applied in a wide range of operating temperatures; however, the storage container requires effective thermal insulation and it can be an important part in the system's costs [224].

The most common application of SHS is in water tanks to supply heat for industrial or district water heating/cooling processes [225]. In renewable power generation, SHS using molten salts has been proven as a commercially viable alternative for concentrating solar power plants (CSP). Indeed, by the end of 2019, approximately a total capacity of 21 GW h of TES were operating coupled to CSP plants [226], where 95 % corresponds to molten salts technology. Nevertheless, an important disadvantage of SHS systems is their low energy density, compared to latent heat and thermochemical storage methods [227]. Moreover, the operating temperatures are constrained to the range of thermal stability of the storage medium, requiring additional control strategies that can increase significantly the capital costs of the technology. Due to such drawbacks, the scientific community has focused on researching new materials and methods for storing sensible heat, aiming to improve the efficiency and reduce the operational costs of thermal systems. In that context, one alternative is to use a solid heat storage medium, such as rocks or waste materials arranged in a packed-bed system.

4.1.1 Packed-bed TES systems

Recent researches have pointed out packed-bed storage systems as a promising SHS option to be coupled with renewable thermal energy sources [224, 223, 17, 20]. The packed-bed TES concept consists in using solids as a storage media that is in direct contact with a heat transfer fluid (HTF) to convey heat [24]. The storage process is carried out through a charging period, where the hot HTF transfers thermal energy to the solid phase; as a result, the temperature of the medium rises, storing sensible heat. Afterwards, the thermal energy is recovered during the discharge process where low temperature HTF flows through the storage domain and the solid phase transfers the accumulated heat to the working fluid.

Figure 4.1 illustrates the behavior of a packed-bed system during its cyclic operation, showing the temperature distribution within the storage domain as the heat transfer occurs. During the charging process, the hot fluid inlets the system at the high temperature zone (see Figure 4.1), whereas the discharging process considers the inlet of the fluid from the low temperature zone. Consequently, no mixing is developed during charging/discharging periods [223]; thus, both regions remain separated by a thermal gradient called "thermocline" [228]. The latter effect corresponds to a constructive advantage since the natural stratification of the storage medium allows using single-tank systems for packed-bed TES, which can reduce capital costs comparing with molten salt TES systems, which are based in two-tank schemes. Another important feature is that packed-bed TES enables the use of a wide variety of storage materials such as natural rocks, ceramics, and waste materials. In fact, important scientific efforts have been devoted to the study of industrial byproducts as a storage medium, considering its high stability at temperatures up to 650 °C and chemically compatible with most of HTF currently employed in commercial plants [17].

Packed-bed systems can be implemented as thermal storage in a wide range of applications according to the operating temperatures. For instance, for low temperature storage,

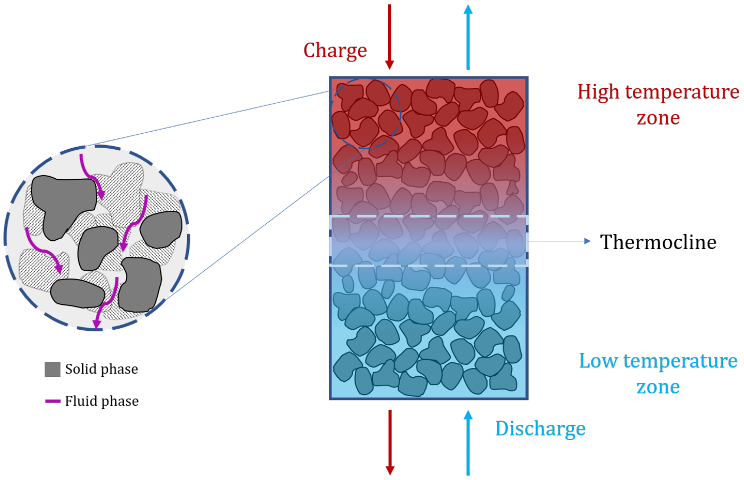

Figure 4.1: Packed-bed TES operating principle.

packed-bed is currently used in residential or greenhouse heating/cooling processes [223, 20]. Whereas, for high temperature processes, they have been analyzed as an alternative for CSP plants [20], since packed-bed systems allow eliminating the temperature constraints associated with molten salts. Thus, packed-bed storage systems allow increasing the operating temperature and achieving higher conversion efficiency by using high temperature power cycles. In that context, several studies have proposed the use of packed-bed systems with compressible gases such as sCO_2 or atmospheric air as working fluid [16, 25, 148, 229, 230]. Furthermore, according to Agalit et al., employing industrial byproducts and air as HTF, reduces the estimated capital costs by 35 % below molten salts systems [17]. Recently, packed-bed technologies has also been studied for compressed air energy storage (CAES) and the so-called Carnot batteries, such as Brayton PTES (Pumped Thermal Energy Storage) [231, 232]. Benato and Stoppato developed an economical analysis of a Carnot battery using packed-bed TES, concluding that despite the poor round-trip efficiency, the system can compete with CAES and Pumped Hydro Storage in terms of energy density and specific costs [233].

Despite the technical and economical benefits of using packed-bed TES systems using air as a HTF, a crucial issue is the large mass flow rate and surface area required, due to the low volumetric heat capacity and thermal conductivity of air [16]. As a consequence, a significant increase in pressure drop and thermal losses are observed. The above is caused mainly by perturbations in the velocity profile observed close to the storage walls and solids placed nearby, which constitutes a key issue especially for small-scale tanks, due to the tank-to-particle diameter ratio [16]. This effect increases the concern to address these challenges through an appropriate design, sizing, and rating of packed-bed TES systems.

4.1.2 Analysis of packed-bed storage topologies

Considering the large variety of applications for packed-bed TES, as well as the aforementioned potential drawbacks, it is crucial to analyze in deep the influence of the key design variables. For instance, regarding the storage materials, industrial byproducts have introduced a broad portfolio of potential candidates, allowing the system to operate at different performance levels depending on the thermophysical properties of the material [234]. On the other hand, the packed-bed topology significantly changes the flow structure within the packed-bed, playing a crucial role in the system's performance. Thus, important research efforts have been devoted to improve current concepts in packed-bed systems by analyzing new design topologies (geometries).

Most packed-bed designs and pilot plants rely on a cylindrical storage tank with axial fluid flow. This topology is considered as a viable choice because it develops a clear thermal stratification for a considerable number of charge/discharge cycles, and a uniform flow distribution across the packed-bed. This geometry has been extensively studied numerically and experimentally, validating a number of heat transfer and pressure drop correlations [16, 42, 130]. Among the axial-based packed-bed TES systems, a truncated cone shape has been also proposed aiming to reduce thermomechanical stresses in the storage structure. Similar to cylindrical TES, there are pilot-scale [25] and industrial scale experimental facilities [27]. The state-of-the-art concepts and topologies for packed-bed systems are discussed extensively in [235].

To improve the operational features of the cylindrical and truncated cone TES systems, several parametric and comparative studies have been carried out to analyze the influence of their operating parameters on the system's performance. For instance, Hänchen et al. developed a parametric study considering a cylindrical TES with axial flow, varying the storage dimensions, mass flow rate, particle diameter, and storage material. The authors aimed to evaluate its cyclic behavior by computing the round-trip efficiency and capacity ratio [16]. The effect of the aspect ratio, storage dimensions, and material employed were studied in [234] using 1^{st} and 2^{nd} law approach for an axial flow cylindrical TES. Regarding comparative studies between different storage domains, Ortega-Fernández et al. assessed three packed-bed TES geometries with axial fluid flow: a cylindrical, regular cone (larger diameter at the top), and inverse cone (larger diameter at the bottom). The study concluded that cylindrical storage presents a better thermal performance than conical structures, and the use of the latter should be only be considered to reduce mechanical stresses [31].

In contrast to the available literature for axial flow structures, few studies have been developed for radial flow packed-bed TES, which are based on the concept illustrated in Figure 4.2d [235, 236]. It is composed of a rock pile enclosed by two perforated concentric pipes with different diameters. During the charging process, the HTF flows through the bed of rock in the radial direction from the inner pipe to the external pipe, reaching the outer plenum and exiting from the bottom of the structure; then, the fluid returns inward during the discharge process.

McTigue and White performed a comparative study between radial and axial flow packed-bed in a cylindrical domain for cold storage applications. Through a thermal model, a 2^{nd} law analysis, and a thermo-economic optimisation, it was determined that radial flow TES exhibits lower pressure drops and a competitive round-trip efficiency compared to axial flow TES [236]. Trevisan et al. proposed an initial design for a radial flow packed-bed TES for high-temperature applications and compared its performance with an axial flow TES after a single charge-discharge cycle. Due to the development of the thermocline in the radial flow packed-bed, this concept has a self-insulating capacity, which reduces its thermal loss to the environment by 46%, compared to the axial flow TES [235]. Both studies do not include a detailed analysis regarding the cyclic performance of radial flow TES, and a comparison with truncated cone shape geometries.

The present study reports a comparative study between the different high temperature packed-bed storage topologies reported in the literature, including the radial flow packed-bed concept. One of the main contributions of the analysis reported herein is the characterization of the cyclic behavior of the radial flow TES in terms of thermal performance and entropy generation. Another important contribution reported is the parametric analysis in terms of the storage dimensions, which enable comparing all the domains and determining the best design considerations for the radial flow thermal storage concept, allowing to improve its efficiency and reduce the thermal losses. Hence, the analysis described in the present article contributes to the available information related to radial flow packed-bed, and extends the application of the preliminar schemes proposed by [235, 236]. Finally, the analysis was carried out considering an industrial by-product as a storage media, copper slag from a Chilean foundry, which is also a novel waste material recently characterized in [234].

The present article is structured for facilitating the description of the analytical model for assessing the performance of the packed-bed topologies (section 4.2). The storage schemes are modelled through a 2-phase heat transfer approach, whereas the thermal losses and entropy generation mechanisms are characterized in depth (section 4.2.1 and subsection 4.2.3, respectively). The numerical results are presented in section 4.3, where the cyclic behavior of the systems is compared in terms of the temperature profiles, thermal losses, and destroyed exergy (subsection 4.3.1). Finally, the study concludes with a parametric analysis performed in terms of the main dimensions of the storage domain, allowing to compare 1^{st} and 2^{nd} law indicators for different storage sizes (subsection 4.3.2).

4.2 Mathematical model

The mathematical model considers a packed-bed structure composed of copper slag pebbles. The potential of copper slag as storage material was initially assessed in [234], showing important advantages for operating temperatures up to 650 °C and using air as HTF. In order to compare different storage configurations, a mathematical model is proposed for describing the behavior of the system, which is solved through numerical methods. The geometric domains analyzed herein consider the most common topologies reported in the literature: cylindrical axial flow tank, a conical tank, an inverse conical tank, and a cylindrical radial flow tank, as shown in Figure 4.2. The arrows in the diagram represent the fluid flow direction during the charging process. In the axial flow structures (see Figure 4.2a, 4.2b and 4.2c) during the charge process the HTF flows from the top down to the bottom of the TES system. During discharge the flow is reverted and it exits from the top at high temperature. In the radial flow configuration (Figure 4.2d), during charge, the HTF enters the inner pipe and it flows radially outward exiting from the outer plenum. During the discharge phase, the flow is reverted and the HTF enters the packed bed from the annulus, moves radially inward, and exits from the inner pipe.

Among the topologies analyzed, several assumptions are considered for the 1D thermal model: (i) No internal heat generation within the tank; (ii) the packed-bed of rock is simplified as an arrangement of mono-sized spheres and characterized by an averaged particle diameter

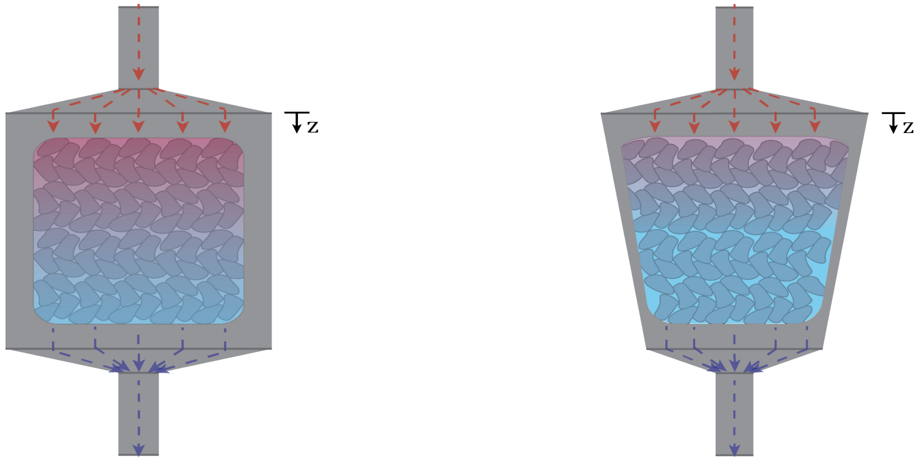

(a) Cylindrical tank with axial flow

(b) Conical tank with axial flow (A)

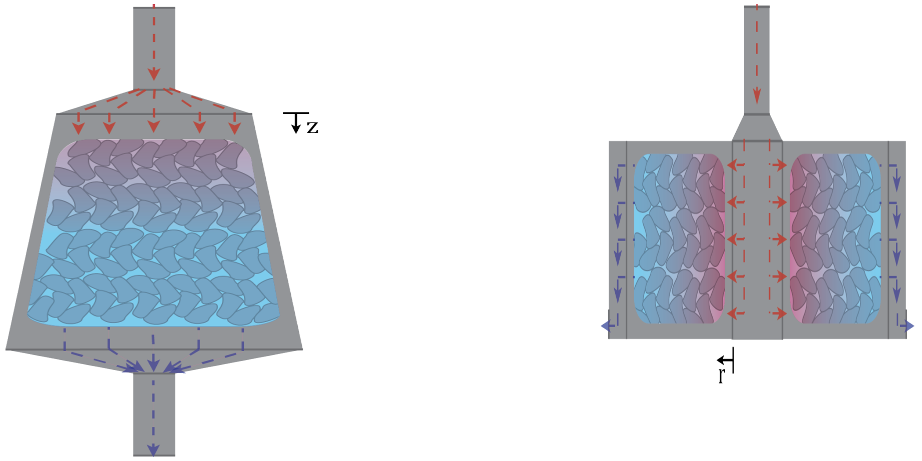

(c) Conical tank with axial flow (B)

(d) Cylindrical tank with radial flow

Figure 4.2: Packed-bed storage configurations.

d; (iii) uniform temperature of the particles, (iv) no thermal gradient in the insulation wall and (v) one-dimensional fluid flow. Due to the latter, the mass continuity equation can be solved for all geometric domains by neglecting the mass accumulation of the fluid within the tank. Thus, it can be deduced that $\dot{m}_{\mathrm{in}} = \dot{m}_{out} = \dot{m}$, where the subscripts *in* and *out* refers to the inlet and outlet of the control volume, and $\dot{m}$ refers to the mass flow rate. As a result, the mass flux G is calculated as $G = \dot{m}/A$. Depending on the configuration analyzed, the cross-sectional area A is evaluated as a function of the axial (z) or radial coordinate (r).

The expressions for the cross sectional area (A) are presented in Table 4.1, where D_T is the tank diameter for cylindrical configurations, D_{top} and D_{bot} are the diameters at the top and bottom of the conical tanks, respectively. r_{i} and r_o is the inner and outer radius of the cylindrical tank with radial flow, and H_T is the tank height.

Table 4.1: Relationship between cross-sectional area and geometric coordinate

Geometry	Cross-sectional area m^2	Range
Cyl. TES w/axial flow	$A = \frac{\pi}{4} D_T^2$	$z \in [0\,,\ H_T]$
Con. TES w/axial flow	$D(z) = D_{top} + (D_{bot} - D_{top})\,\frac{z}{H_T}$ $A(z) = \frac{\pi}{4} D(z)^2$	$z \in [0\,,\ H_T]$
Cyl. TES w/radial flow	$A(r) = 2\pi H_T r$	$r \in [r_\mathrm{i}\,,\ r_o]$

4.2.1 Heat transfer modeling

Aiming to characterize the charging and discharging processes for each domain, a heat transfer model is proposed and solved through numerical methods. The thermal model of the packed-bed system is based on the model developed by Littman et al. [137], which is an extended version of Schumann's model [135] since it considers thermal diffusion in the fluid phase as well [137]. These model was described and validated in a previous study of our group [234], and it consists in a one-dimensional energy balance for the fluid and solid phases. The general formulation is presented in Equation 4.1 and 4.2:

$$\varepsilon\,(\rho c_p)_f \left(\frac{\partial T_f}{\partial t} + u \cdot \nabla T_f\right) = \nabla \cdot (k_{\mathrm{e}ff,f} \nabla T_f) + h_v\,(T_s - T_f) + U_w a_w\,(T_0 - T_f) \tag{4.1}$$

$$(1-\varepsilon)\,(\rho c_p)_s \frac{\partial T_s}{\partial t} = \nabla \cdot (k_{\mathrm{e}ff,s} \nabla T_s) + h_v\,(T_f - T_s) \tag{4.2}$$

where the subscripts f, s and 0 refer to the fluid phase, solid phase, and the reference state, respectively. ε is the void fraction of the porous structure, u the mean velocity of the fluid inside the packed-bed, ρ the density of the phase and c_p its specific heat. The conductive heat transfer is modeled by an effective thermal conductivity $k_{\mathrm{e}ff}$, and a volumetric heat transfer coefficient h_v is employed for describing the convection between the phases. Because of the higher contact area a_w between the fluid and storage walls, thermal losses to the surroundings are assumed only in the fluid's energy balance and modelled considering an overall heat transfer coefficient U_w.

To model the thermal interaction between the particles and the HTF, several heat transfer correlations have been reported in the literature for different operating conditions of the packed-bed. In these systems, the energy can be transferred through: (i) Forced convection between the solid and fluid phase, (ii) conduction due to stagnant fluid in the voids, (iii) conduction through the contact area of the particles and (iv) radiation from the solid phase. Nevertheless, in the present study the radiation heat transfer is neglected since the domains are analyzed at temperature levels up to 650 °C and according to Calderón-Vásquez et al., the thermal radiation becomes relevant for temperatures higher than 750 °C [228]. On the other hand, thermal conduction is modeled through an axial effective thermal conductivity ($k^a_{\mathrm{e}ff}$), which depends on the motionless stagnant conductivity ($k^0_{\mathrm{e}ff}$) and the flow regime

[85]. The expression employed for k^a_{eff} is the proposed by Yagi and Kunii and presented in Equation 4.3 [123].

$$k^a_{\mathrm{e}ff} = k^0_{\mathrm{e}ff} + k_f \alpha_a \,\mathrm{Re}\,\mathrm{Pr} \tag{4.3}$$

where k_f is the thermal conductivity of the fluid, Re is the Reynolds number and Pr is the Prandtl number. α_a is an experimental constant and is assumed to be 0.7 based on Yagi's experiment [123]. The term k^0_{eff} is calculated through the correlation proposed by Hadley [90]. Finally, the effective thermal conductivity of the fluid and solid phase $k_{eff,f}$ and $k_{eff,s}$ are determined from Equation 4.4 and 4.5 [50].

$$k_{\mathrm{e}ff,f} = 0.5\,\mathrm{Re}\,\mathrm{Pr}\,k_f \tag{4.4}$$

$$k_{\mathrm{e}ff,s} = k^a_{\mathrm{e}ff} - k_{\mathrm{e}ff,f} \tag{4.5}$$

The convection between the phases is modeled through the volumetric heat transfer coefficient h_v with an empirical correlation, whose selection is based on its use in experimental setups and the operational range where it is valid. To date, there are not experimental studies for radial flow packed-bed TES to study the validity of h_v correlations proposed in the literature for conventional packed-bed topologies. On the other hand, the correlation proposed by Coutier and Farber has been employed and validated for both cylindrical and truncated-cone shapes [16, 42, 27]. The correlation is expressed in Equation 4.6 and their values are valid for $1 \leq G/\mathrm{d} \leq 500$ kg/(m^3 s) [42].

$$h_v = 700 \left(\frac{G}{\mathrm{d}}\right)^{0.76} \tag{4.6}$$

Finally, the model satisfies the following boundary conditions: (i) Thermal equilibrium in the fluid phase at the storage's outlet: $\left.\frac{\partial T_f}{\partial \xi}\right|_{\xi_{out}} = 0$, (ii) thermal equilibrium in the solid phase at the inlet and outlet: $\left.\frac{\partial T_s}{\partial \xi}\right|_{\xi_{in}} = \left.\frac{\partial T_s}{\partial \xi}\right|_{\xi_{out}} = 0$. ξ is the radial or axial coordinate, depending on the geometry analyzed. The initial condition for both phases considers the temperature profiles obtained at the end of the previous process, and for the first charging process, the initial temperature for both phases is the reference temperature T_0.

Thermal losses

Thermal losses through storage walls play an important role in the heat transfer balance since they are directly in contact with the solid and fluid phase. Modeling the thermal losses strongly depends on the geometric domain, therefore a detailed analysis was carried out to compare the overall thermal losses through the surfaces of a packed-bed TES: top cover, bottom cover, and lateral cover (identified by the subscripts *top*, *bot*, and *lat*). During the operation of the storage tank, the internal surfaces are subject to forced convection due to the high-temperature air flow, while the external surfaces are exposed to natural convection because of the temperature differences between the tank and the surrounding air. The Nusselt number for the convection inside the tank (Nu_{int}) is modelled as suggested in [124]:

$$\mathrm{Nu}_{int} = \begin{cases} 0.6\,\mathrm{Pr}^{1/3}\,\mathrm{Re}^{0.5} & 1 < \mathrm{Re} \leq 40 \\ \mathrm{Pr}^{1/3}\,\mathrm{Re}^{0.8} & 40 < \mathrm{Re} \end{cases} \tag{4.7}$$

The internal convective heat transfer coefficient h_{int} can be determined by the expression proposed in [124]: $h_{int} = \frac{k_f}{\mathrm{d}}\mathrm{Nu}_{int}$. Regarding the radial flow packed-bed TES, the interaction of the fluid with the walls while flowing through the outer plenum must also be considered (see Figure 4.2d). Assuming that the ratio between the outer diameter of the packed-bed ($D_{o,pb}$) and the outer plenum (D_{op}) is close to one ($D_{o,pb}/D_{op} \approx 1$), an approximation of the Nusselt number for fully developed laminar flow in a circular tube annulus can be applied [237]: $\mathrm{Nu}_{int} = 4.86$.

The correlation employed for the Nusselt number to describe natural convection (Nu_{ext}) over a standing wall is the one proposed in [237]:

$$\mathrm{Nu}_{ext} = 0.68 + \frac{0.67\mathrm{Ra}^{1/4}}{\left(1 + \left(\frac{0.492}{\mathrm{Pr}}\right)^{9/16}\right)^{4/9}} \tag{4.8}$$

where Ra is the Rayleigh number. For the cases where the wall is inclined, like the truncated-cone shape, the gravitational acceleration term in the Rayleigh number, is reduced to $g\cos\theta$ [237], with θ being the wall inclination angle. Additionally, for inclination angles between $0° \leq \theta \leq 60°$ and configurations similar to regular cone shape, Equation 4.8 is also valid. For hot inclined plates facing the surroundings, the aforementioned correlation cannot be employed; hence, the expression applied is the one proposed in [238] considering the same correction for the gravitational acceleration term in the Rayleigh number.

$$\mathrm{Nu}_{ext} = 0.508\left(\frac{\mathrm{Ra}}{1 + \frac{0.952}{\mathrm{Pr}}}\right)^{1/4} \tag{4.9}$$

The external natural convection over the top surface of the storage tank can be modelled with the following correlations [237]:

$$\mathrm{Nu}_{ext}^{top} = \begin{cases} 0.54\mathrm{Ra}^{1/4} & 10^4 \leq \mathrm{Ra} \leq 10^7 \\ 0.15\mathrm{Ra}^{1/3} & 10^7 \leq \mathrm{Ra} \leq 10^{11} \end{cases} \tag{4.10}$$

where Nu_{ext}^{top} is the Nusselt number for an upper surface at high temperature. Lastly, the external convective heat transfer coefficient h_{ext} is determined through: $h_{ext} = \frac{k_f}{L}\mathrm{Nu}_{ext}$, and L is the characteristic length. The bottom surface of the TES systems is assumed to be in contact with the floor; therefore, the natural convection term is not included in the thermal losses.

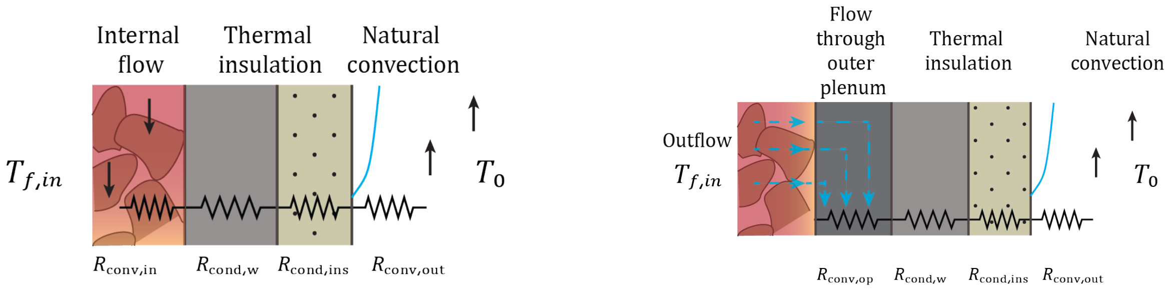

(a) Lateral heat losses in axial flow TES

(b) Lateral heat losses in radial flow TES

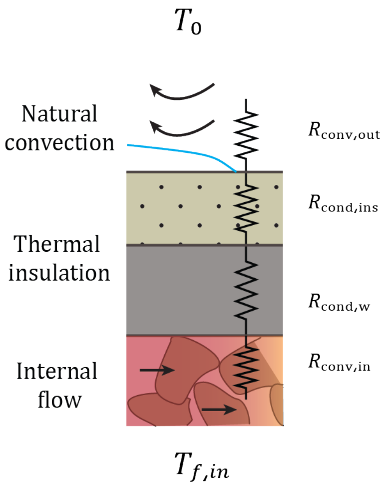

(c) Top cover heat losses in radial flow TES

Figure 4.3: Schematics of the models used for assessing the thermal losses in each storage topology.

Figure 4.3 depicts the modelling approach for the thermal losses in the different direction of the air flow. In all the topologies analyzed, the thermal insulation is considered as composed by a steel layer (storage wall) and a mineral wool layer. For the axial flow packed-bed TES, the top/bottom thermal losses are modelled similarly as described by diagram in Figure 4.3c, yet changing the flow direction. The model neglects the interaction of the internal flows, since the velocity profile of air is modelled as plug-flow. The expressions for the overall heat transfer coefficients can therefore be summarized in Equation 4.11, 4.12, and 4.13.

$$\frac{1}{U_{top}} = \begin{cases} \frac{1}{h_{int}} + \sum\limits_{j=1}^{N} \frac{\delta_j}{\lambda_j} + \frac{1}{h_{out}} & \text{, radial flow TES} \\ \\ \sum\limits_{j=1}^{N} \frac{\delta_j}{\lambda_j} + \frac{1}{h_{out}} & \text{, axial flow TES} \end{cases} \tag{4.11}$$

$$\frac{1}{U_{bot}} = \begin{cases} \frac{1}{h_{int}} + \sum\limits_{j=1}^{N} \frac{\delta_j}{\lambda_j} & \text{, radial flow TES} \\ \\ \sum\limits_{j=1}^{N} \frac{\delta_j}{\lambda_j} & \text{, axial flow TES} \end{cases} \tag{4.12}$$

$$\frac{1}{U_{lat}} = \frac{1}{h_{\text{int}}} + \frac{D_{pb}}{2} \sum_{j=1}^{N} \frac{1}{\lambda_j} \ln \frac{r_{j+1}}{r_j} + \frac{D_{pb}}{h_{\text{ext}} D_{\text{ext}}} \tag{4.13}$$

where δ_j is the width of the j-th insulation layer with its respective thermal conductivity, λ_j. D_{pb} is the packed-bed diameter, which assumes the value of D_T for the cylindrical TES with axial flow, $D(z)$ for the truncated-cone shape TES, and $D_{o,pb}$ for the radial flow TES. Hence, the heat losses through the surface Ω during the charging/discharging process, are calculated using the following expression:

$$Q_{loss,\Omega} = \int\limits_{t_{start}}^{t_{\text{end}}} \left(\int\limits_{\Omega} U \left(T_f(A) - T_0 \right) \mathrm{d}A \right) \mathrm{d}t \tag{4.14}$$

where t_{start} and t_{end} denotes the starting and ending times of the charge/discharge process. A is the area of the surface Ω with overall heat transfer coefficient U.

4.2.2 First-law analysis

The thermal performance of the storage tanks can be characterized through a first-law analysis in terms of the round-trip efficiency, which is defined by the following equation [220].

$$\eta_{rt} = \frac{E_{\mathrm{d}ch}}{E_{ch}} \tag{4.15}$$

where E_{ch} and $E_{\mathrm{d}ch}$ are the energy delivered to the TES system during the charging process and the energy recovered during the discharge, respectively. The energy delivered is calculated through the following expression:

$$E_{ch/\mathrm{d}ch} = \int\limits_{t_{start}}^{t_{\text{end}}} \dot{m} \left(h_{\text{in}} - h_{out} \right) \mathrm{d}t \tag{4.16}$$

where $h_{\rm in}$ is the fluid's enthalpy, evaluated at the inlet temperature of the charging/discharging process, while h_{out} is the enthalpy of the fluid's leaving the packed-bed.

4.2.3 Second-law analysis

During the operation of the TES system, the heat is transferred between the fluid and solid phase during charging and discharging processes. Due to the irreversible nature of the heat transfer mechanisms involved, exergy is destroyed. A second-law analysis allows quantifying the sources of entropy generation. McTigue elaborated a detailed analysis for describing the exergetic losses in a packed-bed systems based on the irreversible processes during heat transfer process [239]. In that context, the following mechanisms are considered in this study: (i) convection heat transfer between the fluid and solid phase, (ii) thermal losses through the storage walls in contact with the thermal front, (iii) conductive heat transfer between the solid particles due to thermal gradients, and (iv) conductive heat transfer in the fluid phase. The expressions for the entropy generation ($\dot{S}_{gen}$) in each process are presented in Equation 4.17, 4.18, and 4.19 (see Bejan [240]).

$$\dot{S}_{gen,conv} = \int h_v A \frac{\left(T_f(\xi) - T_s(\xi)\right)^2}{T_f(\xi) T_s(\xi)} \mathrm{d}\xi \tag{4.17}$$

$$\dot{S}_{gen,cond,j} = \int k_{eff,j} A \left(\frac{1}{T_j(\xi)} \frac{\partial T_j}{\partial \xi} \right)^2 \mathrm{d}\xi \tag{4.18}$$

$$\dot{S}_{gen,loss,\Omega} = \int_{\Omega} U \frac{\left(T_f(\xi) - T_0\right)^2}{T_f(\xi) T_0} \mathrm{d}A \tag{4.19}$$

where the subscripts *conv*, *cond*, and *loss* refers to convection, conduction, and heat loss, respectively. The entropy generation due to heat conduction is defined for the j-th phase, and can be either associated to the fluid or solid phases. Regarding the entropy generation associated to thermal losses, the surface Ω corresponds to region in contact with the thermocline: Lateral walls for axial flow TES, and top and bottom surfaces for radial flow TES. Hence, the exergy destroyed $\Xi_{\rm d}$ by the heat transfer phenomena is calculated through $\Xi_{\rm d} = T_0 \left(\int \dot{S}_{gen} \mathrm{d}t \right)$.

4.2.4 Pressure drop

In general, packed-beds present a good heat transfer capacity due to their large heat transfer surface. The latter also implies an increase in the body forces of the solid medium onto the HTF. Ergun developed an experimental study to characterize the pressure drop through packed-bed columns and proposed an empirical correlation for the shear stress and inertial force coefficients [130]. This empirical correlation has been extensively used to determine pressure drop in axial flow packed-bed topologies, such as cylindrical and cone shape [16, 25, 241]. This empirical correlation is expressed as follows,

$$\nabla P = -\frac{\mu_f}{K}u_D - \frac{C_E}{K^{1/2}}\rho_f u_D^2 \tag{4.20}$$

where u_D is the Darcy's superficial velocity, μ_f and ρ_f the fluid viscosity and density, respectively. K is the permeability term and C_E is an empirical parameter. According to Ergun's study, $K = \left(\mathrm{d}^2\varepsilon^3\right)/\left(150\left(1-\varepsilon\right)^2\right)$ and $C_E = 1.75/(150\varepsilon^3)^{1/2}$ [130], where d is the particle diameter and ε the void fraction.

In order to extend an initial pressure drop analysis for different packed-bed topologies, a steady-state momentum balance is proposed to determine the pressure gradient along the fluid flow direction, which is assessed by the following expression.

$$\nabla P = \mu_f \nabla^2 u - \rho_f u \cdot \nabla u - \frac{\mu_f}{K}u_D - \frac{C_E}{K^{1/2}}\rho_f u_D^2 \tag{4.21}$$

The first and second terms in Equation 4.21 corresponds to the viscous effects and the flow acceleration, respectively. The body force is expressed by the correlation of Ergun in terms of a drag force in the momentum equation. When plug flow is assumed, the first and second terms in Equation 4.21 are zero, resulting in the Ergun's correlation. On the other hand, for topologies with cross-sectional variations, the fluid's velocity (u) along the packed-bed main coordinate also varies, so the first two terms do not cancel in Equation 4.21.

4.3 Results and Discussion

The results presented in this section are based in the simulations obtained from the four topologies aforementioned in Figure 4.2: Cylindrical tank with axial flow, conical tank with axial flow A and B (henceforth regular and inverse cone shape, respectively), and cylindrical tank with radial flow. A detailed comparison is carried out in terms of the cyclic behavior of the packed-bed TES prior to developing a comprehensive parametric analysis of their thermal performance and pressure drop.

4.3.1 Cyclic operation of packed-bed TES

The packed-bed domains are set up in similar geometric dimensions for a first cyclic comparison. The study is designed in terms of equal tank volume, aspect ratio, mass flow rate, charging/discharging period, and operating temperature. Air and copper slag are employed as a HTF and a storage medium, respectively. The thermophysical properties of the slags have been characterized in a previous work [234] for a mean operating temperature within the range of the study; on the other hand, the temperature dependence of the properties is only assumed for the fluid phase.

In Table 4.2 the operating conditions of the comparative study are presented. The aspect ratio is defined as $H_T/\left(r_o - r_\mathrm{i}\right)$ for the radial flow packed-bed, D_T/H_T for cylindrical TES with axial flow, and $\max\left(D\right)/H_T$ for truncated cone shape TES. The selection of the parameters was made aiming to keep $\mathrm{Bi} \approx 0.1$ in all the geometric domains, so that the intraparticle gradient can be neglected.

Table 4.2: Parameters of the cyclic operation study.

Parameter	Value
Charge/discharge temperature $T_{in,ch/\mathrm{d}ch}$	923/298 K
Reference temperature T_0	298 K
Mass flow rate $\dot{m}$	0.08 kg/s
Aspect ratio AR	1
Tank volume V_T	2 m^3
Charge/discharge time	6 h
Number of cycles	10
Particle diameter d	0.02 m

Temperature profiles

From the heat transfer modelling developed in section 4.2, temperature profiles for each storage domain can be obtained. In Figure 4.4, the temperature distribution of the fluid phase within the tank is shown after 10 charge/discharge cycles as a function of the dimensionless coordinate, to compare all geometries. At the end of the 10^{nth} charge cycle, it is observed that the temperature profiles of geometries with axial flow have similar shape, while some differences can be appreciated in the spread of the thermal front, as a result of the thermal losses developed during the charging process. For the radial flow TES, the temperatures reached are greater than the other geometries. The latter can be explained by the reduction of the fluid velocity with the radial position within the bed, since the cross section gets larger. Such effect decreases the convective heat transfer between the fluid and the rock; on the other hand, as the diffusion increases, the temperature profile at the outlet of the storage becomes steeper. When the last discharging process finishes, the remaining temperature profiles exhibit the same differences appreciated for the charging temperature profiles. The temperature delivered at the storage's outlet is the lowest in the inverse cone TES and the radial flow TES, despite having higher temperatures compared to the other domains with axial flow. In both geometries, thermocline is thicker than the regular cone shape and the cylindrical TES with axial flow; therefore, thermocline starts leaving the storage tank after a short period during the discharging process in radial flow TES and inverse cone shape.

Figure 4.5 plots the fluid temperature delivered at the outlet of the TES system during all discharge periods. It should be noted that for the inverse cone shape and radial flow TES, the discharged temperature decreases at a higher rate than the other domains, and that behavior is maintained over the 10 analyzed cycles; hence, the increasing thermocline thickness is critical to keep higher temperatures exiting the storage during the discharging process. From the 5^{th} cycle onwards, the outlet temperature increases between cycles at a slower rate as a result of a thermal equilibrium in the storage tank.

Thermal performance

During the complete operation of the TES system, the thermal losses through the top, bottom, and lateral surfaces were calculated. Figure 4.6 shows the thermal losses classified according to the surface where they occur. The proposed concept of radial flow TES has the lowest levels of overall heat loss due to the self-insulation effect provided by the outer layers

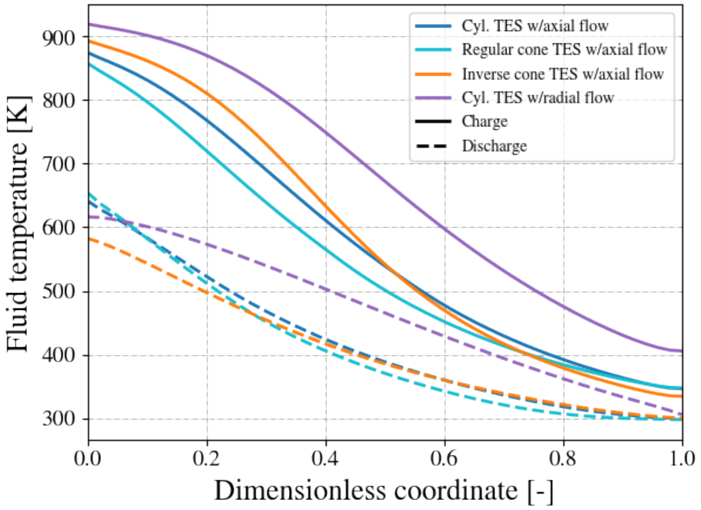

Figure 4.4: Temperature profiles of the fluid at the end of the 10^{nth} cycle.

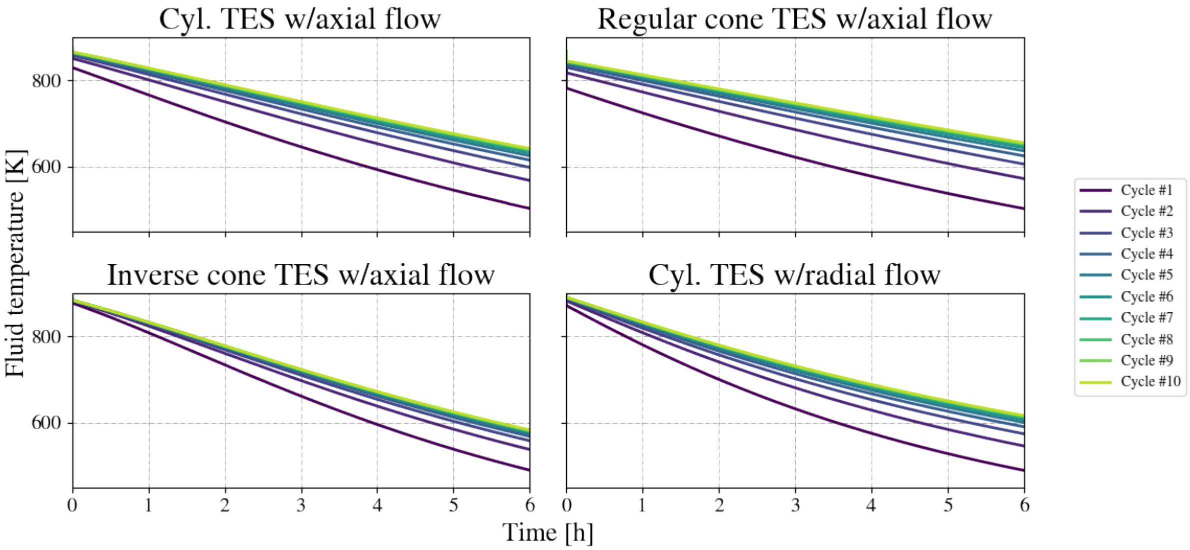

Figure 4.5: Fluid temperature at storage's outlet during discharge process.

of the packed-bed. In addition, Figure 4.4 verifies that the lateral wall of the radial flow TES is in contact with the region at the lowest temperature; conversely, axial flow geometry can exchange a higher amount of heat through that surface, since it is directly in contact with the thermocline. The top surface of the axial flow domain is exposed to the highest temperature in the storage tank, so the thermal loss through that layer is higher than that of the radial TES since the top and bottom of the tank are in contact with the radial thermal profile. The latter explains why the bottom thermal loss is higher in the radial flow TES to the other geometric domains. Regarding the cyclic behavior of the overall thermal losses, while the cycles progress, the losses increase as the temperature levels inside the domain rise. Nevertheless, the difference between cycles also gets smaller as a result of reaching thermal equilibrium during the consecutive charge-discharge cycles.

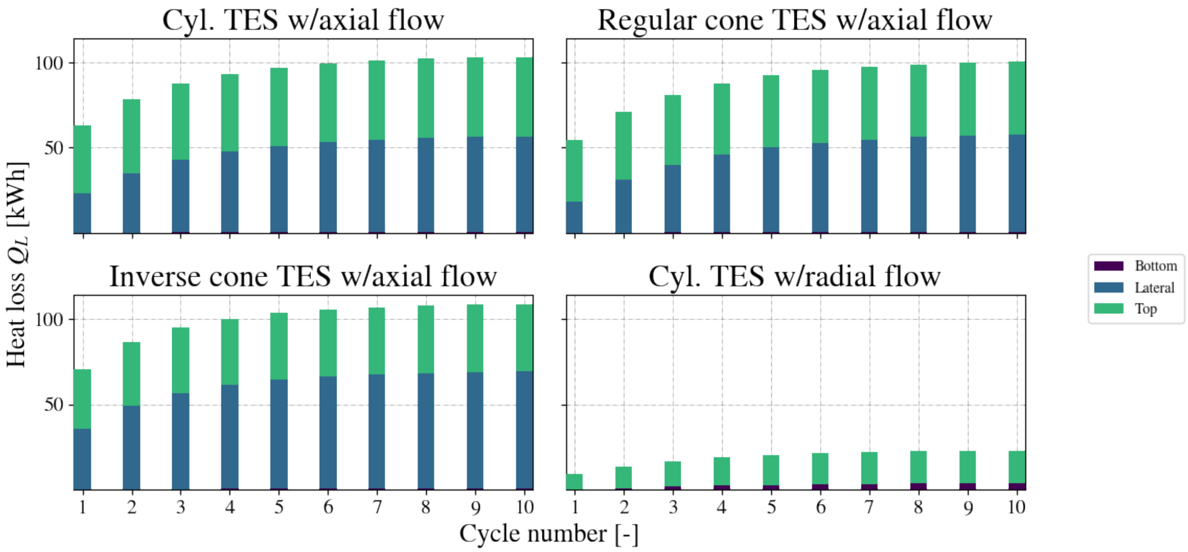

Figure 4.6: Overall thermal losses of the TES in cyclic operation.

Exergetic performance

The total exergy recovered from the TES system is assessed through a second-law analysis. For power generation applications, it is relevant to study the evolution of the recovered exergy during the discharge process to guarantee a proper operation when combined with a power cycle. The transient behavior of the input and recovered exergy of the system is depicted in Figure 4.7. The amount of total input exergy ($\dot{\Xi}_{\text{in}}$) is the lowest in the radial flow TES as a consequence of the higher temperatures reached at the outer layers during the charging period. In terms of recovered exergy during the discharge process, the decreasing rate is strictly related to the temperature delivered at the storage's outlet. Due to irreversibilities developed during the heat transfer process, different behaviors in the recovered exergy are observed; additionally, heat losses through the surface in contact with the thermocline is also involved in the destruction of exergy during charge/discharge processes.

In order to compare the differences in the irreversibilities caused by heat transfer mechanisms and thermal losses, Figure 4.8 is plotted, where the cyclic evolution of three performance indicators are assessed: the round-trip efficiency (η_{rt}), exergy destroyed by convective and conductive heat transfer defined as: $\Xi_{\text{d},HT} = T_0 \left(\int \left(\dot{S}_{gen,conv} + \dot{S}_{gen,cond,s} + \dot{S}_{gen,cond,f} \right) \text{d}t \right)$, and the exergy destroyed by thermal losses through surfaces in contact with the thermocline ($\Xi_{\text{d},L}$). Regarding the behavior of these indicators, for all the domains studied η_{rt} and $\Xi_{\text{d},L}$ increase with the cycle number, since the temperatures reached at the end of the charge-discharge process is higher than the previous one. However, there is a decrease in $\Xi_{\text{d},HT}$ throughout the cycles as a result of a smaller temperature difference between the phases. The radial flow packed-bed at the end of the 10^{nth} corresponds to the domain with the highest round-trip efficiency and exergy destruction due to heat transfer mechanisms, but with the lowest irreversibilities caused by thermal losses. Having a constant supply of energy at

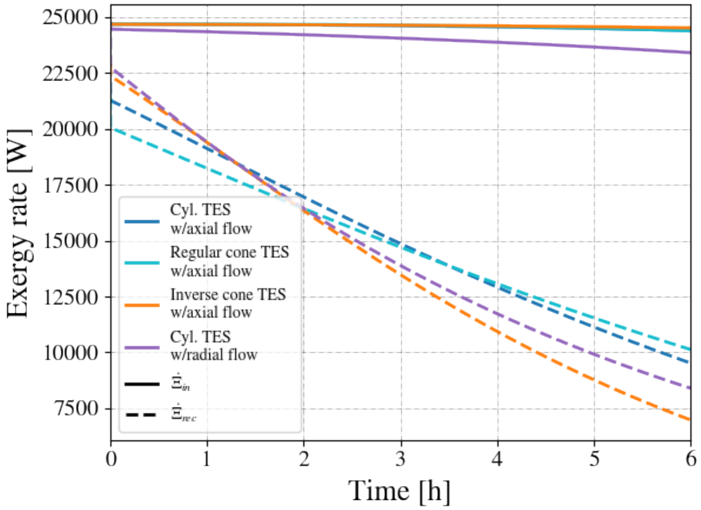

Figure 4.7: Input and recovered exergy as a function of time for all storage domains.

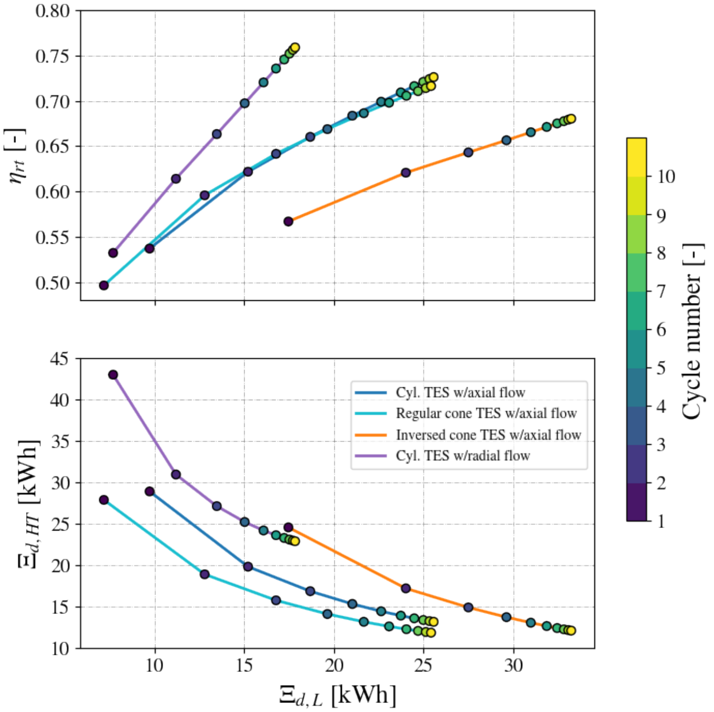

Figure 4.8: Cyclic evolution of round-trip efficiency and exergy destroyed due to heat transfer between the phases, and the exergy destroyed due to thermal loss

high temperatures is important to improve the performance of power generation systems, but the exergy destruction may affect that condition during the discharging period. Axial flow domains such as cylindrical storage and regular cone shape, have similar levels of performance and the differences are mainly caused by the variation in the packed-bed cross-section and the exposed area for thermal losses. Lastly, the inverse cone shape has the highest level of exergy destroyed due to thermal losses, which can have the same impact on the exergetic response of the storage domain as the radial flow TES.

4.3.2 Parametric analysis

A parametric analysis is carried out aiming to compare and assess the 1^{st} and 2^{nd} law behaviors of the packed-bed domains under different geometric conditions, which are determined by varying the tank volume (V_T) and the aspect ratio (AR). A maximum Reynolds number was fixed as well, since the cross-section variations in truncated cone and radial flow TES leads to changes in the velocity profile, so the turbulent regime may be reached within the storage tank. According to Dybbs and Edwards, the turbulence in porous structures appears when $\mathrm{Re} > 300$ [218]; hence, in the present study $\mathrm{Re}_{max} = 100$ for all TES domains, because the condition $\mathrm{Bi} \approx 0.1$ also needs to be fulfilled. As a consequence, an upper limit in the mass flux rate is also fixed, since it can be calculated with the expression: $G_{max} = \mathrm{Re}_{max} \frac{\mu_f}{\mathrm{d}}$; therefore, for topologies with cross-sectional variations, the mass flow rate of air entering the TES is calculated in order to obtain the upper value of G in the smallest cross section.

Table 4.3: Operating conditions considered in parametric study.

Parameter	Value
Aspect ratio AR	from 0.5 to 2
Tank volume V_T	from 2 to 20 m^3
Re_{max}	100
Number of cycles	5
Mass flux range	0.02 - 0.205 $\mathrm{kg/(m^2\,s)}$

The variation of the aspect ratio and the tank volume are presented in Table 4.3 including the operating ranges of the Bi and the mass flux. Operating temperatures, charging/discharging time, and particle diameter are the same as those defined for the cyclic study (see Table 4.2). The results of the parametric analysis are divided into two parts as follows: Part one compares all the storage domain and part two details the geometric on the radial flow TES.

Analysis for all storage tanks

The sensitivity analysis for all storage domains are presented in Figure 4.9 where several features are depicted: The shaded areas represents each storage domain studied. The upper graph consist of a plot of the pressure drop results and the round-trip efficiency for a given pair of (AR , V_T), while the graph at the bottom depicts the pressure drops values as well, but contrasted with the overall thermal losses. The dashed and dotted lines are the cases with the same aspect ratio and tank volume, respectively. Furthermore, the minimum and maximum values of those parameters are colored in the plot and indicated in the legend.

According to the Figure 4.9, there are common responses in the system's performance between the storage domains, which are analyzed as follows: In terms of the general behavior of the pressure drop, for a constant aspect ratio, ΔP increases with the tank volume and that is mainly caused by the increase of the storage height or radial path $r_o - r_\mathrm{i}$ in axial and radial tanks, respectively. On the other hand, the round-trip efficiency decreases as the aspect ratio gets larger for a given tank volume. The above occurs as a result of the higher temperatures reached throughout the storage's length for small aspect ratios since the thermal front takes

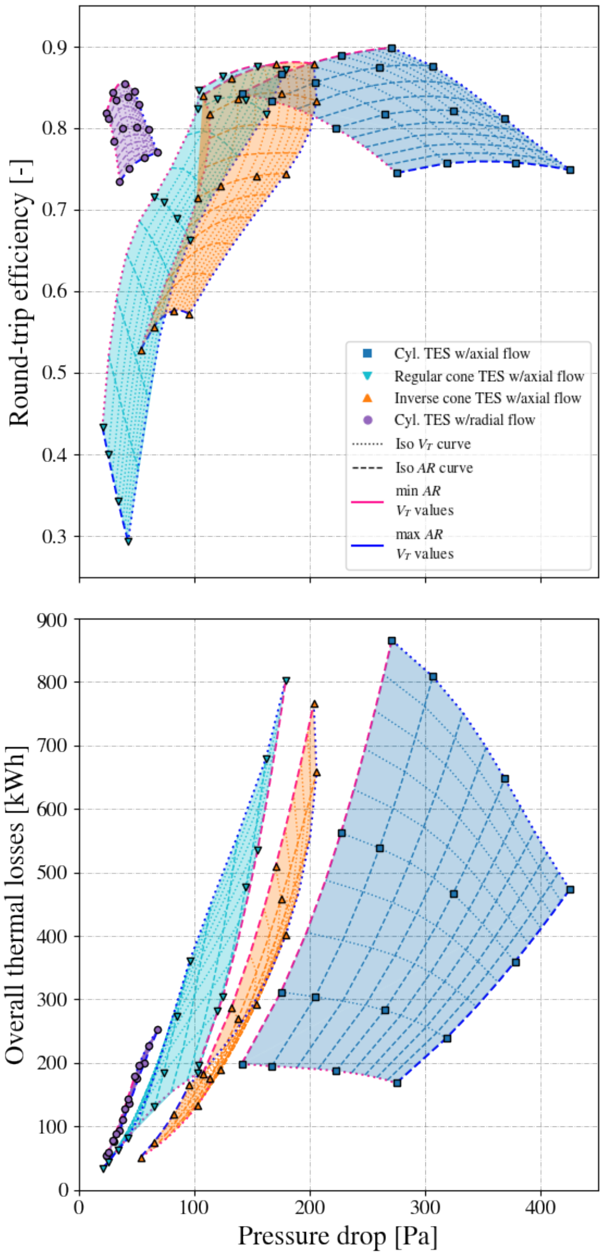

Figure 4.9: Comparison of performance indicators for all storage scenarios: Round-trip efficiency vs pressure drop (top) and overall thermal losses vs pressure drop.

less time to completely circulate along the tank during the charging process, allowing the TES outlet to reach higher temperatures during the charging process and storing a greater amount of sensible heat. Thermal losses exhibits an expected behavior when analyzed for a constant aspect ratio: for larger tank volumes, the overall thermal losses are higher as a result of the larger exposed surfaces.

Considering the effects of the geometric dimensions in cylindrical domains, when the aspect ratio is between 0.5 - 1.3 a parabolic shape of the round-trip efficiency is recognized; thus, for a critical tank volume, a maximum value of η_{rt} is reached. For higher aspect ratios the round-trip efficiency improves with the tank volume until it reaches an asymptotic behavior.

For the design of the parametric study, the calculations of the mass flux rate leads to all the cases studied for the radial flow TES being evaluated with the same inlet/outlet mass flux rate; however, the radial path $r_o - r_\mathrm{i}$ increases with the tank volume as well but with no significant variations in both fluid and thermal front velocity between cases. Due to the above, it appears that there is an stagnation on the thermal front as the volume increases, which may cause differences in the amount of energy stored and recovered. For the axial flow TES, the evolution of the round-trip efficiency with the tank volume is similar to the radial flow TES and that can be justified by the same phenomena previously described, considering that the mass flux rate also remain the same for all tank dimensions assessed. On the other hand, pressure drop increases with the aspect ratio for both storage topologies, as a result of the higher tank lengths. Finally, according to the evolution of the overall thermal losses with the aspect ratio in the axial flow TES, at higher values of AR the overall thermal losses result to be the lowest and that is caused by the temperature profiles developed in high aspect ratios: The temperature gradient becomes steeper for these cases [234], thus the temperatures reached in the "cold zone" of the storage tank is lower than compared to small values of aspect ratios. The geometric effects on the overall thermal losses in the radial flow TES are discussed in depth in section 4.3.2.

For conical tanks, their behavior are noticeable different compared to cylindrical topologies. The inverse cone TES exhibits a similar behavior to radial flow TES in terms of the round-trip efficiency, since they both have divergent topology during charging process and convergent during discharge. Nevertheless, the main difference is the larger variation on the performance that inverse cone has against radial flow TES, and it can be due to the evolution of the void fraction with the axial coordinate. On the other hand, the round-trip efficiency on regular cone TES tends to decay as the tank volume increases as a result on the void fraction and mass flux rate variations: At higher aspect ratios and tank volumes, due to the TES topology the lower zones in the regular cone packed-bed presents the largest void fraction and mass flux rates; therefore, the convective heat transfer is lower in that zone because of the voids and the low temperatures reached, which reduce the amount of energy stored and recovered from the TES. Regarding the pressure drop, an unusual behavior is encountered when the aspect ratio increases. As shown in Figure 4.9, the pressure drops decreases as the conical tank gets larger and it can be caused by the following effects: (i) Higher aspect ratios, allows the conical TES to have a smaller D_{bottom}/D_{top} ratio and higher mass flux rates variations, (ii) Larger void fraction in the zones with smaller tank diameter, allowing the fluid to easily circulate through the packed-bed. The above causes a noticeable change in the drag forces acting on the fluid, compared to the effective path length within the domain.

Comparing all TES topologies, the geometric dimensions affects considerably the thermal performance of the regular cone TES. Conversely, cylindrical TES with axial flow presented the highest pressure drop values in all the cases and the highest variability. That behavior is because of the Re_{max} fixed for the parametric analysis, which is only affected by changes in the thermophysical properties of the fluid; on the contrary, the other domains also have cross-sectional changes that modify the fluid velocity and the local Reynolds. The results of the variations of performance indicators are summarized in Table 4.4. Among the TES topologies assessed, radial flow TES presented the lowest thermal performance variability and in pressure drop values; hence, it can be adapted to any dimensional requirement and with low impact on its performance. The latter places it as a promising and versatile candidate for thermal energy storage designs.

Table 4.5 shows the maximum round-trip efficiency obtained among all $(AR\,,\,V_T)$ combinations, and the respective thermal losses and pressure drop. Even though the cylindrical TES with axial flow presented the highest value of η_{rt}, it also has the larges values of ΔP and Q_L. The aforementioned, suggest that it is necessary to study the quality of the energy obtained during the recovering process, since it may be with lower temperatures compared to other topologies, as a result of the high thermal losses through the lateral walls. On the other hand, cylindrical TES with radial flow presented the lowest values of all the performance indicators showed in Table 4.5, but the maximum round-trip efficiency obtained is only 4.2 % lower than axial flow TES. Furthermore, the pressure drop and overall heat losses are both near the 13 % of the obtained in cylindrical TES with axial flow, which also presented a tank volume 2.5 times bigger than the radial flow TES. Those differences allows the radial flow concept to compete with traditional TES topologies in key design parameters and performance indicators.

Table 4.4: Variation of the performance indicators for all TES topologies

Geometry	$\Delta\eta_{rt}$	$\Delta P_{max} - \Delta P_{min}$ Pa	ΔQ_{loss} kW h
Cyl. TES w/axial flow	0.153	284.066	697.485
Regular cone TES	0.583	158.722	770.066
Inverse cone TES	0.353	152.505	714.975
Cyl. TES w/radial flow	0.121	44.753	198.299

Table 4.5: Maximum round-trip efficiency and the respective pressure drop and overall thermal losses for all storage topologies

Geometry	η_{rt}	ΔP Pa	Q_{loss} kW h	AR	V_T m^3
Cyl. TES w/axial flow	0.897	271.352	865.625	0.5	20
Regular cone TES	0.877	161.412	597.305	0.5	12
Inverse cone TES	0.881	186.352	623.396	0.5	14
Cyl. TES w/radial flow	0.855	37.208	114.263	0.5	8

Geometric effects in radial flow TES

As mentioned before, a detailed analysis of the thermal losses is needed in the radial flow TES. Figure 4.10 plots the parametric behavior of the top/bottom and lateral thermal losses obtained for each combination of $(AR\,,\,V_T)$ in the radial flow TES. The dashed lines indicates the cases with the same aspect ratio, and the colorbar illustrates the increase in the tank volume.

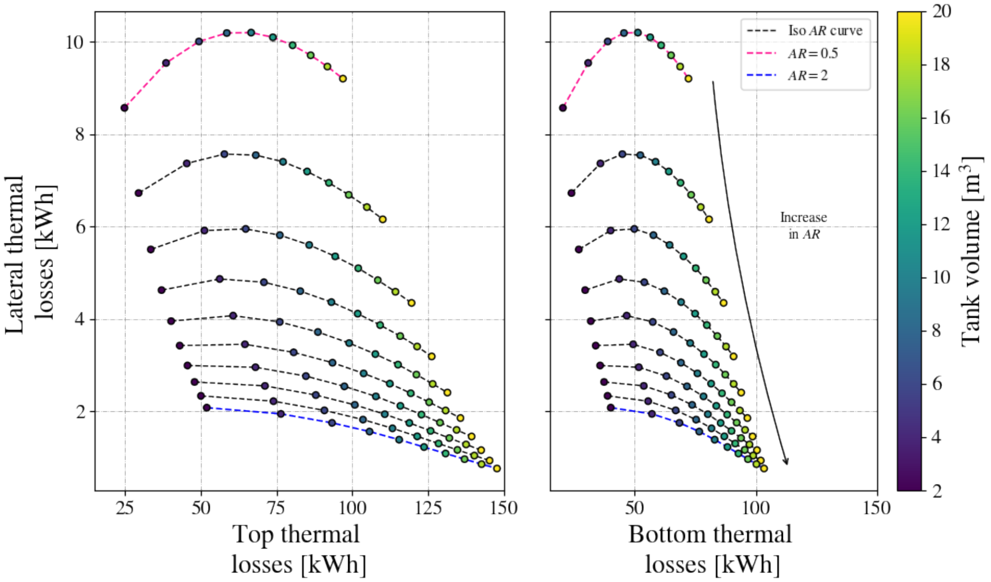

Figure 4.10: Parametric behavior of thermal losses in radial flow TES.

Considering the values achieved for the thermal losses, the behavior illustrated in Figure 4.10 confirms the “self-insulating" feature of the radial flow packed bed for all cases assessed. That result can be explained by the following reasons: (i) The outer layers of the packed-bed are always exposed to the lowest operating temperatures in the storage cycle, and (ii) when the surface area of the top/bottom lids is lower than the lateral walls (low aspect ratios), the temperature in the thermocline is higher; thus, that trade-off results in a less significant geometric impact. Moreover, as the aspect ratio increases for a fixed tank volume, the lateral losses decreases since the exposed area becomes smaller and the temperatures decrease as well in that zone. On the other hand, for a given value of AR, the evolution of the lateral thermal losses in the radial TES is similar to the behavior in the round-trip efficiency.

For the top and bottom thermal losses in the storage tank, the results show an expected behavior in terms of the tank volume and the aspect ratio. As V_T and AR increase, the surfaces exposed to high temperatures are larger; consequently, high thermal losses are achieved. Nevertheless, an important issue is recognized: as the bottom thermal losses are lower than the top thermal losses, that difference can be critical when the TES is on standby. The solids near the upper wall will decrease their temperature faster than the solids near the bottom, which may generate a non-uniform temperature distribution in the axial direction.

Regarding the irreversibilities caused by the heat transfer phenomena within the packed-bed, in Figure 4.11 the exergy destroyed due to convection and conduction is shown, for all the scenarios studied for radial flow TES. In general, convection losses are higher than conductive losses, since the first is the main heat transfer mechanism within the phases. Furthermore, the convection in packed-beds is a volumetric phenomenon, so its respective irreversibility is expected to be proportional to the storage volume. On the other hand, as the

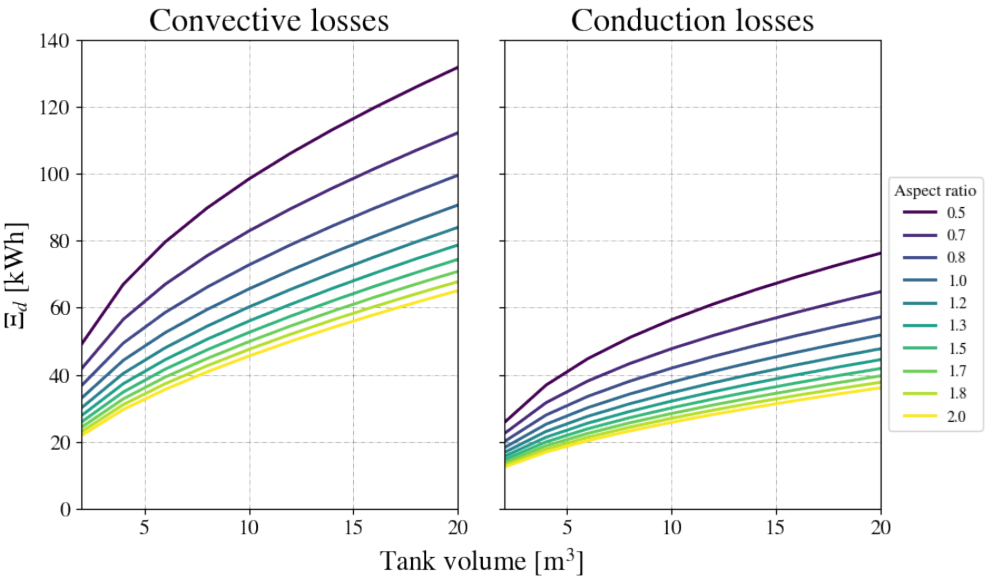

Figure 4.11: Exergy destroyed by convective and conductive heat transfer for different dimensions of radial flow TES

temperature difference between the phases increase, so does the entropy generation during the heat exchange. When the aspect ratio is low, temperatures at the outer layers of the TES are higher and during the initial periods of the discharging process, the temperature difference between the solid and the fluid is high as well, increasing the entropy generation during that heat transfer process.

4.4 Conclusions

The present work develops a parametric analysis of the performance of four different packed-bed topologies for high-temperature thermal energy storage in cyclic operation. A detailed modelling of the thermal losses and the entropy generation phenomena was conducted in order to establish different metrics to characterize the performance of the proposed topologies. The analysis of the cyclic operation of the packed-bed domains was carried out under the conditions. On the other hand, several design configurations were assessed in all storage topologies in terms of the aspect ratio and the tank volume, aiming to assess the impact of the geometric dimensions on the system's performance.

Important differences are observed between the TES topologies during their cyclic operation. Thermal losses in radial flow TES are 80% lower than tradicional TES topologies, which confirms its self-insulating feature. However, the cross-sectional variations of the radial flow TES cause changes in the airflow, affecting the heat transfer process and inducing an increase on the entropy generation. The parametric study showed that a critical aspect in the round-trip efficiency is the thermocline control, and its distribution is subject to the evolution of the mass flux rate across the packed-bed. Furthermore, the low variability on the performance of the radial flow TES systems regarding their geometric dimensions highlights a great advantage compared to other topologies, since a broad combinations of storage sizes, and geometric distributions can be employed, without a significant impact on its performance.

This study extends the available information of the radial flow packed-bed topology for thermal energy storage applications, placing this topology as a promising alternative compared to traditional TES domains. The low values on the pressure drop and thermal losses suggest that a thermo-economic analysis should be performed to evaluate the cost benefits. Finally, a detailed analysis in terms of the flow distribution within the packed during the charge/discharge process has to be carried out in future work in order to identify turbulence and other sources of entropy generation.

Chapter 5

General conclusions and future work

The present work deeply analyzed the design conditions of a packed-bed TES in terms of the storage material, geometric dimensions, and different concepts in packed-bed topologies aiming to study their influence in the system's performance indicators; thus, several guidelines were established to improve the operating conditions of the packed-bed TES. In addition, the use of industrial byproducts as filler materials were discussed as well, by means of the assessment of copper slags for high-temperature applications.

To develop the heat transfer analysis, several modelling approaches were reviewed. In actual packed-bed thermal models, the explicit integration of radiation heat transfer has not been discussed so far. In this work, a simplified study is conducted in chapter 2 in order to assess how the radiation can affect the packed-bed performance. The study showed that the radiation effects cannot be neglected from temperatures higher than 750 °C since the radiation heat transfer coefficient can achieve values as high as 32 % of the convection coefficient. Additionally, some modelling approaches are based on the integration of a local radiative heat transfer in the correlation of k_{eff}, which is insufficient to model the interaction with neighboring particles in a short- to long-range vicinity; therefore, a detailed investigation is required to determine the effects of including radiation at high-temperature conditions.

The present thesis proposes a practical use of copper slags, which were initially proposed in the 1960s highlighting its cost-effective potential, but without a detailed study of its engineering applications. Through the study of its properties and a heat transfer model, its potential use in high-temperature packed-bed TES applications is demonstrated. In fact, under the same geometric conditions, copper slags presented a stored energy density of $138\,\mathrm{kW\,h/m^3}$ against $129\,\mathrm{kW\,h/m^3}$ of the other industrial byproducts analyzed in this work. That feature allows the design of compact storage tanks, which can reduce TES costs for thermal and power generation systems. However, thermophysical properties of copper slags are highly heterogeneous, which increases the uncertainty in the evaluation of the system's overall performance. In that context, experimental studies have to be conducted to contrast the actual thermal performance of the packed-bed against the proposed models.

Another relevant parameter that influences the thermal performance of packed-bed TES, is the storage geometry. Recently, the concept of a novel radial flow TES has begun to be studied; nevertheless, there are no works that have detailed its behavior in cyclic operation, nor how its geometry affects its performance. In the comparative study developed in this thesis, a cyclic characterization and a parametric analysis were conducted for different packed-bed topologies. Owing to their self-insulating property, the radial flow topology can reduce thermal losses by 80 %, compared to conventional TES geometries. Furthermore, in contrast to other TES topologies, by varying the aspect ratio and tank volume, the radial flow TES presented the smallest change on the round-trip efficiency with a value of 12 % against the regular cone with a variation of 58 %. Hence, thermal performance of radial TES topology is less susceptible to changes in the aspect ratio and tank volume. The latter indicates that further research is needed to analyze other design variables. Even though this initial study demonstrates that radial flow TES has thermal losses and pressure drop values lower than traditional packed-bed systems, the lack of experimental research in radial flow topology adds uncertainty to these preliminary results, as the validity of the empirical correlations has yet to be verified.

Overall, the present dissertation showed that the use of copper slags as filler material for packed-bed TES is suitable for high-temperature applications, and it has been verified through several indicators: Experimental data of their thermophysical properties, a thermal model of the packed-bed using copper slags, and a comparative study with other waste materials analyzed in the literature. In addition, it includes studies that have not been discussed in depth by the scientific community, such as the explicit modelling of thermal radiation in packed-bed TES systems or the application of a radial flow packed-bed for high-temperature storage. This leads to further theoretical and experimental research, and the contribution to scientific knowledge in renewable energy systems.

Bibliography

[1] Ekkert, M.. Global energy transformation: a roadmap to 2050. 2018. ISBN 1059-910X.

[2] REN21, . Renewables 2019 Global Status Report Collaborative. July; 2019. ISBN 978-3-9818911-7-1. URL: `http://www.ren21.net/gsr-2019/pages/foreword/foreword/`.

[3] He, Y.L., Qiu, Y., Wang, K., Yuan, F., Wang, W.Q., Li, M.J., et al. Perspective of concentrating solar power. Energy 2020;198:1–22. doi:`10.1016/j.energy.2020.117373`.

[4] Agency, I.E.. Technology roadmap - solar thermal electricity. Tech. Rep.; IEA; 2014.

[5] Qazi, S.. Chapter 7 - solar thermal electricity and solar insolation. In: Qazi, S., editor. Standalone Photovoltaic (PV) Systems for Disaster Relief and Remote Areas. Elsevier. ISBN 978-0-12-803022-6; 2017, p. 203–237. doi:`https://doi.org/10.1016/B978-0-12-803022-6.00007-1`.

[6] Murphy, C., Sun, Y., Cole, W., Maclaurin, G., Turchi, C., Mehos, M., et al. The Potential Role of Concentrating Solar Power within the Context of DOE's 2030 Solar Cost Targets. Tech. Rep. NREL/TP-6A20-71912; NREL; 2019. URL: `https://www.nrel.gov/docs/fy19osti/71912.pdf`.

[7] Kolb, G.J., Ho, C.K., Mancini, T.R., Gary, J.A.. Power tower technology roadmap and cost reduction plan. Tech. Rep. April; Sandia National Laboratories; Albuquerque; 2012.

[8] González-Roubaud, E., Pérez-Osorio, D., Prieto, C.. Review of commercial thermal energy storage in concentrated solar power plants: Steam vs. molten salts. Renewable and Sustainable Energy Reviews 2017;80(March 2016):133–148. doi:`10.1016/j.rser.2017.05.084`.

[9] Lott, M.C., Kim, S.I.. Technology Roadmap: Energy Storage. Tech. Rep.; IEA - International Energy Agency; Paris, France; 2014. doi:`10.1007/SpringerReference_7300`.

[10] Montenegro Cardona, C.L.. Reducing the energy mismatch between demand and supply in the gemini south building. Ph.D. thesis; Faculty of Architecture; 2019.

[11] Kuravi, S., Trahan, J., Goswami, D.Y., Rahman, M.M., Stefanakos, E.K.. Thermal energy storage technologies and systems for concentrating solar power plants. Progress in Energy and Combustion Science 2013;39(4):285–319. doi:`10.1016/j.pecs.2013.02.001`.

[12] Herrmann, U., Geyer, M., Kearney, D.. Overview on Thermal Storage Systems. FLABEG Solar International GmbH February 20 - 21, 2002 Workshop on Thermal Storage for Trough Power Systems 2002;:23.

[13] Gil, A., Medrano, M., Martorell, I., Lázaro, A., Dolado, P., Zalba, B., et al. State of the art on high temperature thermal energy storage for power generation. Part 1—Concepts, materials and modellization. Renewable and Sustainable Energy Reviews 2010;14(1):31–55. doi:`10.1016/j.rser.2009.07.035`.

[14] Boukelia, T.E., Mecibah, M.S., Kumar, B.N., Reddy, K.S.. Investigation of solar parabolic trough power plants with and without integrated TES (thermal energy storage) and FBS (fuel backup system) using thermic oil and solar salt. Energy 2015;88:292–303. doi:`10.1016/j.energy.2015.05.038`.

[15] Rodríguez-Sánchez, M.. On the design of solar external receivers. Ph.D. thesis; Universidad Carlos III de Madrid; 2015.

[16] Hänchen, M., Brückner, S., Steinfeld, A.. High-temperature thermal storage using a packed bed of rocks - Heat transfer analysis and experimental validation. Applied Thermal Engineering 2011;31(10):1798–1806. doi:`10.1016/j.applthermaleng.2010.10.034`.

[17] Agalit, H., Zari, N., Maaroufi, M.. Thermophysical and chemical characterization of induction furnace slags for high temperature thermal energy storage in solar tower plants. Solar Energy Materials and Solar Cells 2017;172:168–176. doi:`10.1016/j.solmat.2017.07.035`.

[18] Ortega-Fernández, I., Calvet, N., Gil, A., Rodríguez-Aseguinolaza, J., Faik, A., D'Aguanno, B.. Thermophysical characterization of a by-product from the steel industry to be used as a sustainable and low-cost thermal energy storage material. Energy 2015;89:601–609. doi:`10.1016/j.energy.2015.05.153`.

[19] Ortega, I., Faik, A., Gil, A., Rodríguez-Aseguinolaza, J., D'Aguanno, B.. Thermophysical Properties of a Steel-making by-product to be used as Thermal Energy Storage Material in a Packed-bed System. In: Energy Procedia; vol. 69. Elsevier B.V.; 2015, p. 968–977. doi:`10.1016/j.egypro.2015.03.180`.

[20] Gautam, A., Saini, R.. A review on technical, applications and economic aspect of packed bed solar thermal energy storage system. Energy Storage 2020;27:101046. doi:`10.1016/j.est.2019.101046`.

[21] Green, R., Ottesen, D., Bartel, J., Bramlette, T.. High temperature thermal energy storage. Int Sol Energy Soc 1976;:11–26doi:`10.1016/b978-0-08-021724-6.50008-6`.

[22] Zhang, H., Baeyens, J., Cáceres, G., Degrève, J., Lv, Y.. Thermal energy storage: Recent developments and practical aspect. Prog Energy Combust Sci 2016;53:1–40. doi:`10.1016/j.pecs.2015.10.003`.

[23] Ma, Z., Glatzmaier, G.C., Wagner, M., Neises, T.. General performance metrics and applications to evaluate various thermal energy storage technologies. In: Energy Sustainability; vol. 44816. American Society of Mechanical Engineers; 2012, p. 345–351.

[24] Esence, T., Bruch, A., Fourmigué, J.F., Stutz, B.. Extended modeling of packed-bed sensible heat storage systems. In: AIP Conference Proceedings. 2018, p. 090007–1 – 8.

[25] Zanganeh, G., Pedretti, A., Zavattoni, S., Barbato, M., Steinfeld, A.. Packed-bed thermal storage for concentrated solar power - Pilot-scale demonstration and industrial-scale design. Solar Energy 2012;86(10):3084–3098. doi:`10.1016/j.solener.2012.07.019`.

[26] González, I., Pérez-Segarra, C., Lehmkuhl, O., Torras, S., Oliva, A.. Thermo-mechanical parametric analysis of packed-bed thermocline energy storage tanks. Applied Thermal Energy 2016;179:1106–1122. doi:`10.1016/j.apenergy.2016.06.124`.

[27] Zanganeh, G., Pedretti, A., Haselbacher, A., Steinfeld, A.. Design of packed bed thermal energy storage systems for high-temperature industrial process heat. Applied Energy 2015;137:812–822. doi:`10.1016/j.apenergy.2014.07.110`.

[28] Tiskatine, R., Oaddi, R., Ait El Cadi, R., Bazgaou, A., Bouirden, L., Aharoune, A., et al. Suitability and characteristics of rocks for sensible heat storage in CSP plants. Solar Energy Materials and Solar Cells 2017;169:245–257. doi:`10.1016/j.solmat.2017.05.033`.

[29] S. Kalaiselvam, R.P.. Thermal Energy Storage Technologies for Sustainability. Elsevier; 2014.

[30] Burström, P.E., Frishfelds, V., Ljung, A.L., Lundström, T.S., Marjavaara, B.D.. Modelling heat transfer during flow through a random packed bed of spheres. Heat and Mass Transfer 2018;54(4):1225–1245.

[31] Ortega-Fernández, I., Loroño, I., Faik, A., Uriz, I., Rodríguez-Aseguinolaza, J., D'Aguanno, B.. Parametric analysis of a packed bed thermal energy storage system. In: AIP Conference Proceedings; vol. 1850. American Institute of Physics Inc. ISBN 9780735415225; 2017, p. 080021. doi:`10.1063/1.4984442`.

[32] Galione, P.A., Pérez-Segarra, C.D., Rodríguez, I., Torras, S., Rigola, J.. Multi-layered solid-PCM thermocline thermal storage for CSP. Numerical evaluation of its application in a 50MWe plant. Solar Energy 2015;119:134–150. doi:`10.1016/j.solener.2015.06.029`.

[33] Cocco, D., Serra, F.. Performance comparison of two-tank direct and thermocline thermal energy storage systems for 1MWe class concentrating solar power plants. Energy 2015;81:526–536. doi:`10.1016/j.energy.2014.12.067`.

[34] Meier, A., Winkler, C., Wuillemin, D.. Experiment for modeling high temperature rock bed storage. Solar Energy Materials 1991;24:255–264.

[35] Cascetta, M., Cau, G., Puddu, P., Serra, F.. A study of a packed-bed thermal energy storage device: Test rig, experimental and numerical results. Energy Procedia 2015;81:987–994. doi:`10.1016/j.egypro.2015.12.157`.

[36] Anderson, R., Bates, L., Johnson, E., Morris, J.F.. Packed bed thermal energy storage: A simplified experimentally validated model. Journal of Energy Storage 2015;4:14–23. doi:`10.1016/j.est.2015.08.007`.

[37] Touzo, A., Olives, R., Dejean, G., Pham Minh, D., El Hafi, M., Hoffmann, J.F., et al. Experimental and numerical analysis of a packed-bed thermal energy storage system designed to recover high temperature waste heat: an industrial scale up. Journal of Energy Storage 2020;32(May):101894. doi:`10.1016/j.est.2020.101894`.

[38] Bindra, H., Bueno, P., Morris, J.F., Shinnar, R.. Thermal analysis and exergy evaluation of packed bed thermal storage systems. Applied Thermal Engineering 2013;52(2):255–263. doi:`10.1016/j.applthermaleng.2012.12.007`.

[39] Mctigue, J., Markides, C., White, A.. Performance response of packed-bed thermal storage to cycle duration perturbations. Energy Storage 2018;19:379–392. doi:`10.1016/j.est.2018.08.016`.

[40] Marongiu, F., Soprani, S., Engelbrecht, K.. Modeling of high temperature thermal energy storage in rock beds – Experimental comparison and parametric study. Applied Thermal Engineering 2019;163(12):114355. doi:`10.1016/j.applthermaleng.2019.114355`.

[41] Chandra, P., Willits, D.H.. Pressure drop and heat transfer characteristics of air-rockbed thermal storage systems. Solar Energy 1981;27(6):547—-553. doi:`10.1016/0038-092X(81)90050-5`.

[42] Coutier, J.P., Farber, E.A.. Two applications of a numerical approach of heat transfer process within rock beds. Solar Energy 1982;29(6):451–462. doi:`10.1016/0038-092X(82)90053-6`.

[43] Xu, C., Wang, Z., He, Y., Li, X., Bai, F.. Parametric study and standby behavior of a packed-bed molten salt thermocline thermal storage system. Renewable Energy 2012;48(12):1–9. doi:`10.1016/j.renene.2012.04.017`.

[44] Mawire, A., Taole, S.H.. A comparison of experimental thermal stratification parameters for an oil/pebble-bed thermal energy storage (TES) system during charging. Applied Energy 2011;88(12):4766–4778. doi:`10.1016/j.apenergy.2011.06.019`.

[45] Aly, S.L., El-Sharkawy, A.I.. Effect of wall temperature on the thermal behavior of a packed bed. Heat Recovery Systems and CHP 1990;10(1):55–60. doi:`10.1016/0890-4332(90)90250-N`.

[46] Mertens, N., Alobaid, F., Frigge, L., Epple, B.. Dynamic simulation of integrated rock-bed thermocline storage for concentrated solar power. Sol Energy 2014;110:830–842. doi:`10.1016/j.solener.2014.10.021`.

[47] Zavattoni, S., Barbato, M., Pedretti, A., Zanganeh, G., Steinfeld, A.. High temperature rock-bed TES system suitable for industrial-scale CSP plant - CFD analysis under charge/discharge cyclic conditions. Energy Procedia 2014;:124–133doi:`10.1016/j.egypro.2014.01.165`.

[48] Esence, T., Bruch, A., Molina, S., Stutz, B., Fourmigué, J.F.. A review on experience feedback and numerical modeling of packed-bed thermal energy storage systems. Solar Energy 2017;153:628–654. doi:`10.1016/j.solener.2017.03.032`.

[49] Marti, J., Geissbühler, L., Becattini, V., Haselbacher, A., Steinfeld, A.. Constrained multi-objective optimization of thermocline packed-bed thermal-energy storage. Applied Energy 2018;216:694–708. doi:`10.1016/j.apenergy.2017.12.072`.

[50] Ismail, K.A., Stuginsky, R.. Parametric study on possible fixed bed models for pcm and sensible heat storage. Applied Thermal Engineering 1999;19(7):757–788. doi:`10.1016/S1359-4311(98)00081-7`.

[51] Grirate, H., Agalit, H., Zari, N., Elmchaouri, A., Molina, S., Couturier, R.. Experimental and numerical investigation of potential filler materials for thermal oil thermocline storage. Solar Energy 2016;131:260–274. doi:`10.1016/J.SOLENER.2016.02.035`.

[52] Tamme, R., Laing, D., Steinmann, W.D.. Advanced thermal energy storage technology for parabolic trough. International Solar Energy Conference 2003;January:563–571. doi:`10.1115/ISEC2003-44033`.

[53] Laing, D., Steinmann, W.D., Tamme, R., Richter, C.. Solid media thermal storage for parabolic trough power plants. Solar Energy 2006;80(10):1283–1289. doi:`10.1016/j.solener.2006.06.003`.

[54] Khare, S., Dell'Amico, M., Knight, C., McGarry, S.. Selection of materials for high temperature sensible energy storage. Solar Energy Materials and Solar Cells 2013;115:114–122. doi:`10.1016/j.solmat.2013.03.009`.

[55] El-Sharkawy, H., El Bably, M., Ibrahim, O., Adel, R., Gendy, R., Asaad, M., et al. Thermal Storage Concrete. In: Proceedings of the 2015 CSCE Annual Conference, At Regina. May; 2015, p. 1–10. doi:`10.13140/RG.2.1.3608.5924`.

[56] Grosu, Y., Ortega-Fernández, I., González-Fernández, L., Nithiyanantham, U., Baba, Y.F., Mers], A.A., et al. Natural and by-product materials for thermocline-based thermal energy storage system at CSP plant: Structural and thermophysical properties. Applied Thermal Engineering 2018;136:185–193. doi:`https://doi.org/10.1016/j.applthermaleng.2018.02.087`.

[57] Htun, N.N., Sukchai, S., Hemavibool, S.. Properties of concrete material for thermal

energy storage. In: 2014 International Conference and Utility Exhibition on Green Energy for Sustainable Development (ICUE). 2014, p. 1–5.

[58] Wang, Y., Wang, Y., Li, H., Zhou, J., Cen, K.. Thermal properties and friction behaviors of slag as energy storage material in concentrate solar power plants. Solar Energy Materials and Solar Cells 2018;182(March):21–29. doi:`10.1016/j.solmat.2018.03.020`.

[59] Navarro, M.E., Martínez, M., Gil, A., Fernández, A.I., Cabeza, L.F., Olives, R., et al. Selection and characterization of recycled materials for sensible thermal energy storage. Solar Energy Materials and Solar Cells 2012;107:131–135. doi:`10.1016/j.solmat.2012.07.032`.

[60] Miró, L., Navarro, M.E., Suresh, P., Gil, A., Fernández, A.I., Cabeza, L.F.. Experimental characterization of a solid industrial by-product as material for high temperature sensible thermal energy storage (TES). Applied Energy 2014;113:1261–1268. doi:`10.1016/j.apenergy.2013.08.082`.

[61] Calvet, N., Meffre, A., Olivès, R., Guillot, E., Py, X., Bessada, C., et al. Matériau de stockage thermique par chaleur sensible pour centrales électro-solaires testé sous flux solaire concentré. In: Proceedings in Congres Francais de Thermique. 2010, p. 183,1–6.

[62] Fritsch, A., Flesch, J., Geza, V., Singer, C., Uhlig, R., Hoffschmidt, B.. Conceptual Study of Central Receiver Systems with Liquid Metals as Efficient Heat Transfer Fluids. Energy Procedia 2015;69(0):644–653. doi:`10.1016/j.egypro.2015.03.074`.

[63] Méndez, A.. Utilización de escorias como sustitutos de áridos. Master's thesis; R Escuela de Organización Industrial; Spain; 2003.

[64] Krishna, Y., Faizal, M., Saidur, R., Ng, K.C., Aslfattahi, N.. State-of-the-art heat transfer fluids for parabolic trough collector. International Journal of Heat and Mass Transfer 2020;152. doi:`10.1016/j.ijheatmasstransfer.2020.119541`.

[65] Bruch, A., Fourmigué, J., Couturier, R.. Experimental and numerical investigation of a pilot-scale thermal oil packed bed thermal storage system for CSP power plant. Solar Energy 2014;105:116–125. doi:`10.1016/j.solener.2014.03.019`.

[66] Bruch, A., Molina, S., Esence, T., Fourmigué, J.F., Couturier, R.. Experimental investigation of cycling behaviour of pilot-scale thermal oil packed-bed thermal storage system. Renewable Energy 2017;103(4):277–285. doi:`10.1016/j.renene.2016.11.029`.

[67] Kenda, E.S., N'Tsoukpoe, K.E., Ouédraogo, I.W., Coulibaly, Y., Py, X., Ouédraogo, F.M.A.W.. Jatropha curcas crude oil as heat transfer fluid or thermal energy storage material for concentrating solar power plants. Energy for Sustainable Development 2017;40:59–67. doi:`10.1016/j.esd.2017.07.003`.

[68] Hoffmann, J.F., Fasquelle, T., Vaitilingom, G., Olives, R., Py, X., Goetz, V.. Compatibility of vegetable oils with solid filler materials for thermocline thermal energy

storage systems. Solar Energy Materials and Solar Cells 2019;200. doi:`10.1016/j.solmat.2019.109932`.

[69] Almendros-Ibáñez, J.A., Fernández-Torrijos, M., Díaz-Heras, M., Belmonte, J.F., Sobrino, C.. A review of solar thermal energy storage in beds of particles: Packed and fluidized beds. Solar Energy 2019;192(May 2018):193–237. doi:`10.1016/j.solener.2018.05.047`.

[70] Motte, F., Falcoz, Q., Veron, E., Py, X.. Compatibility tests between Solar Salt and thermal storage ceramics from inorganic industrial wastes. Applied Energy 2015;155:14–22. doi:`https://doi.org/10.1016/j.apenergy.2015.05.074`.

[71] Ortega-Fernández, I., Grosu, Y., Ocio, A., Arias, P.L., Rodríguez-Aseguinolaza, J., Faik, A.. New insights into the corrosion mechanism between molten nitrate salts and ceramic materials for packed bed thermocline systems: A case study for steel slag and Solar salt. Solar Energy 2018;173(December 2016):152–159. doi:`10.1016/j.solener.2018.07.040`.

[72] Brosseau, D., Edgar, M., Kelton, J.W., Chisman, K., Ray, D., Emms, B.. Testing of Thermocline Filler Materials and Molten-Salt Heat Transfer Fluids for Thermal Energy Storage Systems in Parabolic Trough Power Plants. 2004. doi:`10.1115/ISEC2004-65144`.

[73] Bonk, A., Martin, C., Braun, M., Bauer, T.. Material investigations on the thermal stability of solar salt and potential filler materials for molten salt storage. In: AIP Conference Proceedings; vol. 1850. AIP Publishing LLC; 2017, p. 080008.

[74] Niedermeier, K., Marocco, L., Flesch, J., Mohan, G., Coventry, J., Wetzel, T.. Performance of molten sodium vs. molten salts in a packed bed thermal energy storage. Applied Thermal Engineering 2018;141(May):368–377. doi:`10.1016/j.applthermaleng.2018.05.080`.

[75] Li, M.J., Qiu, Y., Li, M.J.. Cyclic thermal performance analysis of a traditional Single-Layered and of a novel Multi-Layered Packed-Bed molten salt Thermocline Tank. Renewable Energy 2018;118:565–578. doi:`10.1016/j.renene.2017.11.038`.

[76] Chen Zhao, B., song Cheng, M., Liu, C., min Dai, Z.. System-level performance optimization of molten-salt packed-bed thermal energy storage for concentrating solar power. Applied Energy 2018;226(May):225–239. doi:`10.1016/j.apenergy.2018.05.081`.

[77] Chen Zhao, B., song Cheng, M., Liu, C., min Dai, Z.. Cyclic thermal characterization of a molten-salt packed-bed thermal energy storage for concentrating solar power. Applied Energy 2017;195:761–773. doi:`10.1016/j.apenergy.2017.03.110`.

[78] Abdulla, A., Reddy, K.S.. Effect of operating parameters on thermal performance of molten salt packed-bed thermocline thermal energy storage system for concentrating solar power plants. International Journal of Thermal Sciences 2017;121:30–44. doi:`10.1016/j.ijthermalsci.2017.07.004`.

[79] Yin, H., Ding, J., Jiang, R., Yang, X.. Thermocline characteristics of molten-salt thermal energy storage in porous packed-bed tank. Applied Thermal Engineering 2017;110:855–863. doi:`10.1016/j.applthermaleng.2016.08.214`.

[80] Shitzer, A., Levy, M.. Transient Behavior of a Rock-Bed Thermal Storage System Subjected to Variable Inlet Air Temperatures: Analysis and Experimentation. Journal of Solar Energy Engineering 1983;105(2):200–206. doi:`10.1115/1.3266366`.

[81] White, A.J., McTigue, J.D., Markides, C.N.. Analysis and optimisation of packed-bed thermal reservoirs for electricity storage applications. Proceedings of the Institution of Mechanical Engineers, Part A: Journal of Power and Energy 2016;230(7):739–754. doi:`10.1177/0957650916668447`.

[82] Esence, T., Desrues, T., Fourmigué, J.F., Cwicklinski, G., Bruch, A., Stutz, B.. Experimental study and numerical modelling of high temperature gas/solid packed-bed heat storage systems. Energy 2019;180:61–78. doi:`10.1016/j.energy.2019.05.012`.

[83] Biencinto, M., González, L., Valenzuela, L., Zarza, E.. A new concept of solar thermal power plants with large-aperture parabolic-trough collectors and sCO2 as working fluid. Energy Conversion and Management 2019;199:112030. doi:`https://doi.org/10.1016/j.enconman.2019.112030`.

[84] Vutukuru, R., Pegallapati, A.S., Maddali, R.. Suitability of various heat transfer fluids for high temperature solar thermal systems. Applied Thermal Engineering 2019;159(May):113973. doi:`10.1016/j.applthermaleng.2019.113973`.

[85] Díaz-Heras, M., Belmonte, J.F., Almendros-Ibáñez, J.A.. Effective thermal conductivities in packed beds: Review of correlations and its influence on system performance. Applied Thermal Engineering 2020;171(February):115048. doi:`10.1016/j.applthermaleng.2020.115048`.

[86] Jalalzadeh-Azar, A.A., Steele, W.G., Adebiyi, G.A.. Heat transfer in a high-temperature packed bed thermal energy storage system—roles of radiation and intraparticle conduction. Journal of Energy Resources Technology, Transactions of the ASME 1996;118(1):50–57. doi:`10.1115/1.2792693`.

[87] Vortmeyer, D., Schaefer, R.J.. Equivalence of one- and two-phase models for heat transfer processes in packed beds: one dimensional theory. Chemical Engineering Science 1974;29(2):485–491. doi:`10.1016/0009-2509(74)80059-X`.

[88] Riaz, M.. Transient analysis of packed-bed thermal storage systems. Solar Energy 1978;21(2):123–128. doi:`https://doi.org/10.1016/0038-092X(78)90039-7`.

[89] Bindra, H., Bueno, P., Morris, J.F.. Sliding flow method for exergetically efficient packed bed thermal storage. Applied Thermal Engineering 2014;64(1-2):201–208. doi:`10.1016/j.applthermaleng.2013.12.028`.

[90] Hadley, G.R.. Thermal conductivity of packed metal powders. International Journal of Heat and Mass Transfer 1986;29(6):909–920. doi:`https://doi.org/10.1016/`

0017-9310(86)90186-9.

[91] Zehner, P., Schlünder, E.U.. Warmeleitfahigkeit von Schuttungen bei mässigen Temperaturen. Chemie Ingenieur Technik 1970;42:933–941.

[92] Krupiczka, R.. Analysis of thermal conductivity in granular materials. International Chemical Engineering 1967;7(1):122–+.

[93] Gonzo, E.E.. Estimating correlations for the effective thermal conductivity of granular materials. Chemical Engineering Journal 2002;90(3):299–302.

[94] Sih, S.S., Barlow, J.W.. The Prediction of the Thermal Conductivity of Powders. Proceedings of the Solid Freeform Fabrication Symposium 1994;2:397–401.

[95] Rousseau, P.G., Du Toit, C.G., Van Antwerpen, W., Van Antwerpen, H.J.. Separate effects tests to determine the effective thermal conductivity in the PBMR HTTU test facility. Nuclear Engineering and Design 2014;271:444–458. doi:`10.1016/j.nucengdes.2013.12.015`.

[96] De Beer, M., Du Toit, C.G., Rousseau, P.G.. Experimental study of the effective thermal conductivity in the near-wall region of a packed pebble bed. Nuclear Engineering and Design 2018;339(September):253–268. doi:`10.1016/j.nucengdes.2018.09.014`.

[97] De Beer, M., Rousseau, P.G., Du Toit, C.G.. A review of methods to predict the effective thermal conductivity of packed pebble beds, with emphasis on the near-wall region. Nuclear Engineering and Design 2018;331(February):248–262. doi:`10.1016/j.nucengdes.2018.02.029`.

[98] Yagi, S., Kunii, D., Wakao, N.. Studies on axial effective thermal conductivities in packed beds. AIChE Journal 1960;6(4):543–546. doi:`10.1002/aic.690060407`.

[99] Elsari, M., Hughes, R.. Axial effective thermal conductivities of packed beds. Applied Thermal Engineering 2002;22(18):1969–1980.

[100] Kuwahara, F., Nakayama, A., Koyama, H.. A Numerical Study of Thermal Dispersion in Porous Media. Journal of Heat Transfer 1996;118(3):756–761. doi:`10.1115/1.2822696`.

[101] Batchelor, G.K., O'brien, R.. Thermal or electrical conduction through a granular material. Proceedings of the Royal Society of London A Mathematical and Physical Sciences 1977;355(1682):313–333.

[102] Deissler, R., Boegli, J.. An investigation of effective thermal conductivities of powders in various gases. Trans Am Soc Mech Engrs 1958;80.

[103] Sih, S.S., Barlow, J.W.. The prediction of the thermal conductivity of powders. In: 1995 International Solid Freeform Fabrication Symposium. 1995, p. 397–401.

[104] Breitbach, G., Barthels, H.. The radiant heat transfer in the high temperature reactor

core after failure of the afterheat removal systems. Nuclear Technology 1980;49(3):392–399.

[105] Zehner, P., Schlünder, E.. Einfluß der wärmestrahlung und des druckes auf den wärmetransport in nicht durchströmten schüttungen. Chemie Ingenieur Technik 1972;44(23):1303–1308.

[106] Vortmeyer, D.. Wärmestrahlung in dispersen feststoffsystemen. Chemie Ingenieur Technik 1979;51(9):839–851.

[107] Demirel, Y., Abu-Al-Saud, B.A., Al-Ali, H.H., Makkawi, Y.. Packing size and shape effects on forced convection in large rectangular packed ducts with asymmetric heating. International Journal of Heat and Mass Transfer 1999;42(17):3267–3277. doi:`https://doi.org/10.1016/S0017-9310(98)00370-6`.

[108] Bunnell, D., Irvin, H., Olson, R., Smith, J.. Effective thermal conductivities in gas-solid systems. Industrial & Engineering Chemistry 1949;41(9):1977–1981.

[109] Löf, G.O.G., Hawley, R.W.. Unsteady-State Heat Transfer between air and loose solids. Industrial & Engineering Chemistry 1948;40(6):1061–1070. doi:`10.1021/ie50462a017`.

[110] Dunkle, R.V.. Randomly-Packed Particulate Bed Regenerators and Evaporative Coolers for Use in Solar Systems. In: Proceedings of the 2nd Southeastern Conference on APPLICATION OF SOLAR ENERGY. Baton Rouge, Louisiana; 1976, p. 131–147.

[111] Alanís, E., Saravia, L., Rovetta, L.. Measurement of Rock Pile Heat Transfer Coefficients. Solar Energy 1977;19:571–572.

[112] Wu, C.C., Hwang, G.J.. Flow and Heat Transfer Characteristics Inside Packed and Fluidized Beds. Journal of Heat Transfer 1998;120(3):667. doi:`10.1115/1.2824335`.

[113] Whitaker, S.. Forced Convection Heat Transfer Correlations for Flow in Pipes , Past Flat Plates , Single Cylinders , Single Spheres , and for Flow in Packed Beds and Tube Bundles. AIChE Journal 1972;18(2):361–371.

[114] Gupta, S.N., Chaube, R.B., Upadhyay, S.N.. Fluid-Particle Heat Transfer in Fixed and Fluidized Beds. Chemical Engineering Science, 1974;29:839–843.

[115] Gunn, D.J., De Souza, J.. Heat transfer and axial dispersion in packed beds. Chemical Engineering Science 1974;29(6):1363–1371. doi:`10.1016/0009-2509(74)80160-0`.

[116] Wakao, N., Kaguei, S., Funazkri, T.. Effect of fluid dispersion coefficients on particle-to-fluid heat transfer coefficients in packed beds: Correlation of Nusselt numbers. Chemical Engineering Science 1979;34(3):325–336. doi:`10.1016/0009-2509(79)85064-2`.

[117] Gunn, D.J.. Transfer of heat or mass to particles in fixed and fluidised beds. International Journal of Heat and Mass Transfer 1978;21:467–476.

[118] Wakao, N., Kaguei, S.. Heat and Mass Transfer in Packed Beds; vol. 1. 1982.

[119] Hanrattry, T.J.. Nature of wall heat transfer coefficient in packed beds. Chemical Engineering Science 1954;3:209–214.

[120] Schwartz, C.E., J.M., S.. Flow distribution in Packed Beds. Industrial and Engineering Chemistry 1953;45(9):1209–1218.

[121] Denloye, A.O.O., Botterill, J.S.M.. Heat transfer in flowing packed beds. Chemical Engineering Science 1977;32(2):461–465.

[122] Thoenes, D., Kramers, H.. Mass transfer from spheres in various regular packings to a flowing fluid. Chemical Engineering Science 1958;8:271–283.

[123] Yagi, S., Kunii, D.. Studies on heat transfer near wall surface in packed beds. AIChE Journal 1960;6(1):97–104. doi:`10.1002/aic.690060119`.

[124] Yagi, S., Wakao, N.. Heat and mass transfer from wall to fluid in packed beds. AIChE Journal 1959;5(1):79–85. doi:`10.1002/aic.690050118`.

[125] Beek, J.. Design of Packed Catalytic Reactors. Advances in Chemical Engineering 1962;3(C):203–271. doi:`10.1016/S0065-2377(08)60060-5`.

[126] Dixon, A., DiCostanzo, M., Soucyt, B.A.. Fluid-phase radial transport in packed beds of low tube-to-particle diameter ratio. International Journal of Heat and Mass Transfer 1984;27(10):1701–1713.

[127] Ofuchi, K., Kunii, D.. Heat-transfer characteristics of packed beds with stagnant fluids. International Journal of Heat and Mass Transfer 1965;8(5):749–757. doi:`10.1016/0017-9310(65)90021-9`.

[128] Whitaker, S.. Flow in porous media I: A theoretical derivation of Darcy's law. Transport in Porous Media 1986;1(1):3–25. doi:`10.1007/BF01036523`.

[129] Kaviany, N.. Principles of Heat Transfer in Porous Media. Springer; 1999.

[130] Ergun, S.. Fluid Flow Through Packed Columns. Chemical engineering progress 1952;48(2):89–94.

[131] Bird, N., Stewart, W., Lightfoot, E.. Transport Phenomena Second Edition. John Wiley and Sons; 2002.

[132] Macdonald, I.F., El-Sayed, M.S., Mow, K., Dullien, F.A.. Flow through Porous Media—the Ergun Equation Revisited. Industrial and Engineering Chemistry Fundamentals 1979;18(3):199–208. doi:`10.1021/i160071a001`.

[133] Dunkle R. Ellul, W.. Randomly packed particulate bed regenerators and evaporative coolers. Eng Aust Mech Chem Eng Trans 1972;:117–121.

[134] du Plessis, J.P., Woudberg, S.. Pore-scale derivation of the Ergun equation to enhance

its adaptability and generalization. Chemical Engineering Science 2008;63(9):2576–2586. doi:10.1016/j.ces.2008.02.017.

[135] Schumann, T.. Heat transfer: A liquid flowing through a porous prism. Journal of the Franklin Institute 1929;208(3):405–416. doi:10.1016/S0016-0032(29)91186-8.

[136] Crider, J.E., Foss, A.S.. Effective wall heat transfer coefficients and thermal resistances in mathematical models of packed beds. AIChE Journal 1965;11(6):1012–1019. doi:10.1002/aic.690110613.

[137] Littman, H., Barile, R.G., Pulsifer, A.H.. Gas-particle heat transfer coefficients in packed beds at low Reynolds numbers. Industrial & Engineering Chemistry Fundamentals 2020;7(04):554–561. doi:10.1021/i160028a005.

[138] Handley, D., Heggs, P.. The effect of thermal conductivity of the packing material on transient heat transfer in a fixed bed. International Journal of Heat and Mass Transfer 1969;12(5):549 – 570. doi:10.1016/0017-9310(69)90038-6.

[139] Wakao, N.. Particle-to-fluid transfer coefficients and fluid diffusivities at low flow rate in packed beds. Chemical Engineering Science 1976;31(12):1115–1122. doi:10.1016/0009-2509(76)85021-X.

[140] Hasegawa, I., Oshima, T.. Void Fraction of Multi-Component Randomly Packed Beds with Size Distributions. KONA Powder and Particle 1985;11(4):438–443. doi:10.1252/kakoronbunshu.11.438.

[141] Beasley, D.E., Clark, J.A.. Transient response of a packed bed for thermal energy storage. International Journal of Heat and Mass Transfer 1984;27(9):1659–1669. doi:10.1016/0017-9310(84)90278-3.

[142] Hoffmann, J.F., Fasquelle, T., Goetz, V., Py, X.. A thermocline thermal energy storage system with filler materials for concentrated solar power plants: Experimental data and numerical model sensitivity to different experimental tank scales. Applied Thermal Engineering 2016;100:753–761. doi:10.1016/j.applthermaleng.2016.01.110.

[143] Odenthal, C., Klasing, F., Bauer, T.. A three-equation thermocline thermal energy storage model for bidisperse packed beds. Solar Energy 2019;191(7):410–419. doi:10.1016/j.solener.2019.09.005.

[144] Johnson, E., Bates, L., Dower, A., Bueno, P.C., Anderson, R.. Thermal energy storage with supercritical carbon dioxide in a packed bed: Modeling charge-discharge cycles. Journal of Supercritical Fluids 2018;137(December 2017):57–65. doi:10.1016/j.supflu.2018.03.009.

[145] Anderson, R., Shiri, S., Bindra, H., Morris, J.F.. Experimental results and modeling of energy storage and recovery in a packed bed of alumina particles. Applied Energy 2014;119:521 – 529. doi:https://doi.org/10.1016/j.apenergy.2014.01.030.

[146] Al-Azawii, M.M., Theade, C., Danczyk, M., Johnson, E., Anderson, R.. Experimental study on the cyclic behavior of thermal energy storage in an air-alumina packed bed. Journal of Energy Storage 2018;18(May):239–249. doi:`10.1016/j.est.2018.05.008`.

[147] Ahlem Bouguila, , Said, R.. Performance investigation of a 100-kWhth thermocline packed bed thermal energy storage system: Comparison between synthetic oil and vegetable oil. Advances in Mechanical Engineering 2020;12(4):1–10. doi:`10.1177/1687814020905746`.

[148] Bueno, P.C., Bates, L., Anderson, R., Bindra, H.. Thermal Energy Storage for the Supercritical CO2 Brayton Cycle. In: ASME, , editor. Proceedings of ASME Turbo Expo 2015. Montréal, Canada: ASME; 2015, p. 1–9.

[149] Mawire, A., McPherson, M., den Heetkamp, R.R., Mlatho, S.J.. Simulated performance of storage materials for pebble bed thermal energy storage (TES) systems. Applied Energy 2009;86(7-8):1246–1252. doi:`10.1016/j.apenergy.2008.09.009`.

[150] Cascetta, M., Cau, G., Puddu, P., Serra, F.. Numerical investigation of a packed bed thermal energy storage system with different heat transfer fluids. Energy Procedia 2014;45:598–607. doi:`10.1016/j.egypro.2014.01.064`.

[151] Kocak, B., Paksoy, H.O.. Numerical Model of Lab-Scale Packed-Bed Thermal Energy Storage System. In: Ires; vol. 4. Atlantis Press; 2019, p. 59–63. doi:`10.2991/ires-19.2019.7`.

[152] Yoo, J., Yoon, S.J., O'brien, T.E., Frick, K.L., O'brien, J.E., Sabharwall, P., et al. Design optimization study on the single tank packed bed thermal energy storage system. Tech. Rep. November; Idaho National Laboratory; Idaho; 2018.

[153] Xu, C., Wang, Z., He, Y., Li, X., Bai, F.. Sensitivity analysis of the numerical study on the thermal performance of a packed-bed molten salt thermocline thermal storage system. Applied Energy 2012;92:65–75. doi:`10.1016/j.apenergy.2011.11.002`.

[154] Kocak, B., Paksoy, H.. Performance of laboratory scale packed-bed thermal energy storage using new demolition waste based sensible heat materials for industrial solar applications. Solar Energy 2020;211(October):1335–1346. doi:`10.1016/j.solener.2020.10.070`.

[155] Lugolole, R., Mawire, A., Lentswe, K.A., Okello, D., Nyeinga, K.. Thermal performance comparison of three sensible heat thermal energy storage systems during charging cycles. Sustainable Energy Technologies and Assessments 2018;30(September):37–51. doi:`10.1016/j.seta.2018.09.002`.

[156] Cascetta, M., Cau, G., Puddu, P., Serra, F.. A comparison between CFD simulation and experimental investigation of a packed-bed thermal energy storage system. Applied Thermal Engineering 2016;98:1263–1272. doi:`10.1016/j.applthermaleng.2016.01.019`.

[157] Cascetta, M., Serra, F., Cau, G., Puddu, P.. Comparison between experimental

and numerical results of a packed-bed thermal energy storage system in continuous operation. Energy Procedia 2018;148:234–241. doi:`10.1016/j.egypro.2018.08.073`.

[158] Soprani, S., Marongiu, F., Christensen, L., Alm, O., Petersen, K.D., Ulrich, T., et al. Design and testing of a horizontal rock bed for high temperature thermal energy storage. Applied Energy 2019;251(May):113345. doi:`10.1016/j.apenergy.2019.113345`.

[159] Barton, N.. Simulations of air-blown thermal storage in a rock bed. Applied Thermal Engineering 2013;55:43–50. doi:`10.1016/j.applthermaleng.2013.03.002`.

[160] Contestabile, F., Cornolti, L., Zavattoni, S., Barbato, M.C.. An advanced wall treatment for a 1D model of packed bed thermal energy storage systems. Journal of Energy Storage 2019;26(7):100918. doi:`10.1016/j.est.2019.100918`.

[161] Klein, P., Roos, T., Sheer, J.. Numerical simulation of a high temperature thermal storage unit for solar gas turbine applications. SolarPaces Conference 2010;.

[162] Klein, P., Roos, T.H., Sheer, T.J.. Experimental investigation into a packed bed thermal storage solution for solar gas turbine systems. Energy Procedia 2014;49:840–849. doi:`10.1016/j.egypro.2014.03.091`.

[163] Rodrigues, F.A., de Lemos, M.J.. Effect of porous material properties on thermal efficiencies of a thermocline storage tank. Applied Thermal Engineering 2020;173:115194. doi:`https://doi.org/10.1016/j.applthermaleng.2020.115194`.

[164] Bai, Y., Yang, M., Wang, Z., Li, X., Chen, L.. Thermal stratification in a cylindrical tank due to heat losses while in standby mode. Solar Energy 2019;185:222 – 234. doi:`https://doi.org/10.1016/j.solener.2018.12.063`.

[165] Wu, H., Gui, N., Yang, X., Tu, J., Jiang, S.. Numerical simulation of heat transfer in packed pebble beds: CFD-DEM coupled with particle thermal radiation. International Journal of Heat and Mass Transfer 2017;110:393–405. doi:`10.1016/j.ijheatmasstransfer.2017.03.035`.

[166] Ruiz, G., Ripoll, N., Fedorova, N., Zbogar-Rasic, A., Jovicic, V., Delgado, A., et al. Experimental and numerical analysis of the heat transfer in a packed bed exposed to the high thermal radiation flux. International Journal of Heat and Mass Transfer 2019;136:383–392. doi:`10.1016/j.ijheatmasstransfer.2019.03.009`.

[167] Wu, H., Gui, N., Yang, X., Tu, J., Jiang, S.. Analysis and evaluations of four models of thermal radiation for densely packed granular systems. Chemical Engineering Science 2020;211:115309. doi:`10.1016/j.ces.2019.115309`.

[168] Wu, H., Gui, N., Yang, X., Tu, J., Jiang, S.. Effect of scale on the modeling of radiation heat transfer in packed pebble beds. International Journal of Heat and Mass Transfer 2016;101:562–569. doi:`10.1016/j.ijheatmasstransfer.2016.05.090`.

[169] Schotte, W.. Thermal conductivity of packed beds. AIChE Journal 1960;6(1):63–67. doi:`10.1002/aic.690060113`.

[170] Kunii, D., J.M., S.. Heat Transfer Characteristics of Porous Rocks: II Thermal Conductivities of Unconsolidated Particles with Flowing Fluids. AIChE Journal 1961;7(1):29–34.

[171] Wakao, N., Kato, K., Furuya, N.. View factor between two hemispheres in contact and radiation heat-transfer coefficient in packed beds. International Journal of Heat and Mass Transfer 1969;12:118–120.

[172] Juul, N.H.. Investigation of approximate methods for calculation of the diffuse radiation configuration view factor between two spheres. Letters in heat and Mass Transfer 1976;3(6):513–521.

[173] Felske, J.. Approximate radiation shape factors between two spheres. Journal of Heat Transfer 1978;10:547.

[174] Tanaka, S.. Exact View-factor Analysis for Radiat ion from a Sphere to another Sphere linked with a Coaxial Cylinder. Review of the Faculty of Marit ime Sciences, Kobe University 2008;5:85–92.

[175] Han, K., Feng, Y.T., Owen, D.R.. An accurate algorithm for evaluating radiative heat transfer in a randomly packed bed. CMES - Computer Modeling in Engineering and Sciences 2009;49(2):143–161. doi:`10.3970/cmes.2009.049.143`.

[176] Howell, J.R., Siegel, R., Menguc, M.P.. Thermal radiation heat transfer. 5th ed.; Boca Raton, Fla.: CRC Press; 2011. ISBN 9781439805336 1439805334.

[177] Feng, Y.T., Han, K.. An accurate evaluation of geometric view factors for modelling radiative heat transfer in randomly packed beds of equally sized spheres. International Journal of Heat and Mass Transfer 2012;55(23-24):6374–6383. doi:`10.1016/j.ijheatmasstransfer.2012.06.025`.

[178] Sloan, I.H.. Lattice methods for multiple integration. Journal of Computational and Applied Mathematics 1985;12-13(C):131–143. doi:`10.1016/0377-0427(85)90012-3`.

[179] Wu, H., Gui, N., Yang, X., Tu, J., Jiang, S.. A matrix model of particle-scale radiative heat transfer in structured and randomly packed pebble bed. International Journal of Thermal Sciences 2020;153:106334.

[180] Argento, C., Bouvard, D.. A ray tracing method for evaluating the radiative heat transfer in porous media. International Journal of Heat and Mass Transfer 1996;39(15):3175–3180.

[181] Hua, Y., Flamant, G., Lu, J., Gauthier, D.. 3D modelling of radiative heat transfer in circulating fluidized bed combustors: Influence of the particulate composition. International Journal of Heat and Mass Transfer 2005;48(6):1145–1154. doi:`10.1016/j.ijheatmasstransfer.2004.10.001`.

[182] Wu, A., Lee, S.K.. Multiple-rays tracing technique for radiative exchange within packed beds. Numerical Heat Transfer: Part B: Fundamentals 2000;37(4):469–487.

[183] Johnson, E., Tarı, İ., Baker, D.. A monte carlo method to solve for radiative effective thermal conductivity for particle beds of various solid fractions and emissivities. Journal of Quantitative Spectroscopy and Radiative Transfer 2020;:107014.

[184] Nellis, G., Klein, S.. Heat Transfer. Cambridge University Press; 2008. doi:`10.1017/CBO9780511841606`.

[185] Vignarooban, K., Xu, X., Arvay, A., Hsu, K., Kannan, A.M.. Heat transfer fluids for concentrating solar power systems - A review. Applied Energy 2015;146:383–396. doi:`10.1016/j.apenergy.2015.01.125`.

[186] Turchi, C.S., Vidal, J., Bauer, M.. Molten salt power towers operating at 600 °C to 650 °C: Salt selection and cost benefits. Solar Energy 2018;164(January):38–46. doi:`10.1016/j.solener.2018.01.063`.

[187] Sarmiento, C., Cardemil, J.M., Díaz, A.J., Barraza, R.. Parametrized analysis of a Carbon Dioxide transcritical Rankine cycle driven by solar energy. Applied Thermal Engineering 2018;140(December 2017):580–592. doi:`10.1016/j.applthermaleng.2018.04.097`.

[188] Rovense, F., Reyes-Belmonte, M.A., González-Aguilar, J., Amelio, M., Bova, S., Romero, M.. Flexible electricity dispatch for CSP plant using un-fired closed air Brayton cycle with particles based thermal energy storage system. Energy 2019;173:971–984. doi:`10.1016/j.energy.2019.02.135`.

[189] Ávila-Marín, A.L.. Volumetric receivers in Solar Thermal Power Plants with Central Receiver System technology: A review. Solar Energy 2011;85(5):891–910. doi:`10.1016/j.solener.2011.02.002`.

[190] Kribus, A., Gray, Y., Grijnevich, M., Mittelman, G., Mey-Cloutier, S., Caliot, C.. The promise and challenge of solar volumetric absorbers. Solar Energy 2014;110:463–481. doi:`10.1016/j.solener.2014.09.035`.

[191] Romero, M., Buck, R., Pacheco, J.E.. An Update on Solar Central Receiver Systems, Projects, and Technologies. Journal of Solar Energy Engineering 2002;124(2):98. doi:`10.1115/1.1467921`.

[192] Mehos, M., Turchi, C., Vidal, J., Wagner, M., Ma, Z., Ho, C., et al. Concentrating solar power: Gen3 demonstration roadmap. Tech. Rep. January; NREL; Golden, Colorado. NREL/TP-5500-67464; 2017. URL: `http://www.nrel.gov/docs/fy17osti/67464.pdf`.

[193] Ibrahim, A., Peng, H., Riaz, A., Abdul Basit, M., Rashid, U., Basit, A.. Molten salts in the light of corrosion mitigation strategies and embedded with nanoparticles to enhance the thermophysical properties for CSP plants. Solar Energy Materials and Solar Cells 2021;219(March 2020):110768. URL: `https://doi.org/10.1016/j.solmat.2020.110768`. doi:`10.1016/j.solmat.2020.110768`.

[194] Palacios, A., Barreneche, C., Navarro, M.E., Ding, Y.. Thermal energy storage tech-

nologies for concentrated solar power – A review from a materials perspective. Renewable Energy 2020;156:1244–1265. URL: `http://www.sciencedirect.com/science/article/pii/S0960148119316258`. doi:`https://doi.org/10.1016/j.renene.2019.10.127`.

[195] Chang, Z.S., Li, X., Xu, C., Chang, C., Wang, Z.F.. The Design and Numerical Study of a 2MWh Molten Salt Thermocline Tank. Energy Procedia 2015;69:779–789. doi:`10.1016/j.egypro.2015.03.094`.

[196] Singh, S., Sørensen, K., Condra, T., Batz, S.S., Kristensen, K.. Investigation on transient performance of a large-scale packed-bed thermal energy storage. Applied Energy 2019;239:1114 – 1129. doi:`https://doi.org/10.1016/j.apenergy.2019.01.260`.

[197] Xu, C., Li, X., Wang, Z., He, Y., Bai, F.. Effects of solid particle properties on the thermal performance of a packed-bed molten-salt thermocline thermal storage system. Applied Thermal Engineering 2013;57(1-2):69–80. doi:`10.1016/j.applthermaleng.2013.03.052`.

[198] Strasser, M.N., Selvam, R.P.. A cost and performance comparison of packed bed and structured thermocline thermal energy storage systems. Solar Energy 2014;108:390–402. doi:`10.1016/j.solener.2014.07.023`.

[199] Li, P., Van Lew, J., Chan, C., Karaki, W., Stephens, J., O'Brien, J.E.. Similarity and generalized analysis of efficiencies of thermal energy storage systems. Renewable Energy 2012;39(1):388–402. doi:`10.1016/j.renene.2011.08.032`.

[200] Li, P., Van Lew, J., Karaki, W., Chan, C.L., Stephens, J., O'Brien, J.. Transient Heat Transfer and Energy Transport in Packed Bed Thermal Storage Systems; chap. 20. ISBN 978-953-307-569-3; 2011, p. 373–417. doi:`10.5772/20979`.

[201] Oró, E., Castell, A., Chiu, J., Martin, V., Cabeza, L.F.. Stratification analysis in packed bed thermal energy storage systems. Applied Energy 2013;109:476–487. doi:`10.1016/j.apenergy.2012.12.082`.

[202] Torab, H., Beasley, D.E.. Optimization of a packed bed thermal energy storage unit. Journal of Solar Energy Engineering, Transactions of the ASME 1987;109(3):170–175. doi:`10.1115/1.3268201`.

[203] Allen, K., von Backström, T., Kröger, D., Kisters, A.. Rock bed storage for solar thermal power plants: Rock characteristics, suitability, and availability. Solar Energy Materials and Solar Cells 2014;126:170–183. doi:`10.1016/j.solmat.2014.03.030`.

[204] Faik, A., Guillot, S., Lambert, J., Veron, E., Ory, S., Bessada, C., et al. Thermal storage material from inertized wastes: Evolution of structural and radiative properties with temperature. Elsevier 2011;182(October):21–29. doi:`10.1016/j.solmat.2018.03.020`.

[205] Curto, P.A.. High temperature thermal storage using slag. In: Internacional Confer-

ence on Alternative Energy Sources. Miami (USA); 1980, p. 109–112.

[206] Biswas, A., Davenport, W.. Matte Smelting. In: Extractive Metallurgy of Copper; 3rd ed. Pergamon Press; 1994, p. 74–99. doi:`10.1016/b978-0-08-042124-7.50010-7`.

[207] Shi, C., Meyer, C., Behnood, A.. Utilization of copper slag in cement and concrete. Resources, Conservation and Recycling 2008;52(10):1115–1120. doi:`10.1016/j.resconrec.2008.06.008`.

[208] Gorai, B., Jana, R.K., Premchand, . Characteristics and utilisation of copper slag - A review. Resources, Conservation and Recycling 2003;39(4):299–313. doi:`10.1016/S0921-3449(02)00171-4`.

[209] Empresa nacional de minería, enami. `https://www.enami.cl`; ???? Accessed: 22-01-2021.

[210] Corporación nacional del cobre, codelco. `https://www.codelco.com/prontus_codelco/site/edic/base/port/inversiones.html`; ???? Accessed: 22-01-2021.

[211] Meier, G.H.. Research on oxidation and embrittlement of intermetallic compounds in the u.s. Materials and Corrosion 1996;47(11):595–618. URL: `https://onlinelibrary.wiley.com/doi/abs/10.1002/maco.19960471104`. doi:`https://doi.org/10.1002/maco.19960471104`. `arXiv:https://onlinelibrary.wiley.com/doi/pdf/10.1002/maco.19960471104`.

[212] Speyer, R.F.. Thermal Analysis of materials. 1st ed.; CRC Press; 1993.

[213] Hollands, K., Sullivan, H., Shewen, E.. Flow uniformity in rock beds. Solar Energy 1984;32(3):343 – 348. doi:`https://doi.org/10.1016/0038-092X(84)90277-9`.

[214] Pfeffer, R.. Heat and mass transport in multiparticle systems. Industrial and Engineering Chemistry Fundamentals 1964;3(4):380–383. doi:`10.1021/i160012a018`.

[215] Chapra, S., R.P., C.. Numerical Methods for Engineers. 7 ed.; 2 Penn Plaza, New York: McGraw-Hill Education; 2015. ISBN 9780073397924.

[216] Courant, R., Friedrichs, K., Lewy, H.. Über die partiellen Differenzengleichungen der mathematischen Physik. Mathematische Annalen 1928;100:32–74. doi:`10.1007/BF01448839`.

[217] Bell, I.H., Wronski, J., Quoilin, S., Lemort, V.. Pure and pseudo-pure fluid thermophysical property evaluation and the open-source thermophysical property library coolprop. Industrial & Engineering Chemistry Research 2014;53(6):2498–2508. doi:`10.1021/ie4033999`. `arXiv:http://pubs.acs.org/doi/pdf/10.1021/ie4033999`.

[218] Dybbs, A., Edwards, R.V.. A New Look at Porous Media Fluid Mechanics — Darcy to Turbulent. Dordrecht: Springer Netherlands. ISBN 978-94-009-6175-3; 1984, p. 199–256. URL: `https://doi.org/10.1007/978-94-009-6175-3_4`. doi:`10.1007/978-94-009-6175-3_4`.

[219] Ergun, S., Orning, A.A.. Fluid Flow through Randomly Packed Columns and Fluidized Beds. Industrial & Engineering Chemistry 1949;41(6):1179–1184. doi:`10.1021/ie50474a011`.

[220] Dincer, I., Rosen, M.. Exergy, Energy, Environment and Sustainable Developement. 1 ed.; Elsevier; 2007.

[221] Vortmeyer, D., Adam, W.. Steady-state measurements and analytical correlations of axial effective thermal conductivities in packed beds at low gas flow rates. International Journal of Heat and Mass Transfer 1984;27(9):1465–1472. doi:`https://doi.org/10.1016/0017-9310(84)90259-X`.

[222] Yang, Z., Garimella, S.V.. Thermal analysis of solar thermal energy storage in a molten-salt thermocline. Solar Energy 2010;84(6):974 – 985. doi:`https://doi.org/10.1016/j.solener.2010.03.007`.

[223] Dincer, I., Ezan, M.. Heat Storage: A Unique Solution For Energy Systems. 2018. ISBN 978-3-319-91893-8. doi:`10.1007/978-3-319-91893-8`.

[224] Sarbu, I., Sebarchievici, C.. A comprehensive review of thermal energy storage. Sustainability 2018;10(1). doi:`10.3390/su10010191`.

[225] Hussain, F., Rahman, M.Z., Sivasengaran, A.N., Hasanuzzaman, M.. Chapter 6 - energy storage technologies. In: Hasanuzzaman, M., Rahim, N.A., editors. Energy for Sustainable Development. Academic Press. ISBN 978-0-12-814645-3; 2020, p. 125–165.

[226] REN21, . Renewables 2020 Global Status Report. June; REN21 Secretariat; 2020. ISBN 978-3-948393-00-7. URL: `https://www.ren21.net/wp-content/uploads/2019/05/gsr_2020_full_report_en.pdf`.

[227] Jurigova, M., Chmurny, I.. Systems of sensible thermal energy storage. Applied Mechanics and Materials 2016;820:206–211. doi:`10.4028/www.scientific.net/AMM.820.206`.

[228] Calderón-Vásquez, I., Cortés, E., García, J., Segovia, V., Caroca, A., Sarmiento, C., et al. Review on modeling approaches for packed-bed thermal storage systems. Renewable and Sustainable Energy Reviews 2021;143. doi:`10.1016/j.rser.2021.110902`.

[229] Trevisan, S., Guedez, R., Laumert, B.. Thermodynamic analysis of an indirect supercritical co2 – air driven concentrated solar power plant with a packed bed thermal energy storage. In: Proceedings of SOLARPACES 2019; vol. 2303. 2020, p. 130007. doi:`10.1063/5.0028624`.

[230] Trevisan, S., Ruan, T., Wang, W., Laumert, B.. Techno-economic analysis of an innovative purely solar driven combined cycle system based on packed bed tes technology. In: Proceedings of SOLARPACES 2019; vol. 2303. 2020, p. 130008. doi:`10.1063/5.0028724`.

[231] Dumont, O., Frate, G.F., Pillai, A., Lecompte, S., De paepe, M., Lemort,

V.. Carnot battery technology: A state-of-the-art review. Journal of Energy Storage 2020;32:101756. doi:`https://doi.org/10.1016/j.est.2020.101756`.

[232] Budt, M., Wolf, D., Span, R., Yan, J.. A review on compressed air energy storage: Basic principles, past milestones and recent developments. Applied Energy 2016;170:250–268. doi:`https://doi.org/10.1016/j.apenergy.2016.02.108`.

[233] Benato, A., Stoppato, A.. Heat transfer fluid and material selection for an innovative pumped thermal electricity storage system. Energy 2018;147:155–168. doi:`https://doi.org/10.1016/j.energy.2018.01.045`.

[234] Calderón-Vásquez, I., Segovia, V., Cardemil, J.M., Barraza, R.. Assessing the use of copper slags as thermal energy storage material for packed-bed systems. Energy 2021;:120370doi:`https://doi.org/10.1016/j.energy.2021.120370`.

[235] Trevisan, S., Guedez, R., Bouzekri, H., Laumert, B.. Initial design of a radial-flow high temperature thermal energy storage concept for air-driven csp systems. In: AIP Conference Proceedings; vol. 2126. 2019, p. 200031. doi:`10.1063/1.5117746`.

[236] McTigue, J., White, A.. A comparison of radial-flow and axial-flow packed beds for thermal energy storage. Applied Energy 2018;227:533–541. doi:`10.1016/j.apenergy.2017.08.179`.

[237] Bergman, T.L., Lavine, A.S., Incropera, F.P., DeWitt, D.P.. Fundamentals of heat and mass transfer; vol. 1. 8 ed.; John Wiley; 2016. ISBN ES8-1-119-32042-5.

[238] Yung, S.C.. Free convection heat transfer from an inclined heated flat plate in air. Ph.D. thesis; University of Missouri at Rolla; 1965.

[239] McTigue, J.. Analysis and optimisation of thermal energy storage. Ph.D. thesis; University of Cambridge; St. Catharine's College; 2016.

[240] Bejan, A.. Entropy Generation Minimization: The Method of Thermodynamic Optimization of Finite-Size Systems and Finite-Time Processes; vol. 1. 1 ed.; CRC Press; 1996. ISBN 0-8493-9651-4.

[241] Trevisan, S., Jemmal, Y., Guedez, R., Laumert, B.. Packed bed thermal energy storage: A novel design methodology including quasi-dynamic boundary conditions and techno-economic optimization. Journal of Energy Storage 2021;36:102441. doi:`https://doi.org/10.1016/j.est.2021.102441`.

[242] Leister, . Hotwind Premium & Hotwind System User's Guide. Leister Technologies AG.; 2011.

[243] SODECA, . Informe técnico de datos CMP-820-2T IE3. SODECA Group; 2020.

[244] Kanomax, . Anemomaster Model 6162 Operation Manual. Kanomax; 2020.

Appendix A

Experimental facilities

In the context of the project FONDECYT 1191705: *High-Temperature thermal storage for CSP power plants using packed bed of rocks: heat transfer analysis and experimental validation*, two experimental facilities have been built to assess the thermal behavior of the copper slags as a storage media. Due to several drawbacks, it has not been possible to run these test benches yet. Nevertheless, several efforts have been developed to acquire new equipment and to elaborate the experimental methods. This section details the components of the experimental bench, as well as the description of the tests that will be conducted to validate the analytical models and determine the performance of the system.

A.1 Description of storage tanks and test facilities

The experimental setup developed for this project consist in a steel storage unit filled with copper slags, and it is connected to pipes which transport the high-temperature air from a heat source to the tank during the charging process. The system also operates at low temperatures, allowing the discharging process through the circulation of the cold air across the packed-bed, recovering the energy stored and exiting the system at high temperatures. Regarding the heat source, it operates with a fan which take atmospheric air and passes it over a heating coil raising the temperature of the fluid to a desired output.

In order to perform tests at different operating conditions, two storage units were built. The first prototype should operate in a medium temperature range (up to 350 °C), and it consists in a 50 L tank with a pipping arrangement which enables the flow of air in different directions through the tank by opening and closing valves. For the second packed-bed system, a simpler concept was chosen on the design of a 8 L unit, which is a removable cylinder connected to two tubes using flanges and is expected to be tested at temperatures up to 650 °C. On the following, the two experimental setups are described in terms of they main features and expected operating conditions.

A.1.1 Medium-temperature storage

To develop experimental tests of a packed-bed TES under medium-temperature conditions, a vertical-oriented 50 liter cylinder tank was built. The storage unit consist in a 304 mm diameter and 688 mm height cylinder with two conical lids placed at the top and bottom of the tank, which allows a uniform distribution of the flow at the inlet during the TES's charge/discharge process. The fluid is transported and guided through a set of pipes and valves, enabling it to entering and exiting the tank (see Figure A.1a). Inside the storage unit, the rock pile is supported by a mesh with 10 mm holes, that prevents small pebbles from falling to the bottom of the lid and obstructing air flow. In Figure A.1b the assembly of the mesh inside the tank is illustrated. As shown in Figure A.1c, the mesh is surrounded by a steel ring which restricts its movement and allows it to be bolted to the base of the tank. All the aforementioned components are fabricated in stainless steel.

The expected operating conditions of this experimental facility are based on the equipment that is going to be coupled to, which is explained latter in this appendix. The conditions are presented in Table A.1.

Table A.1: Operating conditions of the medium-temperature storage

Operating condition/range	Value
Temperature	≈20 °C (room temperature) to 350 °C
Expected air flow rate	$300\,\mathrm{m^3/h}$
Predicted pressure drop	1.12 kPa
Inlet static pressure given by the fan	1.34 kPa
Power to fan	1 kW

As mentioned above, the piping system of this test bench is composed by several elements which enables different flow directions, depending on whether the TES is operating in charging or discharging mode. By opening and closing valves, the air flow can be controlled aiming to keep the stratification within the storage tank. Figure A.2 illustrates the P&ID diagram of the experimental facility. The valves are indicated with numbers in order to indicate which ones should be open/closed for the different processes to be studied.

- **Charging process:** The valves 2 and 5 has to be open, while valves 1, 3, and 4 has to be closed; therefore, the air at high temperatures can flow from the heat source (indicated as HW in Figure A.2), entering the storage tank at the top, and exiting at low temperatures from the bottom.
- **Discharging process:** After the charging process, the energy stored in the packed-bed TES need to be recovered. In that context, the heat source has to be turned off; thus, the air supplied will be at room temperature. By closing the valves 2 and 5, opening the valves 1, 3, and 4, the air can flow from the bottom to the top of the tank, exiting the system at high temperatures.

In constructive aspects, several drawbacks have been noticed in this system such as the deformation of the main tank and the diffuser cones during welding. That issue is relevant for insulating the system, since hot air leakage can be generated in those zones during operation.

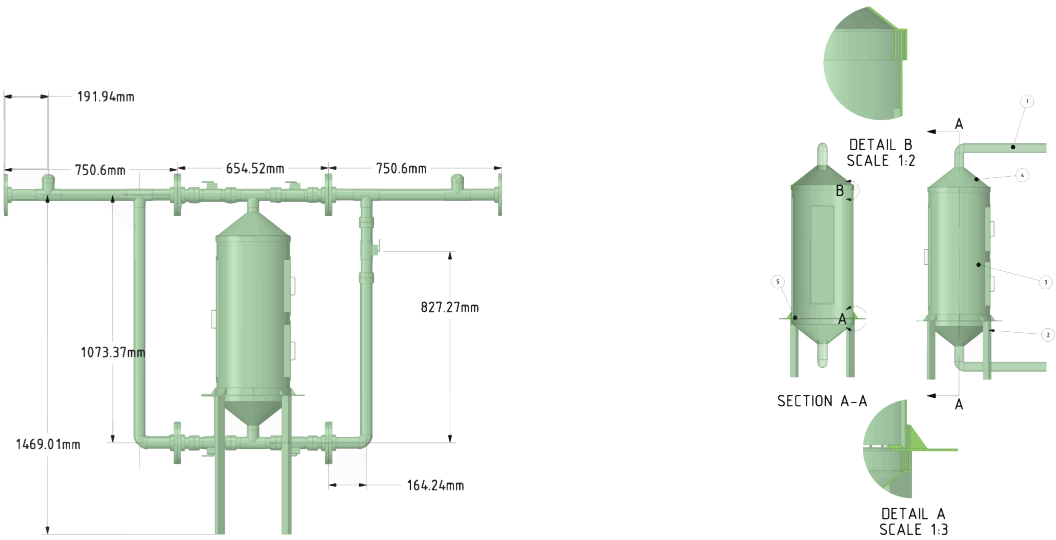

(a) General assembly.

(b) Diagram of mounting of conical lids and internal mesh.

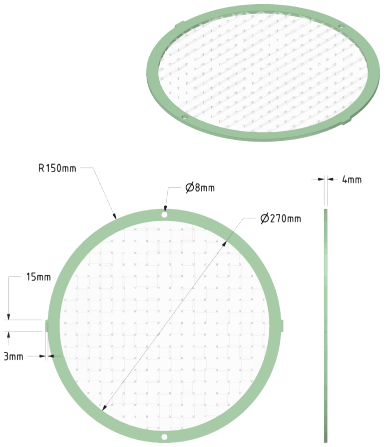

(c) Internal mesh

Figure A.1: Overview of the medium-temperature TES components.

Hence, prior to the first tests, those components need to be modified and properly mounted to ensure a safe operation. Furthermore, the system has yet to be instrumented with the following sensors: Type K thermocouples distributed in the length of the storage tank (as indicated in Figure A.2), a differential pressure with terminals at the inlet and outlet of the piping structure, where also type K thermocouples are needed to measure the temperature in those points. The sensors are connected to a datalogger, where the data can be stored and read for post-processing.

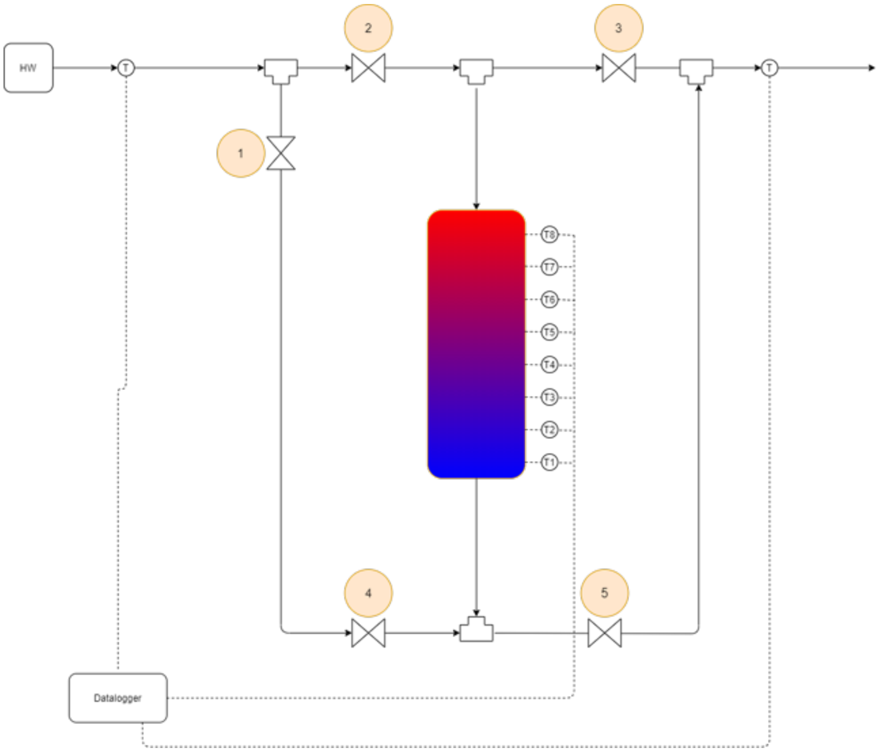

Figure A.2: P&ID diagram of the medium-temperature TES system.

A.1.2 High-temperature storage

The study of the high-temperature performance of a packed-bed TES composed with copper slags, is expected to be conducted in a cylindrical tank horizontally-disposed, as illustrated in Figure A.3. The internal capacity of the main tank is 7.45 L, which is assembled to pipes at each end using flanges. Additionally, two internal meshes are included inside the tank in order to keep the rocks distributed in the cylindrical domain. In Figure A.3b is shown how the meshes are fixed in the storage unit: The mesh is placed on a perforated platen welded inside the tank, while a second platen is mounted over the mesh and fixed to the lower one through bolts. The modular design of this packed-bed TES system, facilitates the removal of the central cylinder and the test of different "packed-bed probes" in the setup. The whole system is supported in a carbon steel holder attached at the worktable (see Figure A.3a).

The storage tank dimensions corresponds to a length of 400 mm and an internal diameter of 158 mm, and it is made by carbon steel. The tank is welded at two flanges of the same material that enables the union with the remaining piping elements manufactured in stainless steel. In contrast to the medium-temperature experimental bench, the air flows in one direction. The latter does not corresponds to the typical operating logic of packed-bed TES system, nonetheless, the experimental procedures are simpler than the medium-temperature test bench.

During its operation, the heat source composed by a high-temperature air blower with an internal heater, which takes atmospheric air and supply it to the system through the inlet pipe. The operating conditions expected are listed in Table A.2. Regarding the static pressure provided by the air blower, the given value is the maximum specified by the manufacturer

(a) General assembly.

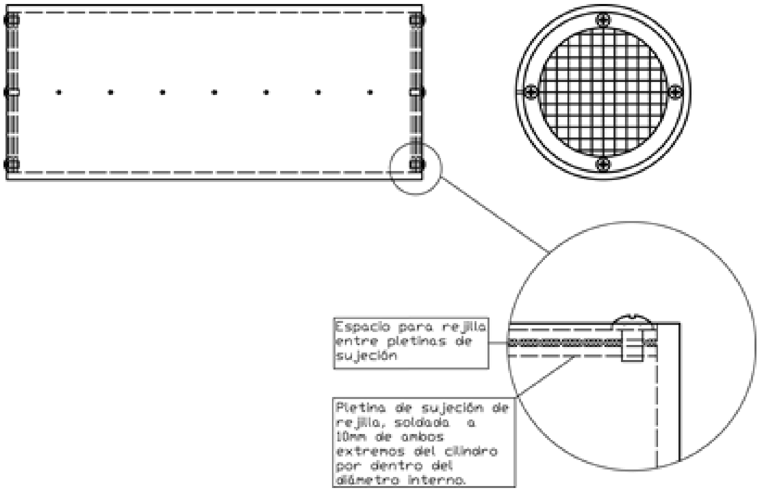

(b) Diagram of mounting the internal mesh.

Figure A.3: Overview of the high-temperature TES components.

since no characteristic curves are not available [242].

Considering the diagram showed in Figure A.4, the basic operation of the system can be separated in two processes: The charging process, where the air is provided at 650 °C by the air blower, entering the tank where the heat is transferred to the rocks, and leaving the system from the outlet pipe. The discharging process occurs in the same direction, by setting the air blower to a low temperature mode. The atmospheric air at room temperature enters the storage, recovering the heat stored and leaving the system at high temperatures from the same outlet pipe. In order to measure the different variables during the heat transfer process, at the inlet and outlet pipe terminals are available to put a type K thermocouple and a capillary tube for a differential pressure sensor. In the storage tank, the type K thermocouples are distributed along the cylinder, to measure the thermocline's behavior. Lastly, at the outlet of the tank a hot wire probe is disposed, which can measure the air

Table A.2: Operating conditions of the high-temperature storage

Operating condition/range	Value
Temperature	≈20 °C (room temperature) to 650 °C
Expected air flow rate	18 m^3/h
Predicted pressure drop	34.91 Pa
Max. static pressure of the air blower	1 kPa
Air blower power	3.7 kW

velocity at high temperatures. The probe is connected to a digital anemometer, where the data can be stored and read in real time, whereas the other sensors are linked to a datalogger to collect the information of the TES system.

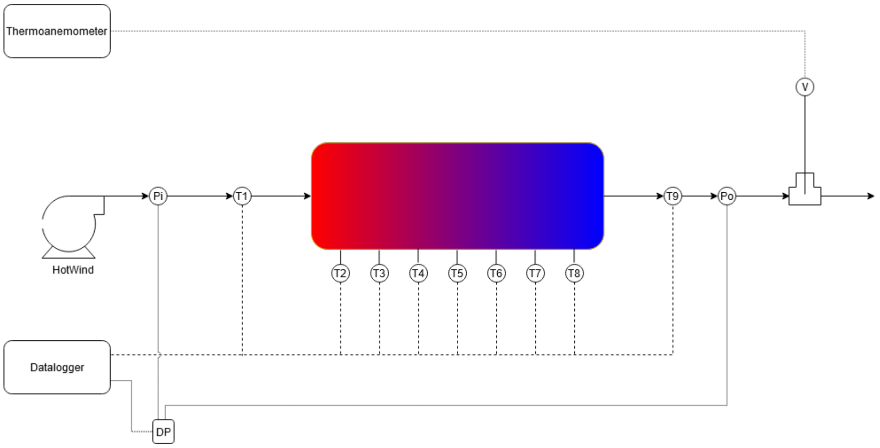

Figure A.4: P&ID diagram of the high-temperature TES system.

Regarding the insulation of the system, between the bolted joints in the structure, EcoGraf seals are employed to prevent air leakage through those zones. To reduce the thermal losses to the environment, a 50 mm layer of mineral wool is disposed in all the elements of the system and externally supported with a steel mesh wire.

A.2 Equipment available

The selection of the experimental equipment represented a great challenge during the design of the test bench, owing to the high operating temperatures expected in the system. The instruments able to withstand temperatures over 600 °C for a considerable amount of time aren't adequate for the experimental setup scale; therefore, modifications had to be made to the design conditions of the experimental study. On the following, a description of the equipment acquired is provided.

A.2.1 Heat sources

One of the heat source employed to rise the air temperature is the air blower from Leister mod. Hotwind System of 3700 W power. The technical specifications and components are detailed in its user manual [242], however, a brief explanation will be made according to its general operating principle.

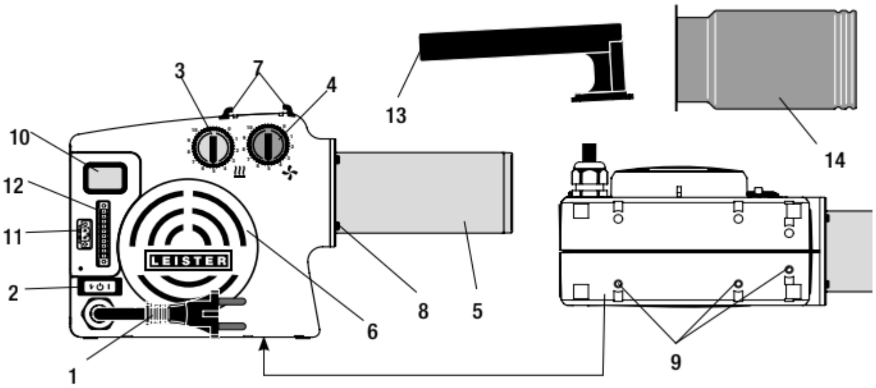

Figure A.5: Air blower diagram and components [242].

The Hotwind System is a fan with an internal electric resistance, which transfers heat to the incoming atmospheric air and exiting the blower at high temperatures. The air intake in marked with the number 6 in Figure A.5, while the heating element is located in the tube marked with the number 5. As observed in Figure A.5 the device has independent knobs for regulating the heating power and the air flow (indicated with number 3 and 4, respectively). Furthermore, it has a display (10) which shows the operating temperature and flow rate. The user also can set the device's internal program in order to control the heating power and/or air flow rate as convenient.

Despite on having independent knobs to control the heat and the flow independently, the actual values delivered by the equipment will depend on the fan operating curves. In Figure A.6b it is indicated the expected values of the heating power and the air flow rate for each position of the respective knob, but according to the curves in Figure A.6a, as the air flow increases, the outlet temperature decreases as a result on the reduced heating power at those airflow conditions. On the other hand, according to the manufacturer, for a Hotwind System with 3680 W of power, a 100 % of the heating power can be achieved when a flow rate of 300 L/min is set [242].

This device was initially planned to be used as heat source for the 50 L storage tank, but the low flow rate to achieve high temperatures influences the experimental operating periods of the system. While its use in a lower scale TES system would allow the execution of multiple consecutive charge-discharge tests. Therefore, a second heat source system is required for the 50 L tank. Aiming to increase the air flow rate conditions, a centrifugal fan is employed; thus, the product CMP-820-2T from SODECA is selected which can reach flow rates up to 1950 $\mathrm{m^3/h}$ [243]. According to the characteristic curves presented in Figure A.7 to ensure a proper operation in the packed-bed, the initial tests must be conducted at low air flow rates, where the static pressure is higher and capable to move the air through the rock pile.

The centrifugal fan is coupled to a 35 kW heating coil manufactured by *Componentes Industriales Ltda.* It consist in a square tube with 18 electric resistances mounted in the inside which provide heat to the circulating air, exiting the domain at 350 °C towards the packed-bed TES.

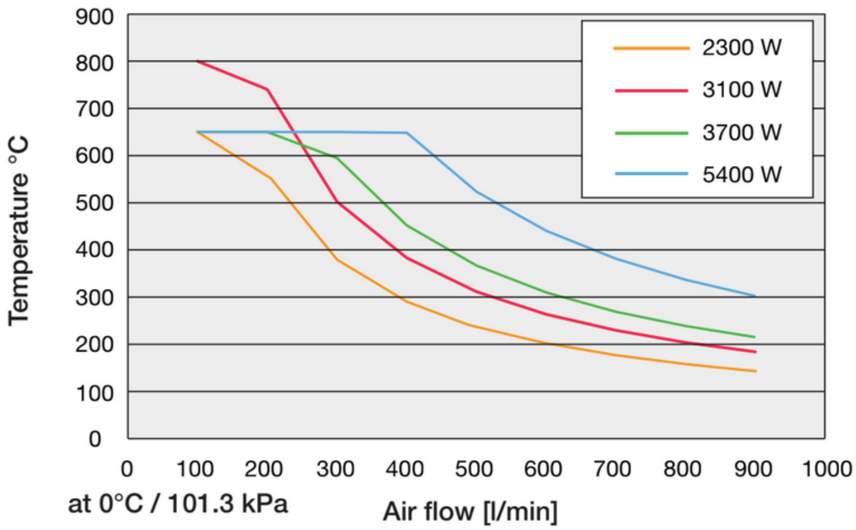

(a) Operating curve Air flow vs Temperature [242].

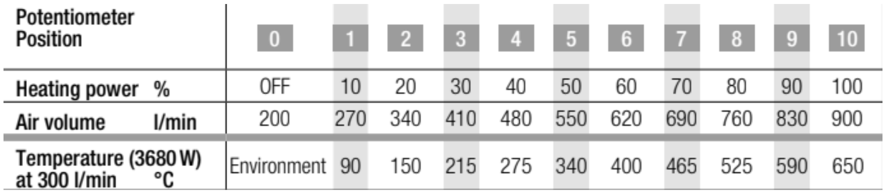

Potentiometer Position	0	1	2	3	4	5	6	7	8	9	10
Heating power %	OFF	10	20	30	40	50	60	70	80	90	100
Air volume l/min	200	270	340	410	480	550	620	690	760	830	900
Temperature (3680 W) at 300 l/min °C	Environment	90	150	215	275	340	400	465	525	590	650

(b) Heat source operation [242].

Figure A.6: General operation of the Hotwind System.

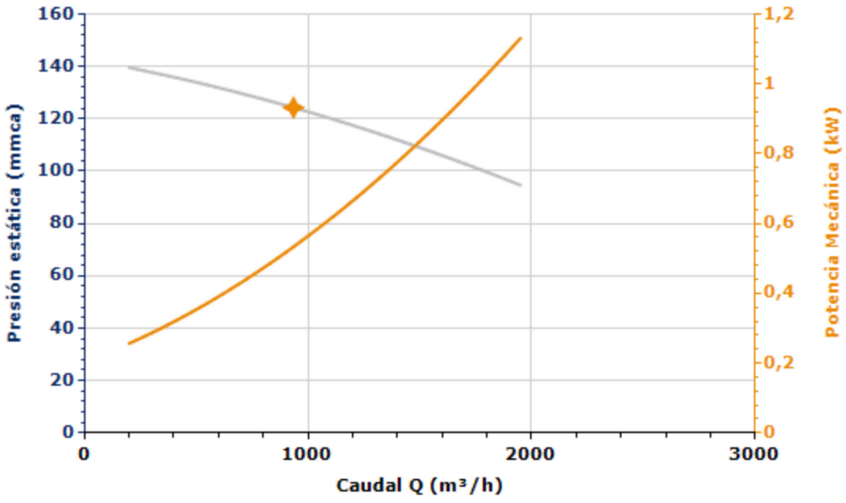

Figure A.7: Characteristic curves of the fan [243].

A.2.2 Measuring instruments

Thermo-anemometer In order to measure the air velocity, a high-temperature thermo-anemometer has been acquired. The Anemomaster 6162 developed by Kanomax is an anemometer designed for specialized high-temperature testing, which is illustrated in Figure A.8a. By using the high-temperature probe 0205 (see Figure A.8b), air velocity and temperature can be measured at limits up to 500 °C. The anemometer also has a display where the data is showed in real time and it can be connected to a laptop to store the data for future post-processing [244].

(a) Anemomaster 6162.

(b) High-temperature probe.

Figure A.8: High-temperature anemometer main components.

The high-temperature probe is composed by a thin platinum coil located in its tip and covered with a mesh to prevent the damage. To measure the fluid's temperature and velocity, the flow has to be in contact with that sensor. The platinum coil acts as a hot-wire, so when it is exposed to the airflow the sensor will be cooled. The amount of heat (H) removed from the sensor is expressed as follows [244]:

$$H = \left(a + b\sqrt{U}\right)(T - T_a) \tag{A.1}$$

where U is the fluid velocity and T_a its temperature. T is the sensor temperature, a and b are constants. with the theoretical basis given by Equation A.1, a velocity and temperature sensor can be developed within the probe in order to measure the fluctuations of each variables [244].

A.3 Experimental methods

The following section describes experimental methodologies to perform heat transfer tests in the high-temperature packed-bed TES. Regarding the medium-temperature experimental setup, no test proposals are discussed, since major constructive improvements are required.

A.3.1 Rocks selection for tests

The copper slags from the local foundries have irregular shapes and sizes; hence, prior to develop the experimental studies of its thermal behavior in a packed-bed TES, a proper selection of the rocks has to be conducted. For this preliminary stage, 2 physical characteristics are important for the classification of the copper slags:

- Fragility: The rocks that are easy to break by hand.
- Shape: The degree of *cubicity*[1] and how compact the rock is.

Some general considerations for the selection are described below:

a. Choosing compact rocks reduce the probability of fracture during tests. Most of copper slags have a compact shape with flat sides and edges, nevertheless, some have cavities and irregular edges (see Figure A.9a). These rocks can be broken by hand, obtaining a pair of compact slags.

b. In general, the copper slags are fragile and can be fractured by hand or hitting them with another rock. Conversely, some will present more resistance; therefore, they must be selected for thermal storage tests.

c. When handling the rocks, it can be noticed that some slags with similar size tend to have a noticeable different weight. The heavier ones may be harder and with compact vitreous characteristics (a shiny texture), as shown in Figure A.9b.

d. For the cubicity, a rock will be considered with cubic shape if it has at least one relatively flat side (see Figure A.9c). Also, if its shape is regular and compact such as the rocks in Figure A.9d.

e. The size considered corresponds to a length and width between 5 to 7 cm. A quick way to select them is to set a length of 25 cm and align 4 to 5 rocks along it.

There is still no research studies on how the shape of the filler materials affect the packed-bed TES's performance. Indeed, the thermal models assumes a continuum porous medium, but some heat transfer coefficients are developed by assuming spherical shape. Even though those models are experimentally validated, no further description about the characteristics of the filler material is made. In that context, it is expected a lower error in the analytic model when contrasted with data from a packed-bed TES arrangement with low cubicity copper slags, than for those composed by rocks with cubic shape.

---

[1] The actual degree of cubicity of the slags has not yet been measured. In this initial classification, it will qualified according its straight sides' tendency.

(a) Irregular rock with minor cavities.

(b) Compact rocks: irregular shape with fractures (left) and high cubicity with vitreous characteristics (right).

(c) Vitreous and compact rock, with a relatively flat side.

(d) Regular and compact rocks.

Figure A.9: A collection of copper slags.

A.3.2 Tests proposals

Measuring void fraction

In a porous medium, the void fraction is a measure of the arrangement's porosity. For the 1D thermal model proposed in this dissertation, in a cylindrical packed-bed with axial flow the void fraction along the axial coordinate is assumed constant. Therefore, to validate the analytic formulation it is necessary to measure the overall void fraction of the packed-bed TES.

The experimental procedure should take place after the heat transfer tests, since the storage tank is going to be filled with water and the copper slags may still be wet when heated. The latter can cause salts to be deposited on the slag due to exposure to high temperatures. The experimental methodology is listed as follows:

1. Disassemble the central cylinder from the piping flanges and transport it to a water draining zone.

2. Put the cylinder in vertical position and place it on a weight. Record the mass of the rocks + cylindrical tank system $M_{sys,2}$.
3. Remove the bolts holding the steel ring and the wire mesh from one side of the cylinder.
4. Using a plastic, cover the remaining hole and assemble the steel ring and the mesh removed in step 3. Turn the cylinder leaving the end with the plastic at the bottom, and place it on the weight.
5. Using a hose, fill the tank with water from the top without exceed the level of the wire mesh. Record the mass of the rocks + cylindrical tank system + water $M_{sys,5}$.
6. Drain the water and remove the plastic from the other end of the tank.

Using the data from the previous procedure, the volume of drained water V_w can be calculated using Equation A.2, which is equivalent to the volume that is not being occupied by the rocks inside the tank.

$$V_w = \frac{M_{sys,5} - M_{sys,2}}{\rho_w} \tag{A.2}$$

where ρ_w is the water density. Finally, the experimental void fraction (ε_{exp}) of the arrangement can be calculated with

$$\varepsilon_{exp} = \frac{V_w}{V_T} \tag{A.3}$$

where V_T is the internal volume of the tank where the rocks are confined.

Heat transfer experiments

In this first stage of the study, the temperature evolution along the storage tank will be evaluated, as well as the temperature at the system's inlet and outlet.

Thermal equilibrium during charging and discharging processes It is proposed to study the characteristic heating/cooling time ($\hat{t}_{h/c}$) of the system, corresponding to the total time required to heat/cool all the rocks within the tank. The analytical expression of $\hat{t}_{h/c}$ can be obtained by performing an energy balance in the packed-bed, where the heat required to raise all the solids to the working temperature must be equal to the energy provided by the air (see Equation A.4).

$$\hat{t}_{h/c} = \frac{(1-\varepsilon)\,(\rho c_p)_s}{c_{p,f} G} H_T \tag{A.4}$$

where H_T is the packed-bed height, G the mass flux rate, ρ_s and $c_{p,s}$ are the solid density and specific heat, $c_{p,f}$ is the specific heat of the fluid and ε the void fraction of the arrangement. The fluid properties will depend on whether it is a charging or discharging process. The following methodology is proposed for the study of characteristic time:

1. Turn on the fan and set its flow rate to 300 L/min, either by using the control system or by manual adjustment of the blue knob. The latter is between the position 1 and 2.
2. Raise the temperature to 650 °C. Similar to the previous point, it can be done by a control system or manually, turning the red knob to the position 10. As this increase is not immediate, the measured temperature by thermocouple 1 (T1 indicated in Figure A.4) has to be supervised by connecting a laptop to the datalogger.
3. When the target temperature is reached at the storage's inlet, it is considered the beginning of the charging process. The storage will be considered as fully charged when the outlet temperature (thermocouple 9 in Figure A.4) fullfil the condition $|T_{T9} - T_{T1}| < 2\tau$, where τ is the precision of the thermocouples.
4. For the discharging process, the red knob need to be in the position 0 to supply air at room temperature. The decrease of the temperature should be verified in thermocouple 1 in the same way as step 2.
5. Once the inlet is at room temperature, the storage is under discharging process. That stage will end under the same condition established in step 3.

Variable temperature profiles for system charging and discharging The objective is to operate the TES system in a controlled environment by varying the air's inlet temperature with the time. Consequently, consecutive charge-discharge cycles can be generated. Likewise, the air-flow rate entering the system can be controlled, which makes the experimental setup more similar to the operation of a CSP plant. Even though the measures of the fluid velocity is relevant for this experiment, as mentioned before only the temperatures are being evaluated in this initial stage of experiments.

The following procedures described are classified depending on the cut-off criteria for the control logic: Controlled by time, and controlled by temperature reached in the array. Those aforementioned conditions can be programmed in the Hotwind System air blower by using the interface provided by the manufacturer.

- **Inlet temperature controlled by time:** The study proposed consists on program a partial consecutive charge-discharge cycles by setting charge/discharge times shorter than $\hat{t}_{h/c}$, to characterize how the temperature profiles of the subsequent cycles are affected by the remaining stored energy in the system. Figure A.10 shows 3 consecutive charge-discharge cycles developed by assuming a charging/discharging period equivalent to $\hat{t}_{h/c}/2$.
- Inlet temperature controlled by temperature reached in the system: In order to emulate a thermal process where the heat is stored and discharged under limited operating conditions, the following ranges are considered: A fictional process operates with air at temperatures between 400 - 600 °C, and it is coupled to a heat source that supplies air at 650 °C. A direct storage is employed to lower the air temperature after entering the process, and keeping it always within the specified ranges. The control logic is described below:
    1. Raise the system's temperature: The air is injected at 650 °C with a flow rate of 300 L/min until T_{T9} >600 °C.
    2. After reaching that limit, atmospheric air is supplied at room temperature to the packed-bed from the air blower, in order to recover the heat stored. The

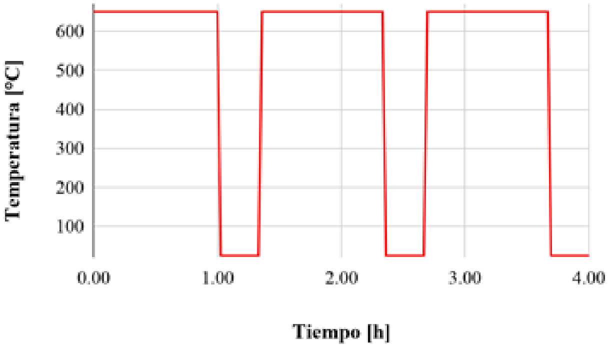

Figure A.10: Time-dependent temperature profiles for 3 charge-discharge cycles.

flow rate can be boosted to 900 L/min. The discharging process is extended until T_{T9} <400 °C.

3. As the lower temperature is achieved, the system is restarted by repeating the steps 1 and 2 aiming to collect a considerable amount of data.

A.3.3 Safety considerations

When working at high-temperature conditions, there are safety considerations that has to be taken into account to prevent accidents. The procedures described should always be done before each heat transfer test, since the heating cycles will affect the system's integrity and its structure. Therefore, air leakages and irregularities must be verified.

Heat transfer tests safety considerations

- During operation, do not pass or stand in front of the air outlet pipe.
- The fan cannot be turned off if there still are regions in the tanks above 50 °C. Considering that the injected air is at room temperature.
- Initialization of the system for the first test: After verifying that there are not air leaks through the joints, a progressive heating of the system should be performed to stabilize the operation at each position of the red knob (heating power) in the Hotwind System. The procedure is described below:
  1. Increase the temperature (manually or by controller) at 50 °C intervals every 15 min, and check the temperature values using a laptop connected to the datalogger.
  2. When the 100 % heating power is reached (red knob at 10^{nth} position), the system has achieved the maximum temperature available for that air flow rate, and it can be cooled down.
  3. Carry out step 1 but in reverse, reducing the temperature every 15 min.
  4. Repeat steps 1 to 3 for all positions of the flow rate (blue knob). In the last position, keep the fan turned on until the system is completely cooled.

  During the process described above is relevant to verify that there are no problems during operation at high temperatures. In addition, it allows the thermal stabilization of the copper slags in the packed-bed. Subsequent tests should be operated regularly under the safety notes already mentioned.

Void fraction tests safety considerations

- Before removing any part of the system, verify that the assembly is at room temperature.
- Verify that the fan is turned off prior to any part removal.
- The whole system will be covered with an insulating jacked mainly composed by mineral wool. Therefore, the assembly must be handled with globes, safety shoes, goggles and mask.
- Special considerations have to be accounted before removing the main cylinder, which are listed as follows:
    1. Disconnect all sensors attached to any data acquisition device.
    2. Remove the insulating jacked from the central cylinder without forcing the thermocouples arranged along the tank.
    3. Withdraw the bolts from the flanges attached to the main cylinder.
    4. Detach the base that holds the central cylinder from the worktable.
    5. Remove the central cylinder from the assembly.